Queen Mary University of London

Hot Jet Noise Modelling

Vasily Gryazev

Supervisor: **Dr. Sergey Karabasov**

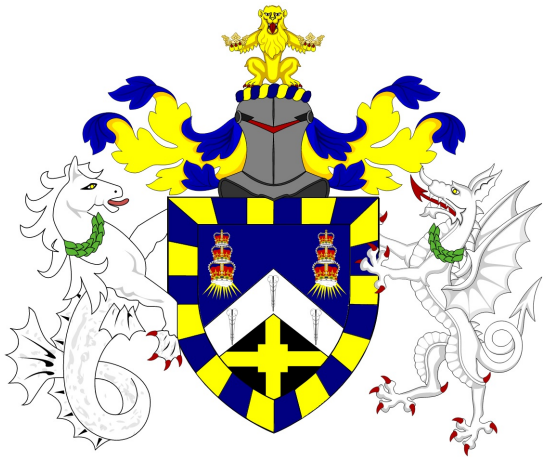

A thesis submitted to the

School of Engineering and Material Science

in partial fulfilment of the requirements of the

Degree of Doctor of Philosophy

September 2019

Declaration

I, Vasily Gryazev, confirm that the research included within this thesis is my own work or that where it has been carried out in collaboration with, or supported by others, that this is duly acknowledged below and my contribution indicated.

I attest that I have exercised reasonable care to ensure that the work is original, and does not to the best of my knowledge break any UK law, infringe any third partys copyright or other Intellectual Property Right, or contain any confidential material.

I accept that Queen Mary University of London has the right to use plagiarism detection software to check the electronic version of the thesis. I confirm that this thesis has not been previously submitted for the award of a degree by this or any other university.

The copyright of this thesis rests with the author and no quotation from it or information derived from it may be published without the prior written consent of the author.

Signature: Vasily Gryazev

Date: 30/09/2019

Acknowledgements

I would like to express my sincere gratitude to my supervisor Dr. Sergey Karabasov for the guidance during my Ph.D study, for his patience, motivation and immense knowledge. His expertise was invaluable in the formulating of the research topic and methodology.

I am also deeply thankful to Dr. Anton Markesteijn, who has greatly contributed to this work. Without his support this thesis could not have been accomplished.

I would like to acknowledge the help received through the collaborative work undertaken with the my colleagues Dr. Anuroopa Kalyan and Dr. Dominic Tan.

Contents

List of Figures

List of Tables

List of Symbols

Roman Letters

c	Speed of sound
c_l	Turbulent length-scale coefficient
c_τ	Turbulent time-scale calibration coefficient
D_j	Nozzle Diameter
f	Frequency
$G_{\mu k}$	Matrix Green's function
G_k^a	Adjoint vector Green's function
h	Enthalpy
$I_{\mu j}$	Propagator tensor
k	Wavenumber
l_s	Correlation length scale
M	Mach number
M_c	Convective Mach number
n	Mode number
p	Pressure
R	Distance from the nozzle exit to observer

St	Strouhal number
t	Time
T	Temperature
T_{ij}	Lighthill stress tensor
$R_{\mu jkl}$	Generalized stress tensor
U_c	Convective velocity
Q	Source
$\mathbf{v}$	Velocity vector
u, v, w	Velocity components
Re	Reynolds number
x	Axial coordinate
r	Radial coordinate
x_s	Axial coordinate of the source
r_s	Radial coordinate of the source
$\mathbf{x}$	Position vector of observer
$\mathbf{y}$	Position vector of source

Greek Letters

α	jet spreading rate
β	potential core length
α_{ijkl}	Quadrupole source stengths
β_{ij}	Dipole source stengths
κ	Turbulent kinetic energy
ε	Turbulent dissipation
ρ	Density
δ_{ij}	Kronecker symbol
$\delta(\cdot)$	Dirac delta function
ω	Angular frequency
ϕ	Polar angle
θ	Azimuthal angle
τ	Source point time variable
τ_s	Correlation time scale

Subscripts

i, j, k, l, μ	Vector or tensor components
$\cdot_\infty$	Ambient condition
$\cdot^a$	Adjoint components of Green's function
$\cdot_j$	Relating to jet
$\hat{\cdot}$	Fourier transform
$\bar{\cdot}$	Time average
$\tilde{\cdot}$	Favre-filtered quantity
$\cdot'$	Fluctuating component
$\cdot_{ref}$	Reference value
$\langle\cdot\rangle$	Averaging over defined interval

Abbreviations

CABARET	Compact Accurately Boundary Adjusting Technique
CFD	Computational Fluid Dynamics
CoJeN	Computation of Coaxial Jet Noise
DES	Detached Eddy Simulation
ICAO	International Civil Aviation Organization
LDA	Laser Dopplet Anemometry
LES	Large Eddy Simulation
LTRAC	Laboratory of Turbulence Research in Aerospace and Combustion
NPR	Nozzle Pressure Ratio
OP	Operation Point
PIV	Particle Image Velocimetry
RANS	Reynolds Averaged Navier-Stokes
TTR	Total Temperature Ratio
WMLES	Wall-Modeled Large Eddy Simulation

Introduction

Impact of noise emissions associated with the commercial aviation poses a challenge to aircraft manufactures in the 21st century. Excessive noise levels in the vicinity of the airports and urban areas are not only annoying, but also have a direct implication for people's health. Adverse effects of aircraft noise on wildlife are also well-known. With a predicted increase of number of aircraft around the world noise pollution tends to increase accordingly. Aircraft noise is regulated by International Civil Aviation Organization (ICAO) which poses stringent noise regulations to alleviate the noise. Aircraft noise sources of aerodynamic origin include several major components, one of which that is very important for take-off conditions is noise generated by the propulsive jet flow from the engine exhaust, i.e. jet noise. Hence, predictions of jet noise is an essential component of the multidisciplinary design optimisation studies where the reduction of noise and NOx emissions is becoming a second important criterion for aeroengine design after safety. The process of noise generation in high-speed jet flow is characterised by the coexistence of a disparity of flow scales which include large-scale coherent structures and fine-scale turbulence interacting with acoustic waves whose scale is typically much larger than the that of the aerodynamic scales in the jet. All this complexity is exacerbated by incomplete understanding of turbulence properties of the anisotropic high-Reynolds number flows. Hence, understanding and prediction of jet noise is a complex task that has been a challenge for researchers since the dawn of the first aircraft. In general, jet noise is a classical problem of

aeroacoustics, which solution involves knowledge from several disciplines such as fluid dynamics, applied mathematics, and computational modelling. In particular, computational modelling has become a very important tool in jet noise research since unsteady high-resolution computational methods for free-shear flow simulations have now reached a mature state. These methods can provide a wealth of information about the physics of sound generation in turbulent jet flows that can be used in further theoretical modelling. Computational methods for solving jet noise problems can be broken down into direct and hybrid approaches.

Direct computation methods

In this category, high resolution schemes are used for solving the governing Navier-Stokes equations from the first-principles in the entire computational domain including the far field. The development of direct methods has been greatly facilitated by the significant growth of computer power. In the direct numerical simulations the governing three-dimensional Navier-Stokes equations are solved on a fine grid to resolve the viscous scales. Not surprisingly, this approach is very expensive and currently only amenable for relatively low to moderate Reynolds number flows, $O(10^5)$ even on supercomputers, while the Reynolds number range of interest for jet noise is $O(10^6\text{-}10^7)$. More practical approaches such as Large Eddy Simulation (LES) employ sub-grid scale modelling schemes to approximate the viscous scale effect. In many cases, hybrid approaches are used where LES is merged with Reynolds Averaged Navier-Stokes equations. These include the family of Detached Eddy Simulation (DES) and Zonal LES approaches where there a RANS solution is used in the vicinity of the nozzle wall boundaries and LES is applied in the free-shear zone flow. In addition to traditional Eulerian Navier-Stokes methods such as those developed by Bodony and Lele [1], Bailly and Bogey [2], Uzun et al. [3], Spalart et al. [4], Karabasov et al [5], Markesteijn et al. [6] a promising alternative approach which is based on particle in cell method such as Lattice Boltzmann Method Grace et al. [7], Casalino and Lele [8]. Regardless

of the method details, such high-resolution aeroacoustic models require efficient numerical algorithms and utilise large parallel computer resources. The outcome of these simulations typically is big datasets which require expert knowledge for manipulation and analysis.

Hybrid methods based on acoustic analogy

In comparison with the direct computational models, hybrid methods for jet noise based on model decomposition approach are less computer processing intensive. One of the popular approaches is based on the domain decomposition, where the computational region is divided into several (possibly overlapping) sub domains. In each of those sub-domains different governing equations are solved in order to obtain accurate results in each area at a minimum cost. For example, the most expensive part of the model when the Navier-Stokes equations are solved can be restricted to a jet part of the entire solution domain while simplified acoustic propagation equations are solved outside of the jet all the way up to the geometric far-field. This is the approach that formed the idea of the so-called acoustic analogy developed by Lighthill [9], [10]. Lighthill's acoustic analogy is based on an exact re-arrangement of Navier-Stokes equations into a linear propagation operator part and a non-linear source on the right-hand-side. By treating the acoustic source separately from the propagation part and using a reasonable approximation of the source function, the re-arranged equations are solved as a linear problem. In the classical Lighthill acoustic analogy the acoustic propagator at the left-hand side of the equation was chosen to be a simple linear wave equation which is amenable to the elementary Green's function solution. To obtain an analytical solution in a close form and arrive to the celebrated scaling law for jet noise power at the far field, further approximations of the Lighthill theory include assumptions that the jet flow is isotropic, the noise sources are compact, and the temperature and viscosity effects on jet noise are negligible and so is the sound refraction effect. However, as first pointed out by Lilley [11], meanflow refraction effect of sound

waves is very important for jet noise propagation in the small angles to the jet flow which correspond to peak jet noise. For example, ignoring the refraction of the sound waves as they pass through the inhomogeneous jet flow can lead to a significant overestimation of jet noise at high frequencies. Another effect, which was not account for in the Lighthill theory is jet heating. This is important since the exhaust flow of a real aeroengine downstream of a combustor is heated. The effect of temperature on jet turbulence can be significant [12]. As it was suggested in the jet noise literature, the effect of the temperature on jet turbulence can lead to the emergence of dipole-type sources in addition to the quadrupole sources typical of jet noise [13], [14]. Furthermore, in heated jets, the local increase in temperature leads to an increase in the sound speed, which significantly changes jet noise directivity in comparison with the cold jet. After Lighthill, acoustic analogy has been developed by a number of researchers. Most notably, one needs to mention the contribution of Ribner [15] who was the first who discussed the importance of considering the local environment of noise sources and the need to separate the effects associated with the generation and propagation of sound in the flow. In addition, as already mentioned, Lilley [11] made a seminal contribution by taking into account meanflow sound refraction effects and successfully separated the effects of flow-acoustic interaction. Another important contribution is by Ffowcs-Williams [16] who considered the effect of moving sound sources which lead for development of efficient integral surface methods such as Ffowcs Williams - Hawkings method. Finally, the generalised acoustic analogy developed by Goldstein [17] is probably the most complete acoustic analogy formulation uo to date. The generalised acoustic analogy is based on exactly re-arranging the governing Navier-Stokes equations so that the linear hyperbolic part of the governing equations replaces the linear wave propagation part of Lighthill's acoustic analogy. This choice of the acoustic propagator greatly simplifies the sources and makes it possible to consistently subtract the meanflow component from the sources of the generalised acoustic analogy

model. The linear meanflow terms are then explicitly associated with sound propagation. This leads to well-posedness of the acoustic integral in comparison with the previous acoustic analogy formulations which include the meanflow component that does not vanish to zero at the far field. The improve consistency of the Goldstein generalised acoustic analogy model also leads to its lesser sensitivity to errors of the source modelling [18], [5]

Phenomenological approaches

While it is the acoustic analogy method, which is in the focus of the current thesis, alternative hybrid jet noise prediction schemes are discussed in this section. In comparison with acoustic analogy, phenomenological approaches are typically not concerned with the systematic re-arrangement of the governing Navier-Stokes equations but are focused on modelling of a specific phenomenon or a mechanism that is associated with the jet noise physics. Such approaches have their merits. For example, in comparison with the acoustic analogy they are simpler and maybe be more appealing in the case when relevant underlying mechanisms of sound generation can be identified a-priori, which rationalises the modelling of such mechanisms. An example of phenomenological approaches is the two-source model developed by Tam [19]. The two-source model was first inspired by the experimental observations of the role of large-scale coherent structures in jet noise by Crow and Champagne [20]. The second source addressed by the Tam theory is the so-called fine-scale turbulence jet noise which model was developed using the analogy with kinetic gas theory [21]. More recently, the idea of importance of large-scale coherent structures on jet noise has been invigorated in a series of works devoted to the wavepacket theory by Cavalieri et al. [22], Colonius et al. [23], Reba et al. [25] Jordan and Colonius [24]. It can be noted that in comparison with the two-source Tam model, the wavepacket models do not include the fine-scale noise component.

Low order models based on RANS

Regardless of the modelling approach, development of fast turn-around time predictions for jet noise is very important for industrial applications. In this regard, jet noise prediction schemes based on Reynolds Averaged Navier-Stokes (RANS) solutions are popular. Such schemes include both the acoustic schemes which are based on the phenomenological models such as the one developed by Tam and Auriault [21] as well as the methods based on the acoustic analogy.

In the Tam and Auriault model, the acoustic length scale and amplitudes of the source are obtained from the characteristic turbulence length scales and amplitudes using a RANS solution and a set of calibration coefficients based on the far-field noise data. A similar approach is used in many RANS-based acoustic analogy models where the turbulence characteristics are related to the acoustic noise source parameters using some calibration parameters [26], [27], [28]. In some of these models, LES solutions are used to obtain dimensionless parameters of the source amplitudes and scales such as on developed by Karabasov et al. [5].

The existing RANS-based acoustic analogy models differ in terms of their complexity and the underlying assumptions. For example, a simplified version of the Goldstein generalised acoustic analogy method was developed in a series of publications by Khavaran [29], [30]. In the framework of Khavaran model, the effective sound sources are considered in the moving reference frame. This feature leads to additional empirical calibration parameter for estimation of the eddy convection velocity that is a function of the jet velocity at the nozzle exit and the local flow velocity. The strength of the Khavaran model is in its extensive validation on large jet noise datasets from the NASA experiments. In comparison with simpler models like the Tam and Auriault model, the Khavaran model is able to predict jet noise for a range of polar angles including the peak noise direction at small angles to the jet. Furthermore, the Khavaran model is applicable for hot jet noise calculations since it includes both the noise sources based on the fluctuating

Reynolds stresses typical of the cold jets and the enthalpy fluctuations source that is important for heated jets. As already mentioned, most RANS-based jet noise prediction schemes use calibration parameters which need to be obtained from the far-field data. This is because the low-order statistics available from the RANS flow solution, such as time averages and variances, is not sufficient for definition of the acoustic integral that involves higher-order statistical moments.

On the other hand, the required calibration coefficients for the RANS-based acoustic models can be obtained from LES without referring to the far field noise data as shown by Karabasov et al. [5]. For the cold jet, noise predictions of the developed hybrid RANS-LES acoustic model are within 1dB in comparison with the experiment for a range of frequencies and observer angles to the jet. However, one of the questions which remain to be answered is if the temperature effect in heated jets can be included in a similar RANS-LES model as in Karabasov et al. [5]. Furthermore, there is a question if the acoustic source parameters to be extracted from LES for the low-order modelling can be universal in the sense of some non-dimensonalisation of these parameters. That is, it would be useful to reduce the need of having a new LES solution for every jet noise calculation if the RANS-based jet noise prediction scheme is to have a short turn-around time to the solution. To back up this argument, there is some experimental evidence that for a certain category of jets acoustic source parameters can be universal as discussed by Bridges [31]. Both the temperature effect on jet noise and the common non-dimensionalisation of jet noise source parameters are in the focus of the current work. The goal of this thesis is to develop RANS-based jet noise models with taking into account physical complexities such as temperature and dual-stream jet flow effects. The RANS models are based on the standard Computational Fluid Dynamics (CFD) solvers such as ANSYS or Star-CCM+. This choice is motivated by the fact that this software is accessible to the wide range of researchers in academia and in industry in comparison with the LES solvers which use is more

demanding. It is believed that the development of physics-based and fast turn-around-time jet noise models based on RANS, such as the ones considered in this work, can be of benefit for future jet noise studies, especially in the context of Multi-Disciplinary Design Optimisation studies.

Results of the Thesis

1. The effect of jet temperature on noise propagation has been analysed in detail by considering a sound source of similar directivity to that obtained from a validated Large Eddy Simulation of a heated jet flow case. It has been revealed that the temperature effect on propagation is not only important for small angles to the jet flow where refraction effects are maximal but also at 90° angle to the jet flow. The differences due to the variable speed of sound effect in jet noise directivity in comparison with the cold jet are analysed for a range of observer angles, frequencies and source locations.

2. A heated jet noise model has been developed based on generalised acoustic analogy [17]. The model is based on RANS and is informed by LES for reconstruction of dimensionless source strengths. In comparison with the existing models in the literature, the model includes the full directivity of individual noise source components as well as the fluctuating enthalpy source term for heated jet noise modelling. The model validation is performed in comparison with the data of the single-stream cold and heated SILOET jet noise experiment. The model is implemented in a user-friendly programming environment (MATLAB, Octave), which makes it easy to adopt by other researchers working in the same field.

3. A new model of the coaxial heated jet noise has been developed based on the generalised acoustic analogy. The model is based on RANS and is informed

by LES for reconstruction of all dimensionless source parameters. A new concept of reconstruction of all source parameters from a limited number of LES is proposed. The model validation is performed in comparison with the data of the CoJeN experiment for a range of jet temperature and Mach number conditions.

4. For a wide range of high-speed jet flows, which include both the subsonic and supersonic, perfectly expended and under expanded jets, validated RANS solutions have been obtained. The solutions are validated in comparison with the experiment. The RANS solutions provide a useful reference point for a further use in the subsequent jet noise models.

Dissemination

Results of the thesis have been presented in the following articles and conference proceedings:

Articles:

- V. Gryazev, A.P. Markesteijn, and S.A. Karabasov, "Temperature gradient effects on noise propagation in a high-speed hot jet," JSV journal, 2019 (submitted).

- A.P. Markesteijn, S.A. Karabasov, V. Gryazev, R.S.Ayupov L. Benderskiy, and D. Lyubimov, "Flow and Noise Predictions of Coaxial Jets using LES and RANS Methods" AIAA J., 2019 (submitted).

- D. J. Tan, D. Honnery, A. Kalyan, V. Gryazev, S. A. Karabasov, and D. M. Edgington-Mitchell, "Correlation analysis of high-resolution particle image velocimetry data of screeching jets," AIAA J., pp. 163.

- D. J. Tan, D. Honnery, D. M. Edgington-Mitchell, A. Kalyan, V. Gryazev, and S. A. Karabasov, "Equivalent broadband shock-associated noise source reconstruction from particle image velocimetry measurements," AIAA J., pp. 137, 2018.

Conference papers:

- V. Gryazev, A.P. Markesteijn, and S.A. Karabasov, "Low-Order Models of Dual-Stream Jet Noise with Temperature Effects Based on the Goldstein

Generalised Acoustic Analogy," AIAA Aeroacoustics Conference, 20-23 May, Delft, The Netherlands, 2019.

- MA.P. Markesteijn, S.A. Karabasov, V. Gryazev, R.S.Ayupov L. Benderskiy, and D. Lyubimov, "Comparison of GPU CABARET, RANS and RANS/ILES High Resolution Method Solutions for the CoJeN Jet Noise Experiment", 25th AIAA/CEAS Aeroacoustics Conference (Aeroacoustics 2019), 20 - 23 May 2019, Delft, The Netherlands, AIAA 2019-2446.

- V. Gryazev, A.P. Markesteijn, and S.A. Karabasov, "Temperature effect on the apparent position of effective noise sources in a hot jet," AIAA Aeroacoustics Conference, 25-29 June, Atlanta, 2018.

- V. Gryazev, A.P. Markesteijn, and S.A. Karabasov, "Comparison of two Goldstein acoustic analogy implementations with the Tam&Auriault model for heated and unheated jet noise prediction" AIAA Aeroacoustics Conference, 25-29 June, Atlanta, 2018.

- D. J. Tan, A. Kalyan, V. Gryazev, M. Wong, Daniel M Edgington-Mitchell, and S. A. Karabasov, "On the application of shock-associated noise models to piv measurements of screeching axisymmetric cold jets," 23rd AIAA/CEAS Aeroacoustics Conference, 2017.

- A. Kalyan, V. Gryazev, S.A. Karabasov, D.J. Tan, M. Wong, D. Honnery, D. Edgington-Mitchell, "Improved predictions of broadband shock associated noise in supersonic jets.," INTER-NOISE and NOISE-CON Congress and Conference Proceedings 255 (6), 1338-1349, 2017.

In addition, the work has been reported at the following workshops.

Presentations:

- V. Gryazev., Physics based predictions of coaxial jet noise., Russell Binions Memorial PhD Research Symposium., 23 April 2019.

Posters:

- V. Gryazev., Karabasov, S.A., Hot Jet Noise Modelling., The SEMS Industrial Liaison Forum, 14 November 2018.

Chapter 1

Governing mathematical formulations

1.1 Acoustic Analogy

The study of jet noise naturally begins with the acoustic analogy formulation of Lighthill [9], which main derivations are outlined in this Section. Compressible Navier-Stokes equations for density ρ and momentum ρv are considered:

$$\frac{\partial}{\partial t}\rho + \frac{\partial}{\partial x_i}\rho v_i = 0, \tag{1.1}$$

$$\frac{\partial}{\partial t}\rho v_i + \frac{\partial}{\partial x_j}\rho v_j v_i = -\frac{\partial R_{ij}}{\partial x_j}, \tag{1.2}$$

where $R_{ij} = p\delta_{ij} - \sigma_{ij}$ is a stress tensor, σ_{ij} is a viscous part of the stress tensor. By taking the time derivative of (1.1)

$$\frac{\partial^2}{\partial t^2}\rho + \frac{\partial^2}{\partial x_i \partial t}\rho v_i = 0 \tag{1.3}$$

and subtracting the divergence of the momentum equation (1.2)

$$\frac{\partial^2}{\partial x_i \partial t}\rho v_i + \frac{\partial^2}{\partial x_i \partial x_j}\rho v_i v_j = -\frac{\partial^2 R_{ij}}{\partial x_i \partial x_j} \tag{1.4}$$

one obtains

$$\frac{\partial^2}{\partial t^2}\rho = \frac{\partial^2}{\partial x_i \partial x_j}\rho v_i v_j + \frac{\partial^2}{\partial x_i \partial x_i}p - \frac{\partial^2}{\partial x_i \partial x_j}\sigma_{ij}. \tag{1.5}$$

By adding to the both sides of the equation the term $-c_\infty^2 \frac{\partial^2 \rho}{\partial x_i \partial x_i}$, the non-homogeneous wave equation is obtained:

$$\frac{\partial^2 \rho}{\partial t^2} - c_\infty^2 \frac{\partial^2 \rho}{\partial x_i \partial x_i} = q(\mathbf{x}, t), \tag{1.6}$$

where

$$q(\mathbf{x}, t) = \frac{\partial^2}{\partial x_i \partial x_j}\left(\rho v_i v_j + (p - c_\infty^2 \rho)\delta_{ij} - \sigma_{ij}\right) = \frac{\partial^2}{\partial x_i \partial x_j} T_{ij}. \tag{1.7}$$

Here T_{ij} is so-called Lighthill stress tensor which represents all the non-linear terms of the Navier-Stokes equations as well as the linear terms which are not included in the wave equation.

Using the relation $p = \rho \cdot c_\infty^2$ which is true for isotropic gas dynamics, one obtains

$$\frac{\partial^2 p}{\partial t^2} - c_\infty^2 \frac{\partial^2 p}{\partial x_i \partial x_i} = c_\infty^2 \cdot q(\mathbf{x}, t). \tag{1.8}$$

It can be noted that in this exact form acoustic analogy contains the unknown both in the right-hand side and the left-hand side of the equation. Hence, to make it solvable, the major assumption of the Lighthill theory is to neglect the effect of the acoustic variable in the source term. By doing so, the source becomes decoupled from the propagation and the equation becomes linear with respect to the acoustic variable. Under this assumption, the resulting linear wave equation has an elementary solution using the Green's function method so long as the source function is known or can be approximated with a reasonable accuracy.

Figure (1.1) illustrates the idea of underlying flow solution decomposition

implied in acoustic analogies. In this framework, acoustic sources are considered inside the jet flow whereas the process of sound propagation outside the jet is considered as a linear problem.

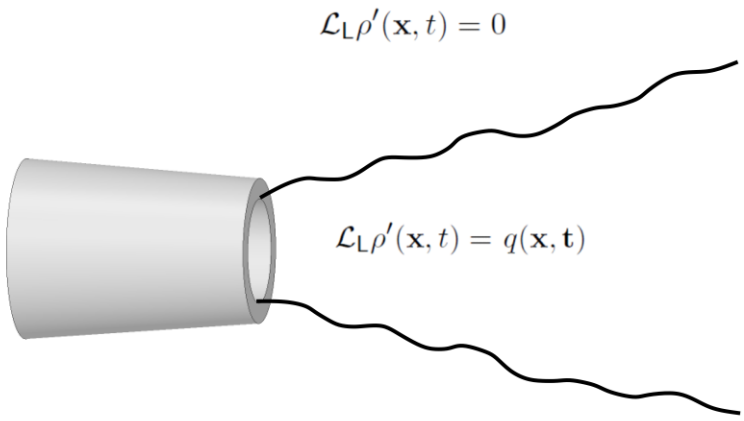

Figure 1.1: Schematic of the domain decomposition in acoustic analogies.

Having assumed that the source is obtained separately from the acoustic variable, the acoustic analogy equation can be solved via the Green's function method.

Let's introduce the Green's function $G(\mathbf{x},t;\mathbf{y},\tau)$ which satisfies the linear wave equation

$$\left(\frac{\partial^2}{\partial t^2}-c_\infty^2\cdot\frac{\partial^2}{\partial x_i\partial x_i}\right)G=\delta(\mathbf{x}-\mathbf{y})\delta(t-\tau),\quad G\big|_{t<0}=0. \tag{1.9}$$

The Green's function solution is given by [32]

$$G(\mathbf{x},t;\mathbf{y},\tau)=\frac{1}{4\pi}\frac{1}{|\mathbf{x}-\mathbf{y}|}\delta\left(t-\tau-\frac{|\mathbf{x}-\mathbf{y}|}{c_\infty}\right). \tag{1.10}$$

Hence, the solution of equation (1.8) follows as

$$p(\mathbf{x},t)=\frac{1}{4\pi}\int_V\frac{1}{|\mathbf{x}-\mathbf{y}|}q\left(\mathbf{y},t-\frac{|\mathbf{x}-\mathbf{y}|}{c_\infty}\right)d^3\mathbf{y}, \tag{1.11}$$

where $\mathbf{y}$ is the source coordinate, $\mathbf{x}$ is the location of the observer.

The computed far-field sound pressure can be converted to the sound power that is a statistically averaged quantity in comparison with the pressure variable. Furthermore, by using the Parseval theorem, the following relation between the variance of acoustic pressure and another useful quantity, the power spectral density can be obtained

$$\int_{-\infty}^{+\infty} \overline{p'(\mathbf{x},t)^2} dt = \frac{1}{2\pi} \int_{-\infty}^{+\infty} \hat{P}(\mathbf{x},\omega)\, d\omega, \quad p'(\mathbf{x},t) = p(\mathbf{x},t) - \overline{p}, \tag{1.12}$$

where $\hat{\psi}(\omega) = \int_{-\infty}^{+\infty} \psi(t) e^{-\mathrm{i}\omega t}\, dt$ denotes the Fourier transform, $\omega = 2\pi f$ is angular frequency, f is frequency [s^{-1}]. Following the accepted convention in acoustics, the power spectral density is typically represented as sound pressure levels in the logarithmic scale,

$$\mathrm{PSD} = 10 \cdot \log_{10}(\hat{P}(\mathbf{x},\omega)/p_{ref}/f_{ref}), \tag{1.13}$$

where the reference pressure $p_{ref} = 2 \cdot 10^{-5}$[Pa] and the reference frequency $f_{ref} = 1$ [Hz].

It can be noted that the acoustic integral (1.11) cannot be evaluated fully analytically in a general case. However, using some simplified assumptions, as was done by Lighthill. For example, to the first approximation, the effect of the viscosity of the fluid can be neglected and the flow is assumed to be homogeneous. Secondly, all linear propagation effects associated with the meanflow refraction can also be neglected. Thirdly, the density of the medium in the jet is assumed to be constant and equal to the density of the environment, thereby all the temperature effects on turbulence are not considered. Lastly, it can be assumed that sound fluctuations are mainly generated by acoustically compact vortices whose size is much smaller than the length of acoustic waves. Under all these assumptions, the acoustic integral can be evaluated and the celebrated Lighthill's v^8scaling law for

jet noise power is obtained

$$W \propto \rho_0 L^2 v^8 c_\infty^{-5}. \tag{1.14}$$

Remarkably, despite the many assumptions some of which are very questionable, the experimental studies have confirmed the validity of the v^8power law on average for a large range of high-speed jets despite some deviations at high-frequencies and for heated jets [12].

One of the important effects which was neglected in the framework of the classical Lighthill acoustic analogy is the meanflow sound propagation. For example, due to the presence of the meanflow velocity gradient in the jet mixing region, the radiated sound waves are strongly affected by refraction especially in high-speed jets and for propagation at small angles to the jet flow [11]. Secondly, jet temperature has a well-known effect on jet mixing noise in heated jets. Heat modifies jet turbulence by affecting the turbulent fluctuating Reynolds stresses as well as generating additional noise sources such as those associated with the fluctuating temperature and entropy [12]. Furthermore, the presence of temperature gradients also affects noise propagation. However, in the classical Lighthill acoustic analogy all these effects are hidden in the effective noise source, hence, difficult to model accurately. Notably, both the meanflow sound propagation and the temperature effects are explicitly included in the Goldstein generalised acoustic analogy that has been selected as the basis for the acoustic modelling work in the current thesis.

1.2 Generalised acoustic analogy

In this section the generalised acoustic analogy developed by Goldstein is outlined. Following [17] density, pressure, velocity and enthalpy are decomposed into mean and fluctuating parts

$$\rho = \bar{\rho} + \rho', \quad p = \bar{p} + p', \quad v_i = \tilde{v}_i + v_i'', \quad h = \tilde{h} + h'', \tag{1.15}$$

where bar represents a time average, tilde stands for Favre averaged and single and double primes represent fluctuations. The idea of Goldstein's acoustic analogy is to exactly rearrange the full set of Navier-Stokes equations including the energy part in such a way that the linear propagation part corresponds to the linear hyperbolic part of the governing equations. The effective sources which arise on the right-handside correspond to fluctuating stresses due to the nonlinear terms in the equations of momentum and energy:

$$\frac{\partial \rho'}{\partial \tau} + \frac{\partial}{\partial y_j}(\rho' \tilde{v}_j + u_j) = 0, \tag{1.16}$$

$$\frac{\partial u_i}{\partial \tau} + \frac{\partial}{\partial y_j}(\tilde{v}_j u_i) + \frac{\partial p'}{\partial y_i} + u_j \frac{\partial \tilde{v}_i}{\partial y_j} - \frac{\rho'}{\bar{\rho}} \frac{\partial \tilde{\tau}_{ij}}{\partial y_j} = \frac{\partial T'_{ij}}{\partial y_j}, \tag{1.17}$$

$$\frac{1}{\gamma - 1}\left(\frac{\partial p'}{\partial \tau} + \frac{\partial}{\partial y_j}\left(p' \tilde{v}_j\right)\right) + \frac{\partial}{\partial y_j}\left(u_j \tilde{h}\right) + p' \frac{\partial \tilde{v}_j}{\partial y_j} - \frac{u_i}{\bar{\rho}} \frac{\partial \tilde{\tau}_{ij}}{\partial y_j} = Q, \tag{1.18}$$

where $i, j = 1, 2, 3$; $\mathbf{y} = (y_1, y_2, y_3) \in \mathbb{R}^3$; $u_i = \rho v'_i$, τ_{ij} is the viscous stress term; Here the enthalpy fluctuations are

$$\tilde{h}_0 = \tilde{h} + \frac{1}{2}\tilde{v}^2, \quad h'_0 = h' + \tilde{v}_i v'_i + \frac{1}{2} v'^2, \tag{1.19}$$

and the sources at the right-hand side are given by

$$T'_{ij} = -(\rho v'_i v'_j - \bar{\rho} \widetilde{v'_i v'_j}), \tag{1.20}$$

$$Q = -\tilde{v}_j \frac{\partial T'_{ij}}{\partial y_i} + \frac{1}{2}\delta_{ij}\left[\frac{DT'_{ij}}{D\tau} + \frac{\partial \tilde{v}_k}{\partial y_k} T'_{ij}\right] - \frac{\partial}{\partial y_j}\left(\rho v'_j h'_0 - \bar{\rho} \widetilde{v'_j h'_0}\right), \tag{1.21}$$

where $D/D\tau$ is the substantial derivative,

$$\frac{D}{D\tau}\frac{\partial}{\partial \tau} + \tilde{v}_j(\mathbf{y}) \frac{\partial \tilde{\tau}_{ij}}{\partial y_j}, \quad \frac{\partial \tilde{\tau}_{ij}}{\partial y_j} = -\frac{\partial}{\partial y_j}\left(\bar{\rho} \tilde{v}_i \tilde{v}_j\right). \tag{1.22}$$

The resulting linearised Euler equations can be solved by introducing the matrix Green's function [32] $\mathbf{G} = (G_{\mu k})$. The matrix Green's function corresponds to the

solution of the system of the same linearised equations with a vector delta-function on the right-hand side:

$$\frac{\partial G_{0k}}{\partial \tau} + \frac{\partial}{\partial x_j}(G_{0k}\tilde{v}_{jk} + G_{jk}) = 0, \tag{1.23}$$

$$\frac{\partial G_{ik}}{\partial \tau} + \frac{\partial}{\partial x_j}(\tilde{v}_j G_{ik}) + \frac{\partial G_{4k}}{\partial x_i} + G_{jk}\frac{\partial \tilde{v}_i}{\partial x_j} - \frac{G_{0k}}{\bar{\rho}}\frac{\partial \tilde{\tau}_{ij}}{\partial x_j} = \delta_{ik}\cdot\delta(\mathbf{x}-\mathbf{y}, t-\tau), \tag{1.24}$$

$$\frac{1}{\gamma-1}\left(\frac{\partial G_{4k}}{\partial \tau} + \frac{\partial}{\partial x_j}(G_{4k}\tilde{v}_j)\right) + \frac{\partial}{\partial x_j}(G_{jk}\tilde{h}) + G_{4k}\frac{\partial \tilde{v}_j}{\partial x_j} - \frac{G_{ik}}{\bar{\rho}}\frac{\partial \tilde{\tau}_{ij}}{\partial x_j} = \delta_{4k}\cdot\delta(\mathbf{x}-\mathbf{y}, t-\tau). \tag{1.25}$$

The resulting solution of linearised Euler equations (1.23)–(1.25)

$$\mathbf{f}(\mathbf{x}, t) = (f_\mu(\mathbf{x}, t)) = (\rho', u_1, u_2, u_3, p'), \quad \mu = 0, 1, 2, 3, 4 \tag{1.26}$$

can be written as follows

$$f_\mu(\mathbf{x}, t) = \int_V \int_{-\infty}^{+\infty} G_{\mu k}(\mathbf{x}, t; \mathbf{y}, \tau) q_k(\mathbf{y}, t)\, d^3\mathbf{y}\, d\tau, \tag{1.27}$$

where the source vector is

$$\mathbf{q}(\mathbf{y}, t) = (q_k(\mathbf{y}, t)) = \left(0, \frac{\partial T'_{1j}}{\partial y_j}, \frac{\partial T'_{2j}}{\partial y_j}, \frac{\partial T'_{3j}}{\partial y_j}, Q\right), \quad k = 0, 1, 2, 3, 4. \tag{1.28}$$

In result, the far-field acoustic pressure can be calculated as a convolution product of the sources with the corresponding components of the matrix Green's function:

$$p'(\mathbf{x}, t) = \int_V \int_{-\infty}^{+\infty} G_{4k}(\mathbf{x}, t; \mathbf{y}, \tau) q_k(\mathbf{y}, t) d^3\mathbf{y} d\tau. \tag{1.29}$$

1.3 Adjoint formulation

The matrix Green's function calculation is computationally expensive because for every far field source location one has to solve the acoustic equations many times.

However, in many cases it is only the pressure variable which is required in the far field (1.29). Moreover, it is only relatively a few microphone positions which are of interest. An elegant way of solving the same problem is to apply the adjoint Green's function technique following [33]. In accordance with adjoint Green's function method the source and the observer position exchange their places, as illustrated in Figure (1.2).

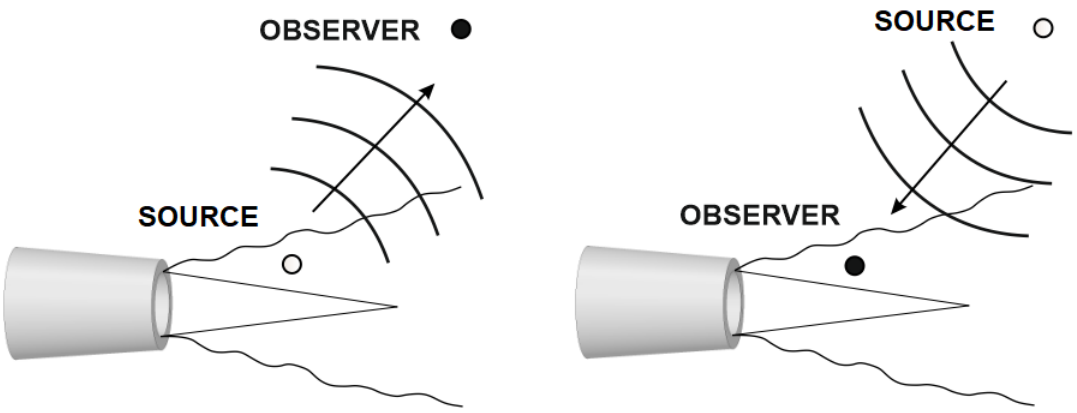

Figure 1.2: Schematic representation of adjoint formulation.

The adjoint vector Green's function is introduced,

$$\mathbf{G}^a(\mathbf{y},\tau;\mathbf{x},t) = (G_k^a), \quad k = 0, 1, \ldots 4, \tag{1.30}$$

where $G_k^a(\mathbf{y},\tau;\mathbf{x},t) = G_{4k}(\mathbf{x},t;\mathbf{y},\tau)$, and which is defined together with the adjoint operator $\mathcal{L}_{\mu k}^*$ using the reciprocity condition

$$\int_V (\mathcal{L}_{\mu k}^*)_{\mathbf{y}} G_k^a \cdot G_{4\mu}\, d^3\mathbf{y} = \int_V G_k^a \cdot (\mathcal{L}_{\mu k})_{\mathbf{y}} G_{4\mu}\, d^3\mathbf{y} + I_0 + I_\infty. \tag{1.31}$$

Here I_0 and I_∞ are boundary conditions at the nozzle boundary and at infinity

respectively. In free-jet cases, the boundary integrals are zero $I_0 = I_\infty = 0$.

Having defined the adjoint operator, the vector adjoint Green's function is found as a solution of the following equation

$$(\mathcal{L}^*_{\mu k})_{\mathbf{y},\tau} G^a_k(\mathbf{y},\tau;\mathbf{x},t) = \delta_{\mu 4}\cdot\delta(\mathbf{x}-\mathbf{y})\delta(t-\tau), \tag{1.32}$$

which in expanded form is given by

$$\mathrm{i}\omega\hat{G}^a_0 + \tilde{v}_j\frac{\partial\hat{G}^a_0}{\partial y_j} + \frac{\hat{G}^a_i}{\bar{\rho}}\frac{\partial\tau_{ij}}{\partial y_j} = 0, \tag{1.33}$$

$$\mathrm{i}\omega\hat{G}^a_j + \frac{\partial\hat{G}^a_0}{\partial y_j} + \tilde{v}_i\frac{\partial\hat{G}^a_j}{\partial y_i} - \hat{G}^a_i\frac{\partial\tilde{v}_i}{\partial y_j} + \tilde{h}\frac{\partial\hat{G}^a_4}{\partial y_j} + \frac{\hat{G}^a_4}{\bar{\rho}}\frac{\partial\tau_{ij}}{\partial y_i} = 0, \tag{1.34}$$

$$\frac{\mathrm{i}\omega}{\gamma-1}\hat{G}^a_4 + \frac{\tilde{v}_j}{\gamma-1}\frac{\partial\hat{G}^a_4}{\partial y_j} - \hat{G}^a_4\frac{\partial\tilde{v}_j}{\partial y_j} + \frac{\partial\hat{G}^a_j}{\partial y_j} = \delta(\mathbf{y}-\mathbf{x}). \tag{1.35}$$

Here $\hat{G}^a_k(\mathbf{y},\omega;\mathbf{x})$ is the frequency domain adjoint vector Green's function. The expression for the far-field power spectral density in the generalised acoustic analogy model is given by

$$\hat{P}(\mathbf{x},\omega) = \int_V\int_V \hat{R}_{\mu jkl}(\mathbf{y},\boldsymbol{\Delta},\omega)\hat{I}_{\mu j}(\mathbf{y},\omega;\mathbf{x})\hat{I}^*_{kl}(\mathbf{y}+\boldsymbol{\Delta},\omega;\mathbf{x})\,d^3\boldsymbol{\Delta}\,d^3\mathbf{y}. \tag{1.36}$$

Here the Fourier transform of the generalized stress tensor auto-covariance is used so that

$$\hat{R}_{\mu jkl}(\mathbf{y},\boldsymbol{\Delta},\omega) = \int R_{\mu jkl}(\mathbf{y},\boldsymbol{\Delta},\tau)e^{-i\omega\tau}d\tau = \int \overline{e''_{\mu j}(\mathbf{y},\tau)e''_{kl}(\mathbf{y}+\boldsymbol{\Delta},t+\tau)}e^{-i\omega\tau}d\tau, \tag{1.37}$$

where the overbar means averaging over time t, $i,j = 1,2,3$, $\mu,k = 1,2,3,4$, and the so-called generalized stresses, $e''_{\mu j}$ are

$$e''_{\mu j} = e'_{\mu j} - \overline{e'_{\mu j}}, \quad \tilde{\theta}_{\mu j} = \delta_{\mu j}\bar{p}_e - \overline{e'_{\mu j}} \tag{1.38}$$

$$e'_{\mu j} = -\rho v'_\mu v'_j + \delta_{\mu j}\frac{\gamma-1}{2}v'^2 + (\sigma_{\mu j} + (\gamma-1)\delta_{\mu 4}\sigma_{jk}v'_k)\,, \tag{1.39}$$

$$v'_4 = (\gamma-1)\left(h' + \frac{1}{2}v'^2\right) = (c^2)' + \frac{\gamma-1}{2}v'^2, \tag{1.40}$$

$$\sigma'_{4j} = -(\gamma-1)q_j. \tag{1.41}$$

The propagation operator that appears in the convolution integral (1.36) is given by

$$\hat{I}_{ij}(\mathbf{y},\omega;\mathbf{x}) = \frac{\partial \hat{G}^a_j}{\partial y_i} - \frac{\partial(\tilde{v}_j \hat{G}^a_4)}{\partial y_i} + \frac{\delta_{ij}}{2}\left(-\mathrm{i}\omega\hat{G}^a_4 + \tilde{v}_k\frac{\partial \hat{G}^a_4}{\partial y_k}\right), \tag{1.42}$$

$$\hat{I}_{i4}(\mathbf{y},\omega;\mathbf{x}) = \frac{\partial \hat{G}^a_4}{\partial y_i}, \tag{1.43}$$

which depends on the adjoin Green's function compoments.

1.4 Solving the mean flow sound propagation using the Green's function method

The Adjoint vector Green's function is obtained by solving the locally parallel flow equations with the coefficients defined from the RANS flow solution. The process of obtaining the RANS solution as well as the description of the jet cases considered in the present work will be discussed in Chapter 2.

A cylindrical-polar coordinate system $\mathbf{y} = (x, r\cos\theta, r\sin\theta)$ is considered and schematically illustrated in Figure (1.3), where x axis coincide with jet centre line, r is the distance to the axis of the jet. The centre of coordinates coincides with the centre of the nozzle, whose diameter is D_j. The position of the observer in spherical coordinates $\mathbf{x} = (R\cos\phi, R\sin\phi, 0)$.

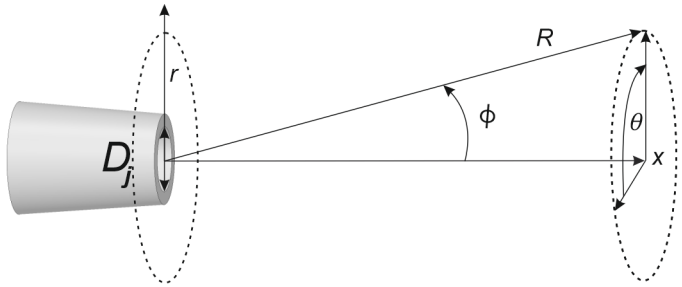

Figure 1.3: Definition of the cylindrical-polar coordinate system.

It can be assumed that the jet flow field changes in the axial direction very slowly in comparison with radial so the influence of axial gradients can be neglected. This approximation is equivalent to the introduction of a locally parallel shear whcih as schematically illustrated in Figure (1.4).

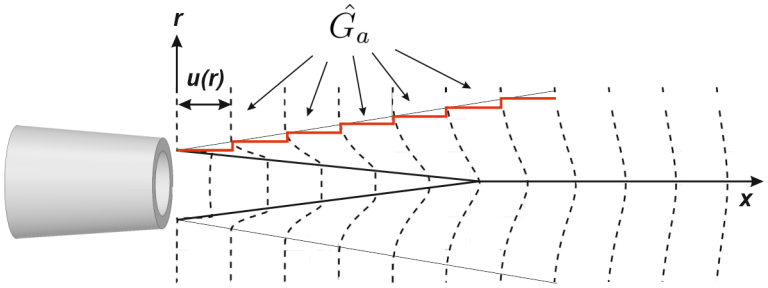

Figure 1.4: Schematic representation of locally parallel flow.

In accordance with the locally parallel approximation, the jet flow is represented as a series of piece-wise parallel jet profiles. For each axial jet location, x, jet velocity is a function of radius only $\tilde{\mathbf{v}} = (\tilde{u}(r), 0, 0)$ and so is the speed of sound $\tilde{c^2} = \tilde{c^2}(r)$. For $r \to \infty$, the following static conditions are assumed: $\tilde{u}(r) \to 0$ and $\tilde{c^2}(r) \to c_\infty^2$, where c_∞ is ambient speed of sound. Let $|\mathbf{x} - \mathbf{y}|$ be the distance from a source centred at a point $\mathbf{y} = (x, r\cos\theta, r\sin\theta)$ to the observer

$\mathbf{x} = (R\cos\phi, R\sin\phi, 0)$. The free space Green's function solution [32] is given by:

$$\hat{G}^a_{4\infty} = \frac{\mathrm{i}\omega e^{\mathrm{i}k|\mathbf{x}-\mathbf{y}|}}{4\pi c^2|\mathbf{x}-\mathbf{y}|}, \tag{1.44}$$

where $c = c_\infty$, $k = \omega/c$ is the acoustic wave number.

If one assumes that $r \ll R$, which corresponds to the geometrical far-field, then

$$|\mathbf{x}-\mathbf{y}| \approx |\mathbf{x}| = R$$

and

$$|\mathbf{x}-\mathbf{y}| \approx |\mathbf{x}| - \frac{\mathbf{x}}{|\mathbf{x}|}\cdot\mathbf{y} = R - x\cos\phi - r\cos\theta\sin\phi,$$

which implies the solution corresponding to the plane wave:

$$\hat{G}^a_{4\infty} = \frac{\mathrm{i}\omega}{4\pi c^2 R} e^{\mathrm{i}k(R - x\cos\phi - r\cos\theta\sin\phi)}. \tag{1.45}$$

By using the well-known formula [32] of the plane wave expansion into cylindrical Bessel functions,

$$e^{-\mathrm{i}\lambda r\cos\theta} = \sum_{n=0}^{\infty} (-\mathrm{i})^n \varepsilon_n J_n(\lambda r)\cos n\theta, \tag{1.46}$$

where

$$\varepsilon_n = \begin{cases} 1, & n = 0, \\ 2, & n \geq 1, \end{cases} \tag{1.47}$$

the adjoint Green's function is transformed to the cylindrical-polar coordinates,

$$\hat{G}^a_4 = \frac{\mathrm{i}\omega}{4\pi c^2 R} e^{\mathrm{i}k(R - x\cos\phi)} \sum_{n=0}^{\infty} f_n(r)\cos n\theta, \tag{1.48}$$

where the Fourier coefficients f_n satisfy the Rayleigh-type equation for the adjoint

Green's function which are the base functions for the Rayleigh-type equation

$$\frac{d^2 f_n}{dr^2} + A\frac{df_n}{dr} + B_n f_n = 0, \quad A = \frac{1}{r} + \frac{1}{\widetilde{c^2}}\frac{d\widetilde{c^2}}{dr}, \tag{1.49}$$

$$B_n = \frac{\omega'^2}{\widetilde{c^2}} - k'^2 - \frac{k'}{\omega'}\left(A\frac{d\tilde{u}}{dr} + 2\frac{k'}{\omega'}\left(\frac{d\tilde{u}}{dr}\right)^2 + \frac{d^2\tilde{u}}{dr^2}\right) - \frac{n^2}{r^2}, \tag{1.50}$$

$$k' = k\cos\phi, \quad \omega' = \omega - \tilde{u}k'.$$

Details of the derivation of the equations (1.49)–(1.50) are presented in Appendix A.

It should be noted that equations (1.49)–(1.50) are well-posed in case the denominator is nonzero, i.e. when $\omega' > 0$, which corresponds to a subsonic jet flow. In the case of the supersonic jet this value becomes singular, which leads to the critical layer problem that will be discussed in Section 1.6.

For a piece-wise constant jet flow field, i.e. the plug flow approximation, in each part of the solution domain, $\tilde{u} = \text{const}$ and $\tilde{c^2} = \text{const}$, the Fourier coefficient equation reduces to the Bessel equation [32]

$$\frac{d^2 f_n}{dr^2} + \frac{1}{r}\frac{df_n}{dr} + \left(\lambda^2 - \frac{n^2}{r^2}\right) f_n = 0. \tag{1.51}$$

A particular solution to this equation can be found in the form $f_n(r) = C_1 J_n(\lambda r) + C_2 H_n^{(1)}(\lambda r)$. By imposing the Neumann condition at zero radius and the Sommerfeld radiation condition at infinity one obtains:

$$f_n(r) \approx \begin{cases} a_0 J_n(\lambda_0 r), & r \to 0, \\ (-\mathrm{i})^n \varepsilon_n J_n(\lambda_\infty r) + a_1 H_n^{(1)}(\lambda_\infty r), & r \to R_\infty, \end{cases} \tag{1.52}$$

where J_n and $H_n^{(1)}$ are Bessel and Hankel functions, respectively; λ_0, a_0, a_1 are some constants; $\lambda_\infty = k\sin\phi$; R_∞ sets the size of the computational domain (in diameters D_j).

In the plug-flow case, the solution can be founded analytically and is presented in Appendix B.

1.5 Numerical solution for the Green's function

In this section numerical procedure will be discussed and verified with analytical solution in the case of piece-wise constant velocity and speed of sound profiles. The locally parallel equations (1.49)–(1.50)

$$\frac{d^2 f_n}{dr^2} + A\frac{df_n}{dr} + B_n f_n = 0, \tag{1.53}$$

are approximated with the standard central second-order finite-difference scheme. The resulting tridiagonal matrix is solved with an implicit scheme in MATLAB using a sparse matrix library. In the numerical solution, the infinite domain $r \in [0, +\infty)$ is truncated to $r \in [0, R_\infty]$ with a sufficiently large R_∞ outside of which the mean flow velocity is zero.

$$\tilde{u}_e = 0, \quad \tilde{c}_e = c, \quad \tilde{u}_i = \text{const}, \quad \tilde{c}_i = \text{const}.$$

For the boundary conditions, the following asymptotic expression is assumed at the origin $J_n(r) = c_n r^n + O(r^{n+2})$, where c_n is a constant, therefore

$$\begin{cases} f_n'(0) = 0, & n = 0, \\ f_n(0) = 0, & n \geq 1. \end{cases}$$

For $r = R_\infty$ with ε_n, $\lambda_\infty = k \sin\phi$ one obtains

$$\begin{aligned} &\lambda_\infty (H_n^{(1)})'(\lambda_\infty R_\infty) f_n(R_\infty) - H_n^{(1)}(\lambda_\infty R_{\infty 0}) f_n'(R_\infty) \\ &= \lambda_\infty A_n \left\{ J_n(\lambda_\infty R_\infty)(H_n^{(1)})'(\lambda_\infty R_\infty) - J_n'(\lambda_\infty R_\infty) H_n^{(1)}(\lambda_\infty R_\infty) \right\} = \frac{2\mathrm{i} A_n}{\pi R_\infty}. \end{aligned} \tag{1.54}$$

For validation of the numerical solution, a sequence of parallel flow profiles is considered with tending the width of the shear and thermal layer to zero and comparing the results with the analytical plug-flow solution as shown in Figure (1.5). Results of comparison between the locally parallel solutions at different shear layer widths and the analytical solution for the four relevant components of the adjoint Green's function (the adjoint density component is identically zero for the parallel flow problem) are shown in Figures (1.6) and (1.7) . The figures correspond to 30° and 90° polar angles to the jet flow, respectively, Strouhal number based on the jet velocity and diameter $St = 2$, and the azimuthal mode number $n = 1$ and $n = 2$. Results for other angles, frequencies, and azimuthal model numbers show a similar excellent agreement with the analytical solution for the smallest width of the jet shear and the thermal layer.

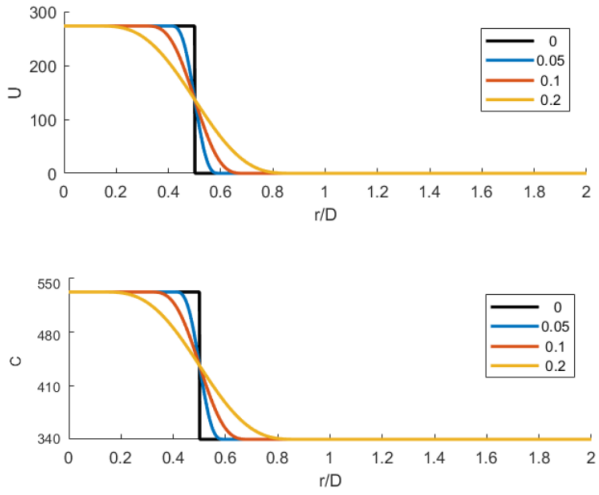

Figure 1.5: Input jet velocity profile (top) and speed of sound (bottom) profiles.

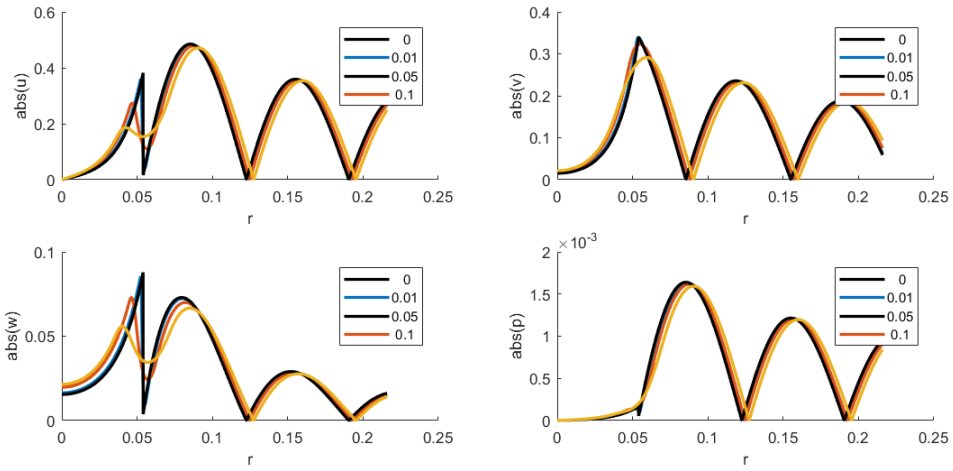

Figure 1.6: Numerical and analytical solutions for the azimuthal mode number n=1; St=2; $\phi = 30°$.

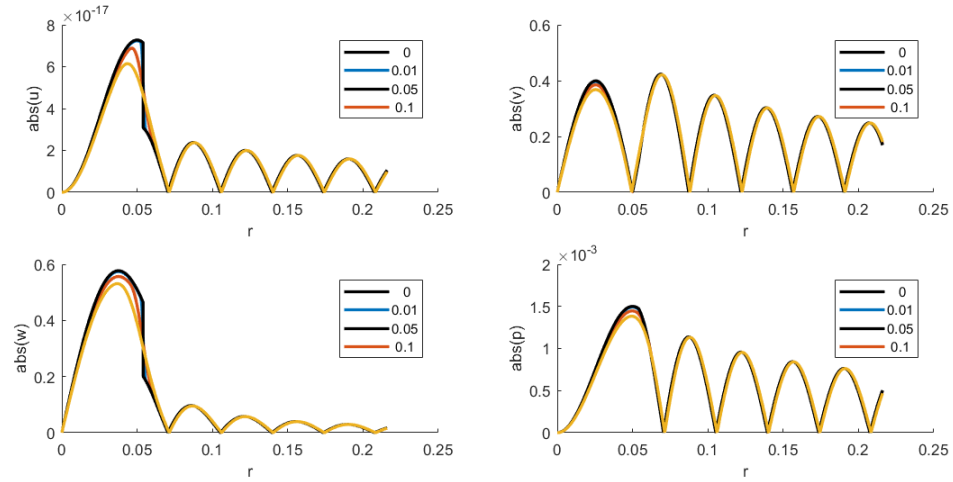

Figure 1.7: Numerical and analytical solutions for the azimuthal mode number $n = 2$; St=2; $\phi = 90°$.

1.6 Critical layer

As noted, for supersonic flows, the coefficients of the governing Rayleigh-type equation become singular. The problem occurs when acoustic Mach number becomes

greater than unity, a crytical layer singularity point emerges at small polar angles where , $\frac{\tilde{u}}{c_\infty}\cos\phi = 1$, thus, leading to $\omega' = 0$. Following [28], the correct treatment of the critical layer singularity is based on the idea of considering first-order non-parallel effects in the shear layer and consists of two parts in accordance with the following algorithm:

1) Shift the integration contour in the complex plane to avoid the singular point by using a modified expression for the axial wavenumber in the vicinity of the singular point along the radial coordinate

$$k' = \frac{\omega}{c_\infty}\cos\phi \cdot (1 - \mathrm{i} \cdot f(r - r_c)), \tag{1.55}$$

where $f(r - r_c)$ is a real function that takes a small value in the vicinity of the critical layer point, and zero otherwise. For example, $f(r - r_c) = \varepsilon$, if $|r - r_c| < r_0$ and $f(r - r_c) = 0$, else, where $0 < \frac{r_c}{D_j} \ll 1$ and $0 < \varepsilon \ll 1$ are some small numerical parameters. The modified wavenumber expression is substituted into the cylindrical wave expansion (1.48) that is followed integrating the modified equation (1.49), (1.50) where all coefficients are well-defined now.

2) Apply a weakly non-parallel correction in the acoustic integrals. The correction corresponds to several multiplication factors for each term of the acoustic integrand, which can be derived from asymptotic expansion analysis, and which details can be found in [28].

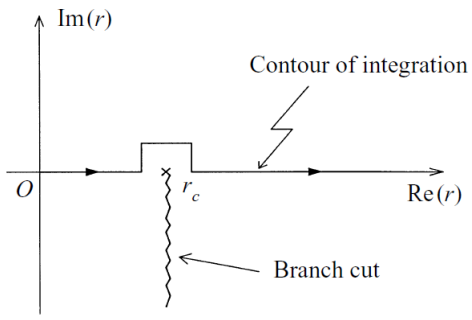

Figure 1.8: Modified integration contour in the complex plane to avoid critical layer singularity [33].

Summary

In this Chapter, the theoretical background of acoustic analogy has been reviewed along with introducing the main definitions and mathematical formulations. This includes classical Lighthill acoustic analogy as well as the modern approach such as the generalised acoustic analogy developed by Goldstein. In comparison with classical Lighthill approach, in the framework of the generalised acoustic analogy it is possible to consistently separate the meanflow terms from the effective sources thus enabling a consistent treatment of the temperature and propagation effects which are in focus of this thesis.

Direct and adjoint Green's function methods for solution of the sound propagation problem have been reviewed. It has been pointed out that adjoint Green's function formultion can lead to significant savings in computational resources which is an important factor for fast turn-around-time jet noise prediction models considered in the present work.

The solution of sound propagation problem in a locally parallel jet flow has been reviewed. This model is sufficiently complex to include a variation of both the local velocity and the temperature in the jet as well as the critical layer correction to include supersonic jets into consideration. On the other hand, the model is

sufficiently simple to allow for a fast semi-analytical solution, which is implemented in MATLAB. The solution has been validated for a set of plug-flow like jet profiles in comparison with the analytical solution corresponding to the limiting case of zero shear layer and thermal layer thickness.

Chapter 2

CFD Modelling

2.1 Flow field modelling

As discussed in Chapter 1, the right-hand side of the acoustic analogy equations, as well as the meanflow coefficients, require input from the Navier-Stokes solution. This solution is obtained using Computational Fluid Dynamics (CFD) in the framework of the Reynolds Averaged Navier-Stokes (RANS) model. In this chapter, RANS solutions for the three nozzle geometries will be considered which correspond to the Roll-Royce SILOET jet experiment [34], the CoJeN jet experiment [35], and the LTRAC jet experiment [36]. Nozzle geometries were parametrically created in SOLIDWORKS CAD package [37] and imported into ICEM grid generation system [38]. For RANS solution commercial CFD package ANSYS Fluent [39] was used. Post-processing of the results was done within MATLAB [40]. The RANS solutions have been validated against the available experimental data and LES results. In particular, the RANS solutions of the transonic SILOET and CoJeN jet cases are compared with with LES experiment. Both of the RANS solutions are then used in the development of subsequent acoustic models which will be discussed in Chapter 4 and 5. The RANS results for the supersonic LTRAC

jet have been compared with the PIV measurements in order to access the robustness of the RANS based solutions for modelling of noise radiated by imperfectly expanded jets [41] which subject is beyond the scope of the current thesis.

2.2 RANS equations

RANS equations are derived from a decomposition of the variables of the governing Navier-Stokes equations into the random fluctuations and the mean values:

$$v_j = \bar{v}_j + v'_j, \quad p = \bar{p} + p'. \tag{2.1}$$

The average values are determined by averaging over a sufficiently large time interval

$$v_j = \lim_{T\to\infty} \frac{1}{T} \int_0^T v_j(t)dt. \tag{2.2}$$

Time averaging of the non-linear convective terms lead to the appearance of so known Reynolds stress term $\rho\overline{v'_i v'_j}$. RANS equations have to be solved with Reynolds stress term by using a set of semi-empirical relations which are known as turbulence models. In order to provide closure to the RANS set of equations, use of an additional model is required to incorporate the effects of turbulence. For example, a wide range of closure models are available in ANSYS Fluent, each specific to different types of fluid flow. The most consistent method of modelling turbulence is through the use of two-equation models that solve transport equations for the turbulent kinetic energy and dissipation rate independently.

2.2.1 $\kappa-\varepsilon$ turbulence model

Two-equation model is implemented in ANSYS package to close RANS equations by solving transport equations for the turbulent kinetic energy κ and eddies dissipation rate ε. The standard $\kappa-\varepsilon$ turbulence model is based on the transport

equations of turbulent kinetic energy κ and its rate of dissipation ε. The transport equation for turbulent kinetic energy κ is derived from the exact equation, whereas the transport equation for the rate of dissipation of turbulent kinetic energy ε is obtained using physical reasoning. The transport equations for turbulent kinetic energy κ and turbulent dissipation ε are:

$$\frac{\partial}{\partial t}(\rho\kappa) + \frac{\partial}{\partial x_i}(\rho\kappa v_i) = \frac{\partial}{\partial x_j}\left[\left(\mu + \frac{\mu_t}{\sigma_\kappa}\right)\frac{\partial \kappa}{\partial x_j}\right] + E_\kappa - \rho\varepsilon, \tag{2.3}$$

$$\frac{\partial}{\partial t}(\rho\varepsilon) + \frac{\partial}{\partial x_i}(\rho v_i\varepsilon) = \frac{\partial}{\partial x_j}\left[\left(\mu + \frac{\mu_t}{\sigma_\varepsilon}\right)\frac{\partial \varepsilon}{\partial x_j}\right] + C_{\varepsilon 1}E_\kappa\frac{\varepsilon}{\kappa} - C_{\varepsilon 2}\rho\frac{\varepsilon^2}{\kappa}. \tag{2.4}$$

Here E_κ represents production of turbulent kinetic energy and defined as

$$E_\kappa = -\rho\overline{v_i' v_j'}\frac{\partial u_j}{\partial x_i}, \quad E_\kappa = \mu_t {S_{ij}}^2. \tag{2.5}$$

In this model the closure is achieved by relating the Reynolds stress to the mean strain rate through Boussinesq approximation

$$-\rho\overline{v_i' v_j'} = \mu_t\left(\frac{\partial v_i}{\partial x_j} + \frac{\partial v_j}{\partial x_i}\right) - \frac{2}{3}\left(\rho k + \mu_t\frac{\partial v_k}{\partial x_k}\right)\delta_{ij}. \tag{2.6}$$

By computing κ and ε one can define the length and time scales as $l = \kappa^{3/2}/\varepsilon$, $\tau = \kappa/\varepsilon$ and turbulent viscosity is defined as $\mu_t = \rho C_\mu \kappa^2/\varepsilon$. Modelling constants are defined as:

$$C_{\varepsilon 1} = 1.44, \quad C_{\varepsilon 2} = 1.92, \quad C_\mu = 0.09, \quad \sigma_\varepsilon = 1.0 \quad \sigma_\kappa = 1.3 \tag{2.7}$$

As discussed by Tam and Ganesan [43], there is no universal turbulence model for jet flow modelling and suggested to modify adjustable constants (2.7) of $\kappa{-}\varepsilon$ model for jet flow modelling. The modified coefficients were obtained by recalibrating $\kappa{-}\varepsilon$ turbulence model using a series of experiments of modelling the jet flow. The closure coefficients for the modified $\kappa{-}\varepsilon$ model are defined as in accordance

with [43]:

$$C_{\varepsilon 1} = 1.40, \quad C_{\varepsilon 2} = 2.02, \quad C_{\mu} = 0.0874, \quad \sigma_{\varepsilon} = 0.377, \quad \sigma_{k} = 0.324. \tag{2.8}$$

2.2.2 SST $\kappa-\omega$ turbulence model

The Shear-Stress Transport (SST) $\kappa-\omega$ turbulence model [44] is a two-equation model which has also become very popular due to its high standard behaviour in adverse pressure gradients and separating flows. The shear stress transport formulation combines the best of two features: (i) the use of $\kappa-\omega$ formulation which provide more accurate solution in the near wall boundary layer and (ii) switches to a $\kappa-\varepsilon$ behaviour in the free-stream and thereby avoids the common $\kappa-\omega$ problems in regions with large normal strains, like stagnation regions. The transport equations for turbulent kinetic energy κ and the specific dissipation rate ω are:

$$\frac{\partial}{\partial t}(\rho k) + \frac{\partial}{\partial x_i}(\rho k v_i) = \frac{\partial}{\partial x_j}\left[\left(\mu + \frac{\mu_t}{\sigma_k}\right)\frac{\partial k}{\partial x_j}\right] + E_k - Y_k, \tag{2.9}$$

$$\frac{\partial}{\partial}(\rho \omega) + \frac{\partial}{\partial x_i}(\rho \omega v_i) = \frac{\partial}{\partial x_j}\left[\left(\mu + \frac{\mu_t}{\sigma_\omega}\right)\frac{\partial \omega}{\partial x_j}\right] + E_\omega - Y_\omega + D_\omega. \tag{2.10}$$

Here σ_k, σ_ω are the turbulent Prandtl numbers for k and ω, E_ω represents the production of specific dissipation rate, Y_κ represents the dissipation of turbulence kinetic energy, Y_ω represents the dissipation of ω. There is an additional so called cross diffusion term D_ω which is introduced as a result of blending $k-\varepsilon$and $\kappa-\omega$ turbulence models. Further complete details on the SST $\kappa-\omega$ turbulence model closure coefficients and auxiliary relations can be found in [44], [45].

2.3 Grid generation

In all RANS calculations, structured grids were used. Because of the axi-symmetric nozzle geometry in all cases, 2D axi-symmteric equations are solved. The grids are

aligned in the flow direction leading to more accurate results and a faster convergence. Multiblock decomposition strategy was used for computational domain decomposition. The idea behind this strategy was to break up the computational domain into several blocks and generate a separate mesh for each. This allows to save mesh generation time significantly. The computational domain is designed to be sufficiently large to ensure that numerical open boundary condition effects are minimal. The grid dimensions for each jet case differs, but not significantly. An important element of numerical modeling by the RANS method is to study sensitivity of the simulation results to the computational grid and to verify the convergence of the solution to the steady state. During this work, RANS calculations were carried out on several initial coarse grids, while at each stage of the grid refinement the number of nodes was consistently increased in the x and y (the stream-wise and radial) grid directions, until the influence of the grid density on the results of calculations of the parameters of interest became insignificant. Adaptive refinement technique is applied to reduce the grid count away from the jet region. The grid refinement was also carried out by iteratively running several RANS calculations to verify that the target y^+ value in the wall-normal units is close to 1 as recommended in RANS simulations.

2.4 Details of the computational solution

The governing RANS equations are solved using the so-called density-based solver in ANSYS Fluent. For spatial discretisation, a second-order Roe scheme is used. With an implicit iterative scheme, the solution is converged within 10^{-5} of initial value. Boundary conditions have been defined at nozzle inlet, free inlet, in the far-field region and at the downstream region in accordance with the jet operating conditions which are discussed in the next sections.

2.5 SILOET jet

Single stream convergent nozzle geometry is considered first. Its initial CAD geometry is presented in Figure (2.1). Two operating conditions which correspond to heated and unheated jet cases are presented in the Table (2.1)

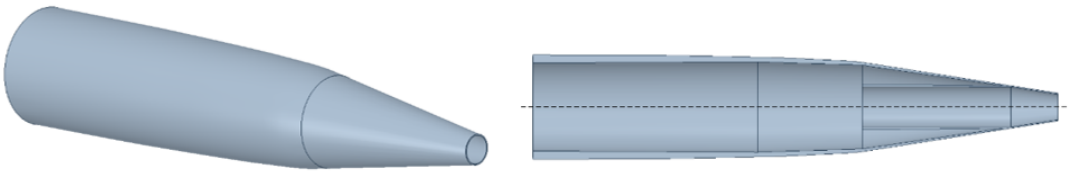

(a) (b)

Figure 2.1: SILOET jet CAD model

	D_j	U_j	M_j	T_j/T_0	Re
Cold jet	0.1016m	297	0.875	1	$2 \cdot 10^6$
Hot jet	0.1016m	297	0.55	2.5	$4 \cdot 10^6$

Table 2.1: The operating conditions: SILOET jet.

The RANS domain is designed to be sufficiently large to ensure that numerical open boundary condition effects are minimal. Computational domain is extended in x direction and in y direction. The total number of elements is approximately $120 \cdot 10^3$ elements and computational grid is presented in the Figure (2.2).

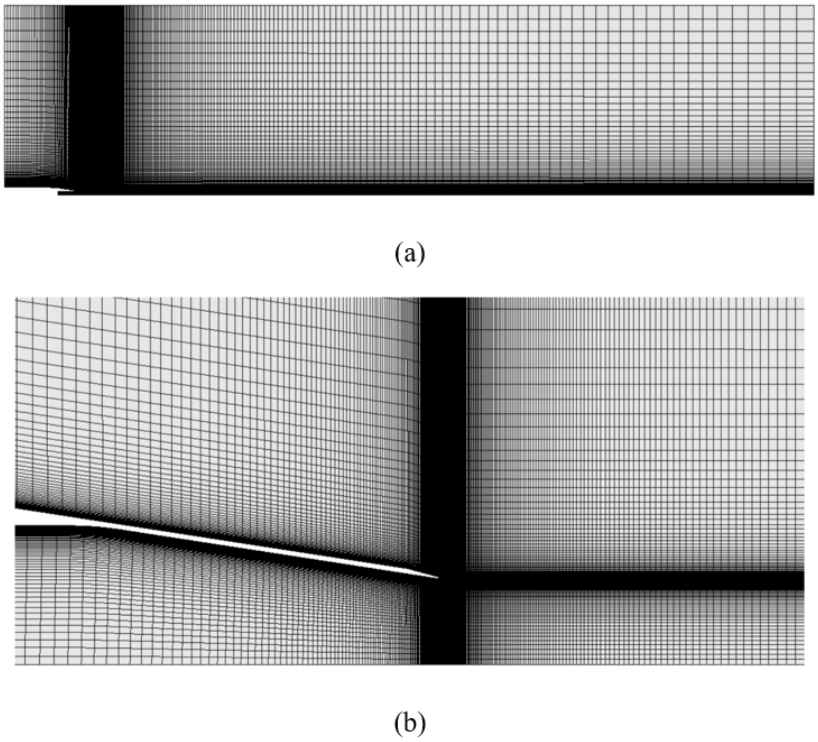

Figure 2.2: SILOET jet RANS mesh: the full domain (a) and a close-up view near the nozzle (b)

Since no experimental flow data were available for the SILOET jet flows, hence, in the following figures the RANS solution will be compared with the Wall-Modeled Large Eddy Simulation (WMLES) from [46]. In each jet case, the normalization is based on jet velocity at the core nozzle exit and the same quantity squared for the meanflow velocity and the turbulent kinetic energy plots, respectively. It can be noted that the RANS fields match the LES solutions reasonably well not only for the meanflow velocity but also for the turbulent fluctuations as shown in Figure (2.3).

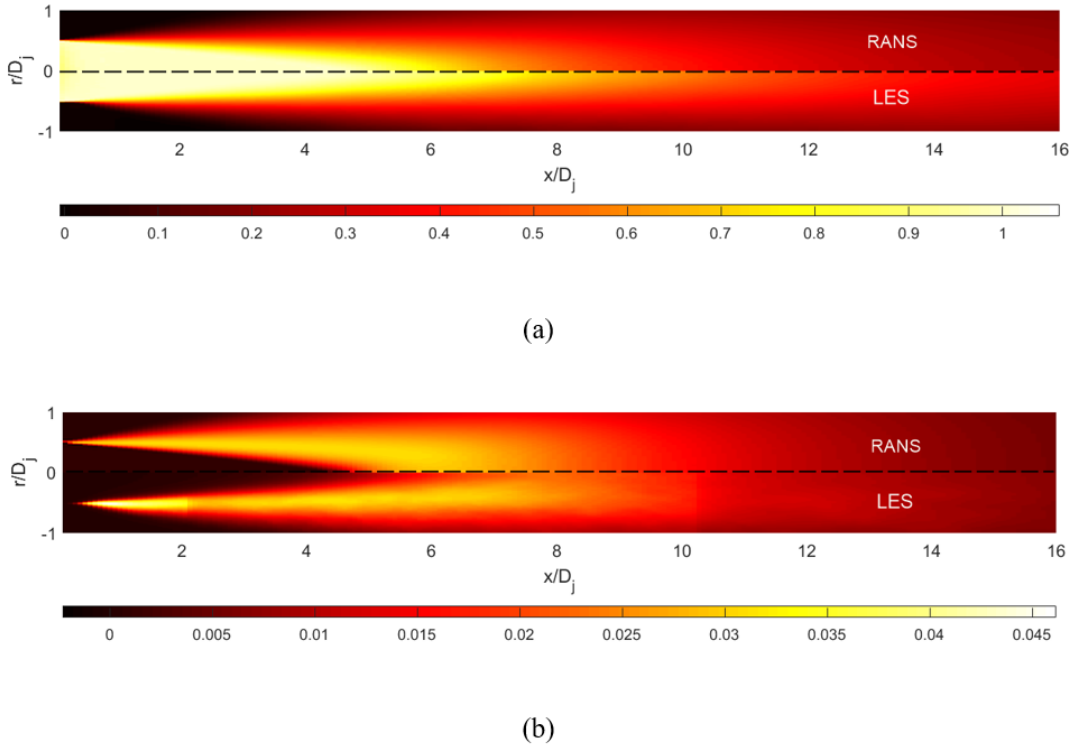

Figure 2.3: Comparison of the RANS solutions with the reference LES flow fields: contours of the mean axial velocity component (a) and turbulent kinetic energy (b) for the heated SILOET jet.

For RANS calculation of SILOET jets, a special set of the turbulence model parameters (2.8) is used as recommended by Tam and Ganesan [43] and compared with the standard $\kappa-\varepsilon$ turbulence model. Indeed, as discussed by Tam and Ganesan the modified $\kappa-\varepsilon$ turbulence model is capturing the length of the potential core for single stream jets correctly. While the decay of jet spreading predicted by RANS is still faster in comparison with the LES solution as shown in Figure (2.4).

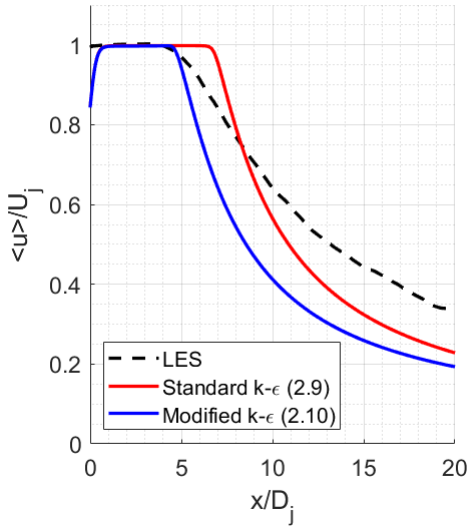

Figure 2.4: Cold SILOET jet comparison of LES centerline velocity profile with standard $\kappa-\varepsilon$ model and modified $\kappa-\varepsilon$ turbulence model.

2.6 CoJeN jet

The CoJeN experiment was designed to represent the jet flow conditions at the take-off. The period of take-off can be considered at the period of the greatest noise production of the jet. The selected Operation Points (OP) of the CoJeN family corresponds to a well-defined dataset including the short-cowl axi-symmetric nozzle geometry, the flow data downstream of the central body, and the far-field noise measurements. The experiments were conducted in the QinetiQ Noise Test Facility (NTF). The inner stream of the considered co-axial jet flow is heated and issues from the core nozzle at supersonic acoustic Mach number while the outer stream is cold and has a subsonic flow velocity. The combination of dual-stream jet parameters leads to transonic flow regions emerging in the jet core/bypass stream shear layers, which makes this benchmark case challenging for modeling.

Dual stream nozzle geometry with a central body is considered for RANS modelling with $\kappa-\omega$ SST turbulence model. Its CAD geometry is presented in

the Figure (2.5). Operating conditions span across a representative range of Mach numbers and core/bypass temperatures and presented in Table (2.2). This case was previously investigated using Particle Image Velocimetry (PIV) [47] the near-field acoustic array technique [48] , and a combination of PIV and Laser Doppler Anemometry (LDA) [49]. The far-field measurements performed by QinetiQ for 6 co-axial jet flows (Table 2.2). For reference, the size of the bypass nozzle diameter, D_j is 0.273m.

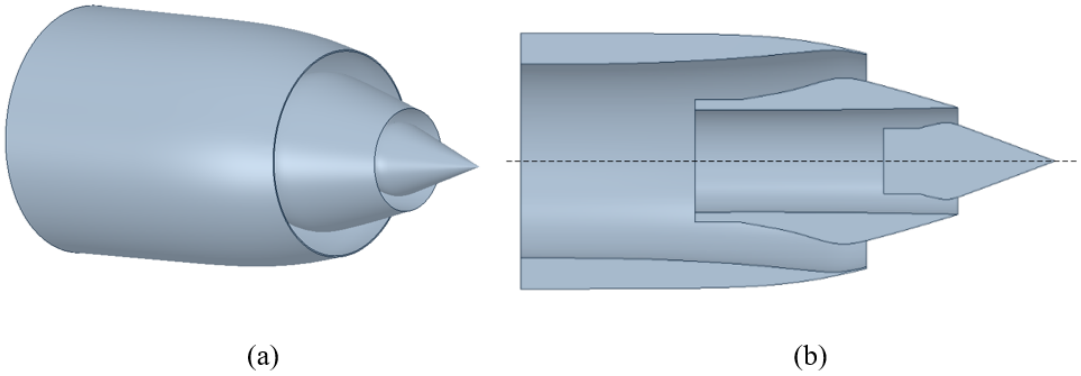

Figure 2.5: CoJeN nozzle CAD (a), (b).

Operation Point		**1.1**	**1.2**	**1.3**	**1.4**	**1.7**	**1.8**
Core	U_j	340.3	404.5	480.7	341.5	218.4	241.7
	M_j	0.621	0.738	0.877	0.620	0.642	0.712
	T_{sj} (K)		775.6		785.0	287.8	287.0
	T_{tj} (K)	827.9	849.5	879.9	837.2	311.5	316.0
Bypass	U_b (m/s)		306.8		218.0	218.1	217.4
	M_b		0.902		0.637	0.640	0.634
	T_{sb} K		288.14		291.14	289.0	292.2
	T_{tb} K		335.0		289.6	312.7	315.7

Table 2.2: The operating conditions: CoJeN jet

The grid dimensions in the axial and the radial directions are $50D_j$ and $30D_j$, respectively. Computational domain is shown in Figure (2.6) It total, the RANS grid contains $250 \cdot 10^3$ elements. A body-fitted curvilinear grid is generated where adaptive refinement is applied to reduce the grid count away from the jet region, thus, reducing the computational cost while maintaining the accuracy of the results.

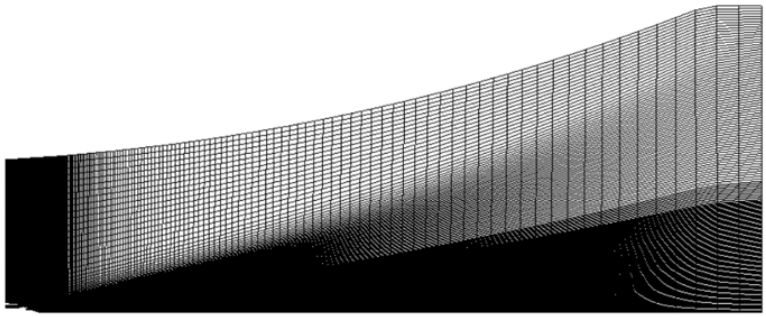

(a)

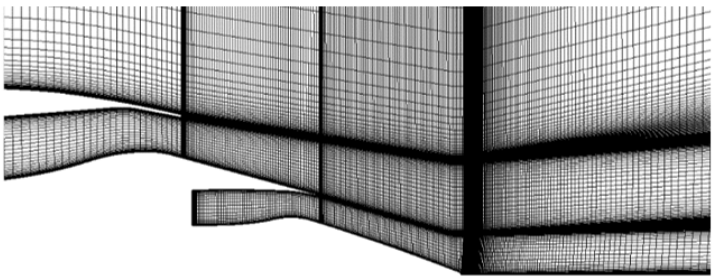

(b)

Figure 2.6: RANS mesh: the full domain (a) and a close-up view near the nozzle

For validation of the RANS solutions, in addition to the experimental data, WMLES solution [50] and the method based on the hybrid RANS/ Implicit LES [51] will be used for comparison of the CoJeN flow field results. For comparison two operating points were considered which correspond to OP1.3 jet case which is the heated and fastest core jet and OP1.7 which can be considered as a cold single stream like jet. Figures (2.7) and (2.8) compares the symmetry-plane distributions

of the axial component of the meanflow velocity and turbulent kinetic energy of the RANS solution with the LES fields for the OP1.3 and the OP1.7 CoJeN jets. Both cases RANS and LES solution can be considered to have a good agreement.

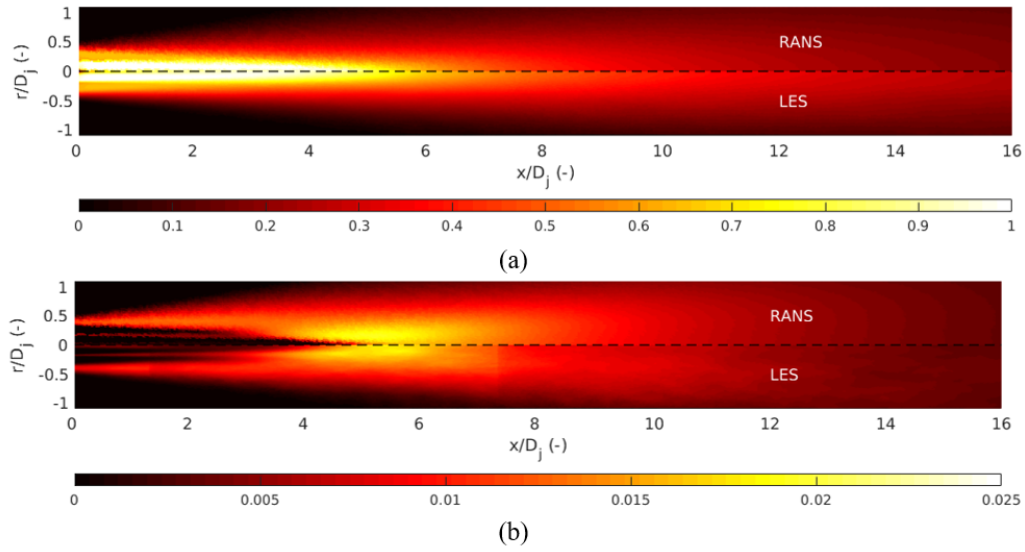

Figure 2.7: Comparison of the RANS solutions with the reference LES flow fields: contours of the mean axial velocity component (a) and turbulent kinetic energy (b) for the OP1.3 jet.

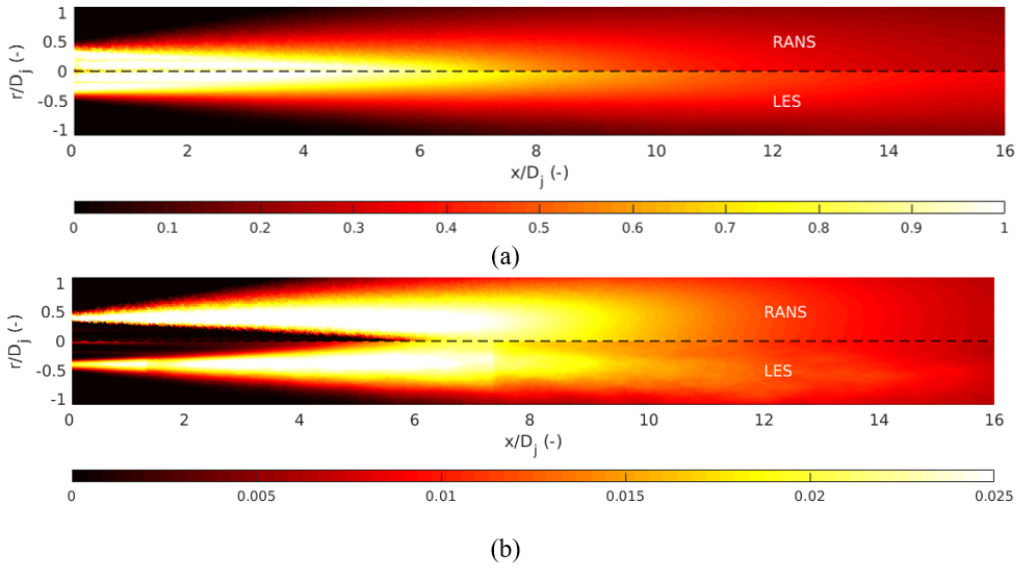

Figure 2.8: Comparison of the RANS solutions with the reference LES flow fields: contours of the mean axial velocity component (a) and turbulent kinetic energy (b) for the OP1.7 jet.

Figure (2.9) shows comparison of the centerline profiles of the meanflow velocity and the stream-wise velocity fluctuations for the RANS solution and the LES solutions from [51] with the experiment for the OP1.3 jet. One LES solution is based on the Wall Modelled LES and the other is based on the hybrid RANS/ILES approach of IDDES-type. The experimental dataset is obtained by digitizing the data from [8]. The RANS solution for the velocity fluctuation is computed following a common assumption between the turbulent velocity fluctuation in the stream-wise direction $\langle u_1{}' \rangle$ and in the directions normal to the high-speed axisymmetric jet flow $\langle u_1{}' \rangle = 1.5 \langle u_2{}' \rangle = 1.5 \langle u_3{}' \rangle$, (where 1 is in the jet flow direction and 2 and 3 are in the transverse plane normal to the jet), which allows to extract the stream-wise velocity fluctuation from the turbulent kinetic energy component of the RANS solution.

It can be noted that the RANS solution is in a reasonable agreement with the LES and the experiment for the OP1.3 jet case near the end of the potential

core but overpredicts the spreading rate of the jet. The RANS solution for the velocity fluctuation underpredicts the turbulence in the wake region but remains in a reasonable agreement with the LES in the vicinity of the peak of turbulent velocity fluctuation and also at locations further downstream in the jet.

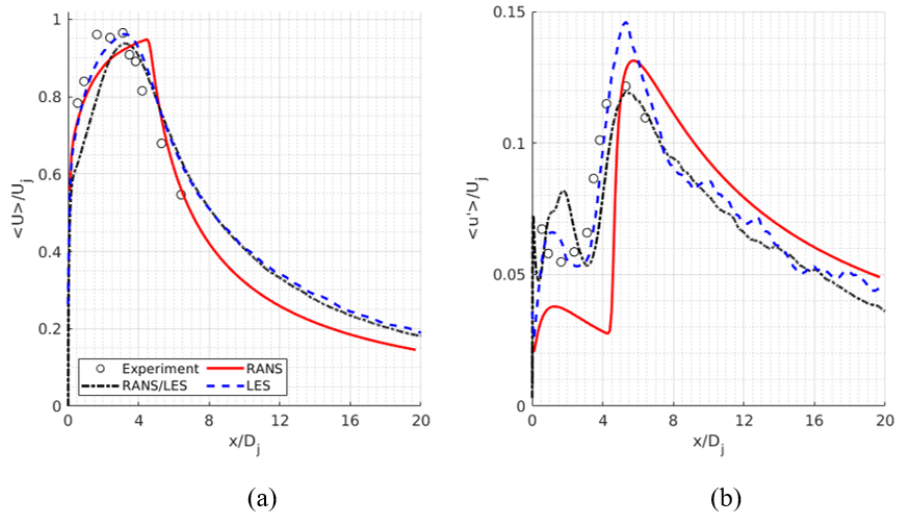

Figure 2.9: Comparison of the GPU-CABARET, RANS/ILES and RANS: mean axial velocity (a) and mean axial velocity fluctuations (b) along the centerline normalized by the jet core velocity of OP1.3 jet.

Figure (2.10) shows radial profiles of the axial meanflow velocity component (Figure 2.9a) and the mean turbulent kinetic energy (Figure 2.9b) for several axial locations downstream of the central body. The WMLES, the RANS/ILES, and the RANS solutions are compared with the experimental data. For the meanflow velocity profiles, all three solutions are in good agreement with the experiment. The solutions of the LES methods for the turbulent kinetic energy also show a very good agreement with the experiment for jet locations upto $x/D_j \approx 5$ and overpredict the levels of turbulence in the jet core locations further downstream. In comparison with the LES, the RANS solution for turbulent kinetic energy generally overpredicts turbulence in the bypass stream and underpredicts it in the core stream.

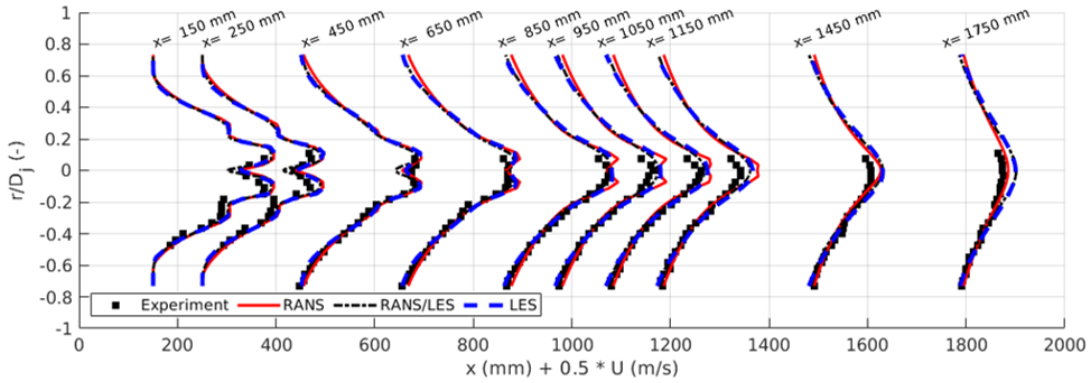

(a)

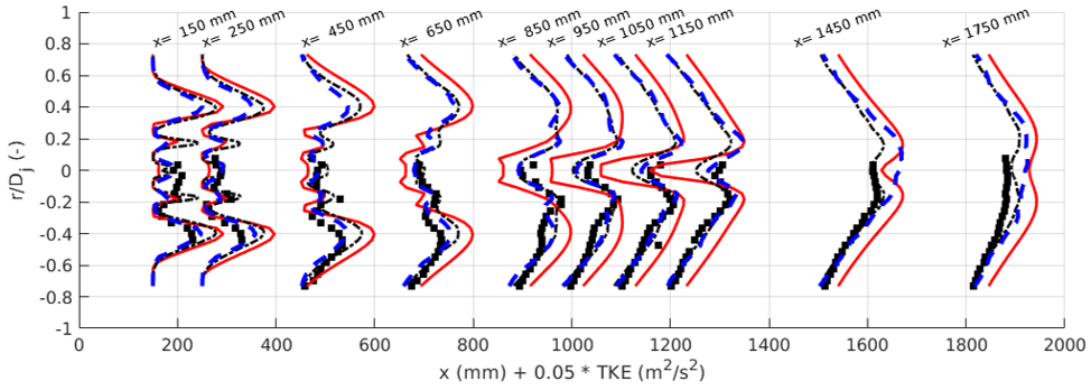

(b)

Figure 2.10: Comparison of the GPU-CABARET, RANS/ILES and RANS: radial profiles of the mean axial velocity (a) and the turbulent kinetic energy (b) of OP1.3 jet.

2.7 LTRAC jets

A convergent nozzle with a high aspect ratio is considered next. CAD geometry is presented in the Figure (2.11). The jet experiment was conducted in LTRAC Supersonic Jet Facility at Monash University where PIV measurements were also performed. In comparison with SILOET and CoJeN jets, LTRAC jets case is strongly under expanded. For the LTRAC case, the $\kappa-\omega$ SST turbulence model is

used, which accounts for the adverse pressure gradients that are characteristic of supersonic flows. Results of the RANS modelling are compared with the PIV data from the same experiment. A summary of the operating parameters of LTRAC jets is provided in Table 2.3. The computational domain was designed to ensure that boundary effects do not contaminate the solutions with axial x and transverse y dimensions of $60D_j$ and $20D_j$, respectively, and the domain is shown in Figure (2.12). The computational mesh has $165 \cdot 10^3$ elements that were created using an adaptive refinement technique. The mesh refinement near the nozzle exit and in the shear layer is evident in the half-view of the computational domain. The mesh was determined by identifying and subsequently refining important flow regions, such as zones around the shear layers and the shock cells.

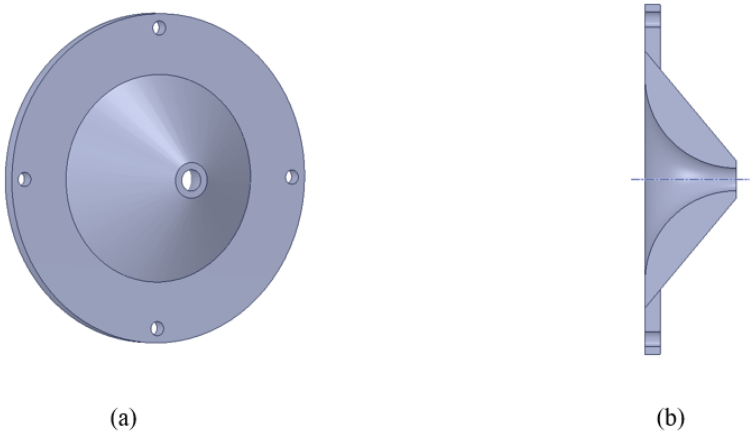

Figure 2.11: CAD Model LTRAC nozzle.

M_j	NPR	TTR	Re	D_j
1.45	3.4	1	$7 \cdot 10^5$	0.015m
1.59	4.2	1	$8 \cdot 10^5$	0.015m

Table 2.3: The operating conditions: LTRAC jet

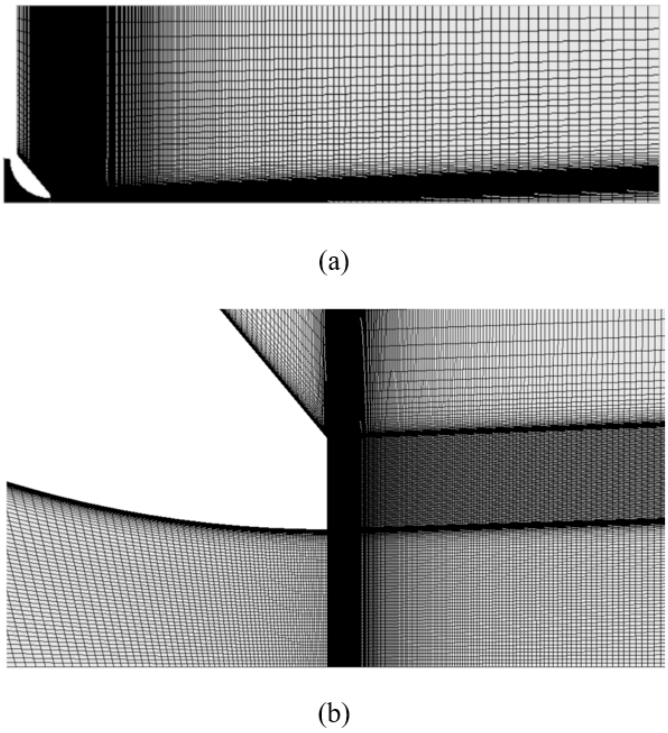

Figure 2.12: LTRAC jet RANS mesh: the full domain (a) and a close-up view near the nozzle (b).

The mean axial and transverse velocity fields that are obtained from the RANS solutions are compared with the PIV measurements in Figures (2.13) and (2.14). The PIV and RANS fields are presented as the top and bottom halves of each contour map, respectively. The sonic line and axial locations of the shock reflection points superimposed with the outer edge of the shear layer indicated on the axial velocity contours of the PIV measurements. The supersonic region is delineated by the sonic line, which is indicated by the dashed horizontal lines. The global flow structure is well predicted by the RANS at both Mach numbers. There are some discrepancies in the shock-cell spacing predicted from the RANS solutions for $M_j = 1.59$ and $x/D_j > 5$. A second internal shear layer occurs for $M_j = 1.59$ due to a Mach disk that is well resolved in both the experiments and simulations. However, despite these differences, there is generally a good agreement between

the PIV measurements and RANS simulation.

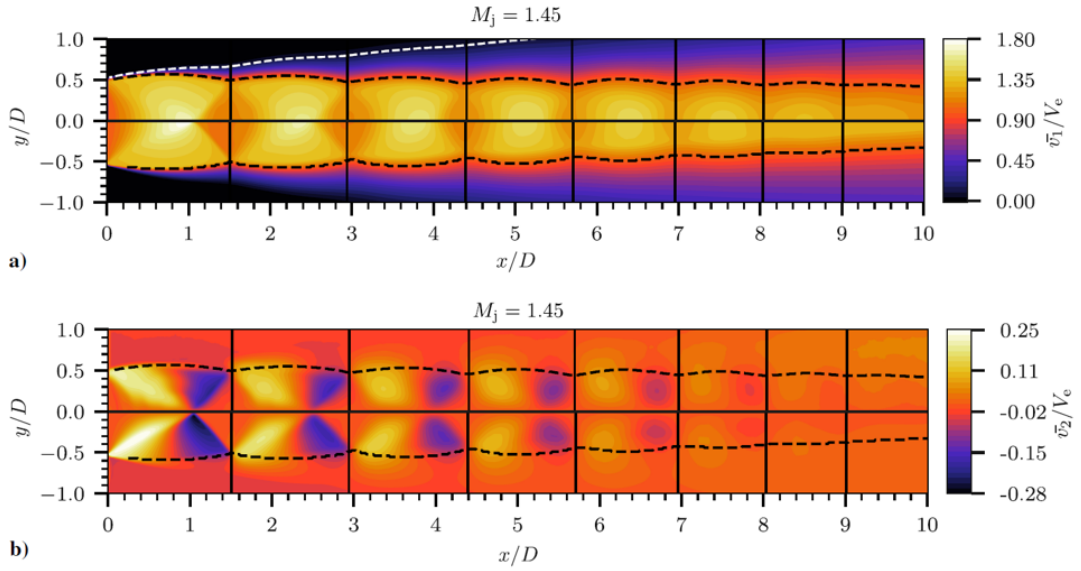

Figure 2.13: Half plane mean axial and transverse velocity fields for LTRAC jet $M_j = 1.45$(top - PIV; bottom - RANS) (Tan et al 2019)

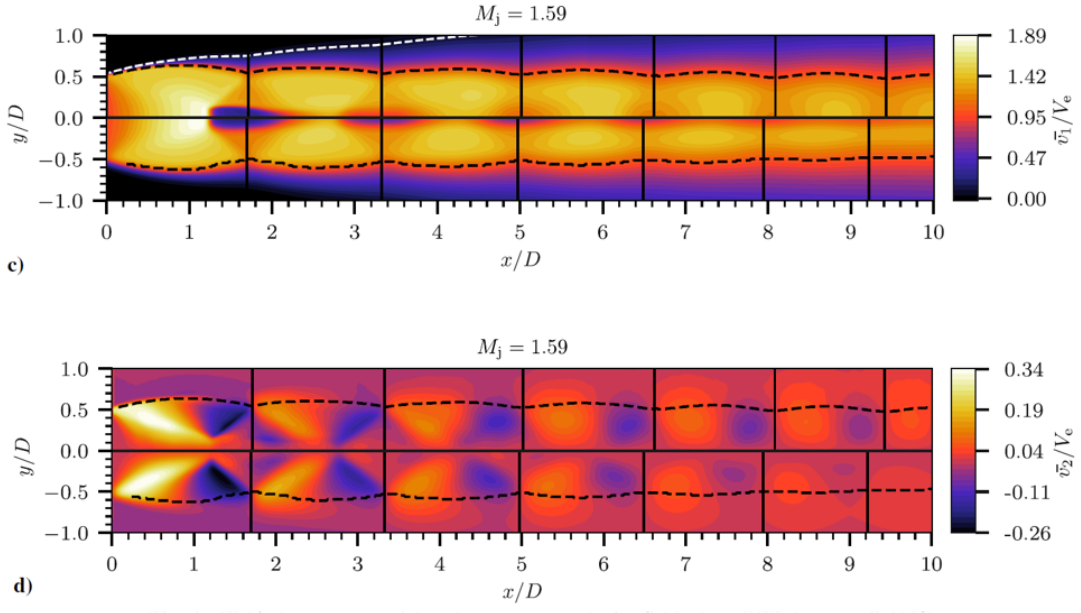

Figure 2.14: Half plane mean axial and transverse velocity fields for LTRAC jet $M_j = 1.59$ (top - PIV; bottom - RANS) [42]

Summary

RANS solutions for three different nozzle geometries are considered. The considered jet cases include single-stream jets corresponding to the SILOET experiment, dual-stream jets with a central body corresponding to the CoJeN experiment and supersonic under-expanded LTRAC jets. Most of the considered jet cases are heated.

Starting from CAD geometry, computational grid generation and the choice of appropriate solver settings, RANS modelling for all considered jet cases have been performed. For validation, comparison with LES and available experimental results is considered. In most cases, the RANS solutions are in a good agreement with the reference solutions, which makes these solutions suitable for a further use in the low-order acoustic modelling.

Chapter 3

Temperature gradient effects on noise propagation in the jet

3.1 Sound propagation in heated jets

It is well-known that jet temperature has an important effect on mixing noise in hot jets [12], [29], [30], [53]. First of all, heat modifies jet turbulence by affecting the turbulent fluctuating Reynolds stresses and producing additional noise sources associated with the fluctuating temperature and entropy. These additional sources can be associated with the entropy noise source of the original Lighthill acoustic analogy formulation [9] as well as in the Lilley acoustic analogy [11]. In accordance with the Goldstein generalised acoustic analogy [17],[28], the temperature effect on hot jet noise is described by the fluctuating enthalpy term. In comparison with other acoustic analogy formulations, the generalised acoustic analogy most consistently eliminates the jet meanflow effects from the effective noise sources. In cold jets, this includes sound refraction through a non-uniform meanflow. In hot jets, the same formulation also takes into account bending of sound waves when they pass through hot temperature spots in the jet where the local sound speed

changes rapidly. In the generalised acoustic analogy literature, several investigations already discussed the sound meanflow propagation effects in cold jets [54], [55], [56] including asymmetric and multistream jets [57], [58]. A relatively few publications have a specific focus on sound propagation of elementary sources in a spreading cold jet flow [5], [59]. In comparison with the cold jets, the number of publications devoted to hot jet noise is much less. This is despite the importance of hot jet noise for aerospace applications, due to the fact that the air flow at the nozzle exhausts of propulsion jet engines is almost always hot. Furthermore, to the best knowledge of the author, there is no single publication in the vast jet noise literature which would systematically study the jet temperature effect on noise propagation while isolating other effects such as the turbulence modelling. The effect of temperature gradient on far-field noise propagation by considering a representative set of jet meanflow and source directivity conditions have been studied by Gryazev [60]. The present analysis is anchored at the conditions of the heated SILOET jet experiment which has been discussed in Chapter 2. Meanflow parameters are obtained from validated LES simulation and the resulting problem of sound propagation through a hot jet flow is considered with and without taking into account the jet temperature gradient.

3.2 Analytical source model

In order to investigate the effect of the non-uniform temperature distribution effects on noise propagation in a hot jet flow, analytical source model will be constructed following [61] and [60].

Effective sources of non-isothermal jet are represented via fluctuating Reynolds stress which has quadrupole form and fluctuating enthalpy terms which is dipole. The correlation between the momentum and the fluctuating enthalpy

stress is neglected and the acoustic integral (1.36) is rewritten as

$$\hat{P}(\mathbf{x},\omega) = P_A + P_B, \tag{3.1}$$

$$\hat{P}_A(\mathbf{x},\omega) = \int_V \int_V \hat{R}_{ijkl}(\mathbf{y},\boldsymbol{\Delta},\omega)\hat{I}_{ij}(\mathbf{y},\omega;\mathbf{x})\hat{I}^*_{kl}(\mathbf{y}+\boldsymbol{\Delta},\omega;\mathbf{x})d\boldsymbol{\Delta}d\mathbf{y}, \tag{3.2}$$

$$\hat{P}_B(\mathbf{x},\omega) = \int_V \int_V \hat{R}_{i4j4}(\mathbf{y},\boldsymbol{\Delta},\omega)\hat{I}_{i4}(\mathbf{y},\omega;\mathbf{x})\hat{I}^*_{k4}(\mathbf{y}+\boldsymbol{\Delta},\omega;\mathbf{x})d\boldsymbol{\Delta}d\mathbf{y}, \tag{3.3}$$

where the Fourier-domain source terms are the corresponding transforms of the time-domain auto-covariances of turbulent fluctuating Reynolds stress and the fluctuating enthalpy stresses,

$$R_{ijkl}(\mathbf{y},\boldsymbol{\Delta},\tau) = \overline{T'_{ij}(\mathbf{y},t)T'_{kl}(\mathbf{y}+\Delta,t+\tau)}, \quad T'_{ij} = \left(\rho v'_i v'_j - \bar{\rho}\widetilde{v'_j v'_j}\right), \tag{3.4}$$

and

$$R_{i4j4}(\mathbf{y},\boldsymbol{\Delta},\tau) = \overline{H'_i(\mathbf{y},t)H'_j(\mathbf{y}+\Delta,t+\tau)},, \quad H'_{j'} = \left(\rho v'_j h'_0 - \bar{\rho}\widetilde{v'_j h'_0}\right), \tag{3.5}$$

respectively.

An analytical ring model of uncorrelated quadrupole $\hat{R}_{ijkl}$ and the dipole $\hat{R}_{i4j4}$ sources is considered following [61] and [60]. The resulting directivity of the ring source satisfies the correlation functions (3.4), (3.5) and it is defined as

$$\hat{R}_{ijkl}(\mathbf{y},\boldsymbol{\Delta},\omega) = \alpha_{ijkl}\delta(x-x_s)r^{-1}\delta(r-r_s)\delta(\boldsymbol{\Delta}), \tag{3.6}$$

and, similarly

$$\hat{R}_{i4j4}(\mathbf{y},\boldsymbol{\Delta},\omega) = \beta_{ij}\delta(x-x_s)r^{-1}\delta(r-r_s)\delta(\boldsymbol{\Delta}), \tag{3.7}$$

Here x_s , r_s are the axial and radial coordinates of the sources. α_{ijkl} and β_{ij} are the corresponding quadrupole and dipole source strengths. The source strengths

depend on the component $i, j = 1, 2, 3$ (1 is in the jet flow direction, 2 is in the radial direction, and 3 is in the circumferential direction) and vary along the jet lipline location $\mathbf{y} = (x, D/2, 0)$ as one of the dominant location for jet noise fig.3.1. Thus, in the case of the ring of quadrupole sources, the acoustic integral (3.4) reduces to

$$\hat{P}_A = \alpha_{ijkl} \int_0^{2\pi} \hat{I}_{ij}(x_s, r_s, \theta) \hat{I}^*_{kl}(x_s, r_s, \theta) d\theta. \tag{3.8}$$

In the case of the ring of dipole sources, the acoustic integral(3.5) becomes

$$\hat{P}_B = \beta_{ij} \int_0^{2\pi} \hat{I}_{i4}(x_s, r_s, \theta) \hat{I}^*_{i4}(x_s, r_s, \theta) d\theta. \tag{3.9}$$

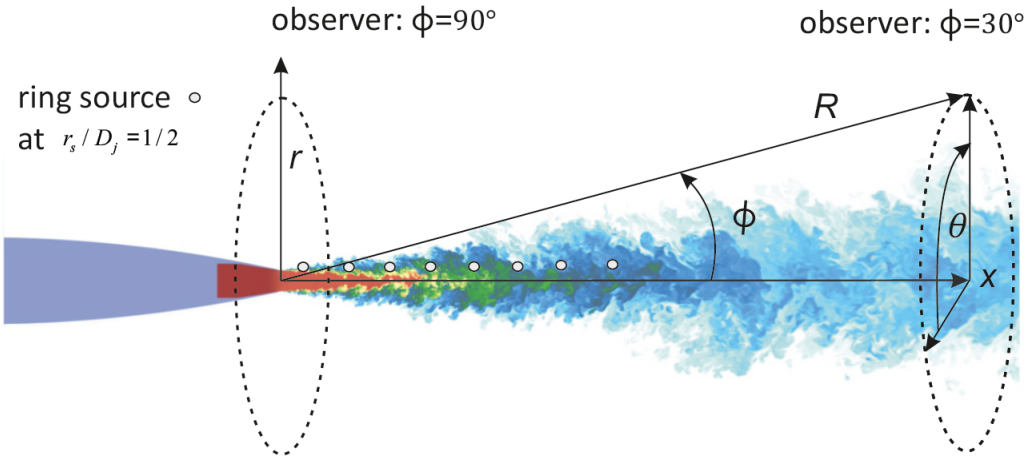

Figure 3.1: The flood field shown corresponds to an instantaneous snapshot of the temperature distribution in the jet symmetry plane from LES. Open circles show locations of the elementary ring sources along the jet lipline.

The extraction procedure of quadrupole and dipole source strengths for acoustic modelling from LES solution as well as its validation will be discussed in the

next section.

3.3 Validation of the LES solution and computation of the acoustic model parameters

LES solution of heated single stream jet is considered and will be briefly presented. Numerical method is based on the Compact Accurately Boundary-Adjusting high-REsolution Technique (CABARET scheme) [62], which implementation for single-stream SILOET jet flow in the framework of Monotonically Integrated LES (MILES) can be found in the series of works Markesteijn et al. [6], [46], [63], [64]. In the current LES calculation, the stream-wise extend of the computational domain is about $100D_j$ and the radial size is $30D_j$. The total LES grid count is about $86 \cdot 10^6$ control volumes. No information about the boundary layer state upstream of the nozzle exit is available in the SILOET experiment. Hence, for simplicity, the present LES calculation did not attempt any modelling of the turbulent inflow condition assuming an initially laminar jet condition at the nozzle exit. To evaluate the effect of the latter approximation on the far-field noise spectra of a consensus turbulent jet flow based on the acoustic Mach number and temperature ratio parameters of the SILOET jet, the current noise spectra predictions based on the LES are also compared with the predictions of the empirical sJet model developed by NASA and calibrated on a large database of singe-stream jet cases of various Mach numbers and temperature ratios. For the LES validation in comparison with the experimental data which are only available in the acoustic far field, the standard penetrable-surface formulation of the Ffowcs Williams – Hawkings method [16] is applied to extrapolate the LES flow solution to far-field microphone locations. Figure (3.2)a shows a picture of the FW-H surface including the closing disc region that is superimposed on a snapshot of the axial velocity component of

the jet in the nozzle symmetry plane and a snapshot of the instantaneous pressure fluctuations outside the jet flow. Further details of acoustic waves radiated by the jet are illustrated in Figure (3.2)b. Here the low-frequency waves appear to radiate from the end of potential core region of the jet at a small angle to the jet while the high frequency waves tend to radiate from the initial shear layers more-or-less uniformly at all angles. All of these are in accordance with the well-known behaviour of jet mixing noise [52]. An estimate of the typical Strouhal number (St_D, based on the nozzle diameter and jet velocity at the nozzle exit) shows the high-frequency and the low-frequency waves approximately correspond to $St_D = 2{-}3$ and $St_D = 0.2{-}0.3$, respectively. The later frequency range corresponds to the peak far-field noise spectra as shown in Figure (3.3) which compares the LES noise spectra predictions with the microphone measurements at the distance of $120D_j$ from the nozzle exit.

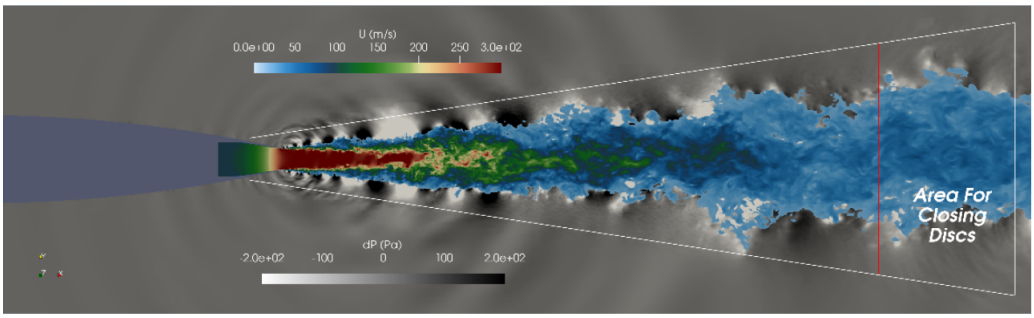

(a)

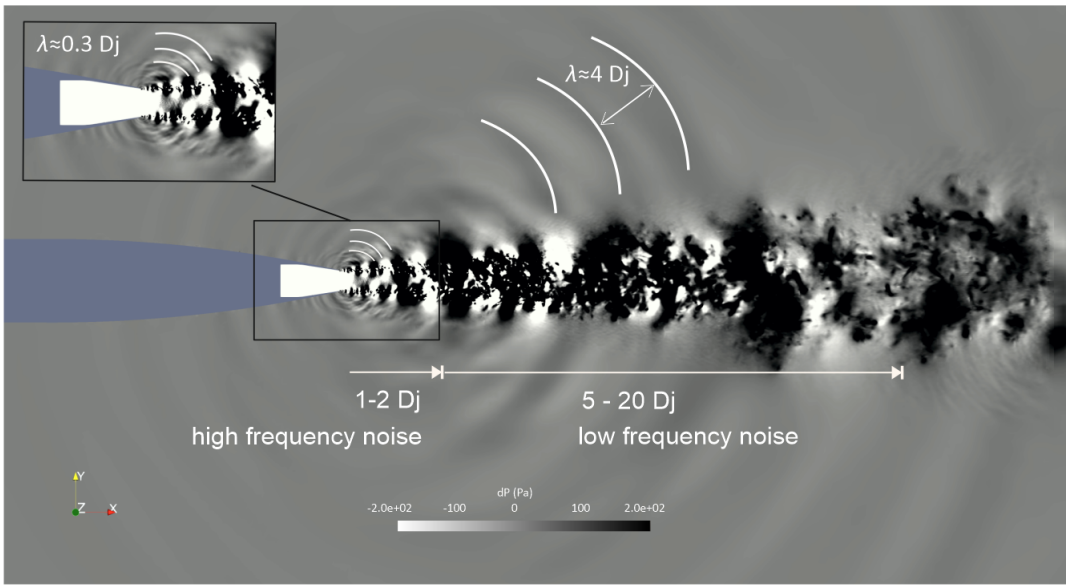

(b)

Figure 3.2: The LES flow and acoustic pressure solution around the jet: instantaneous axial velocity component and pressure distributions with a superimposed schematic of the acoustic integration surface of the FW-H method (a) and the acoustic pressure distribution including a close-up view of the initial jet region (b). Acoustic wave fronts are highlighted to facilitate the estimation of characteristic noise frequencies in each case.

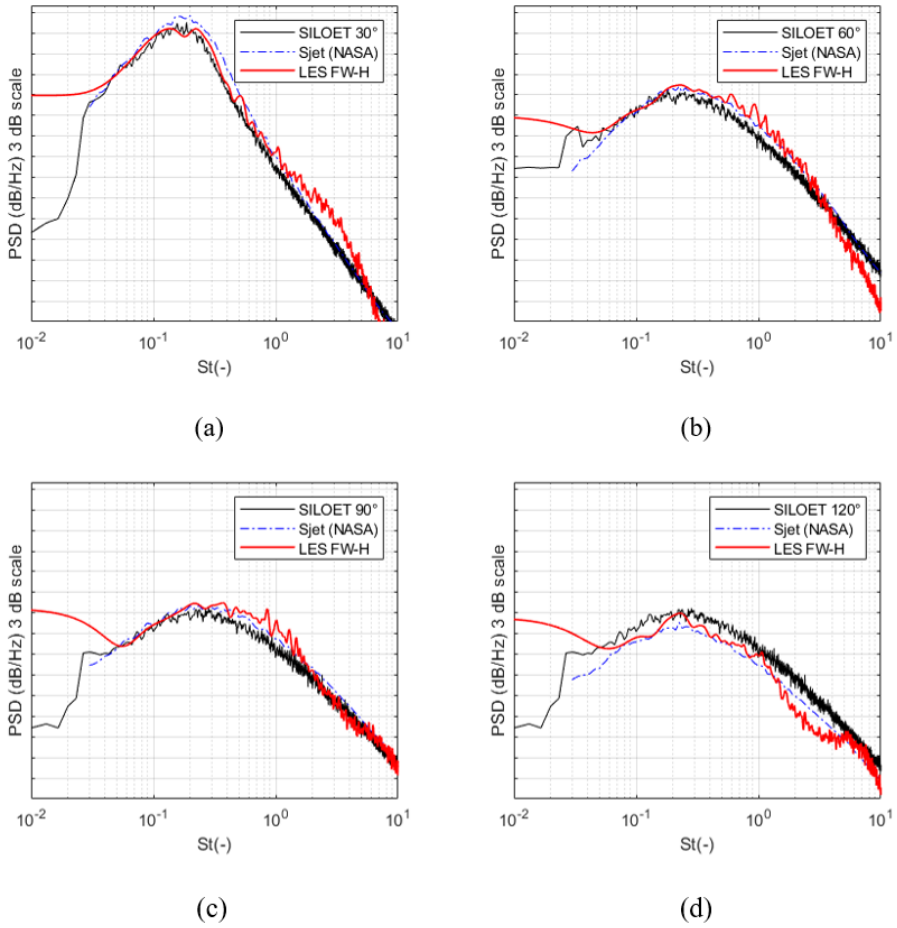

Figure 3.3: LES-based noise spectra predictions for the hot SILOET jet experiment: comparison with the experiment and predictions of the empirical sJet model at 30° (a), 60° (b), 90° (c), and 120° (d) polar angles to the jet flow.

The LES predictions are within 2-3dB from the experiment for frequencies $0.04 < St_D < 8$ for polar angles $30 - 90°$ and $0.04 < St_D < 1.5$ for the 120° angle. The agreement between the current LES predictions and the empirical sJet model is also encouraging especially for the forward noise propagation angle where the two solutions agree within 2-3dB over the entire frequency range of $0.04 < St_D < 8$. Overall, despite some overprediction of jet noise at high frequencies which are most likely being associated with the laminar inflow jet condition, the current LES solution can be considered as a reasonably accurate representation of a high-speed

turbulent jet flow for the acoustic modelling in this Chapter. Relevant meanflow and higher-order statistical properties are interpolated on a uniform Cartesian grid. These interpolated quantities define both the parameters of sound meanflow propagation and the amplitudes of elementary noise sources in accordance with the generalised acoustic analogy. In order to calculate the source strengths α_{ijkl} and β_{ij} in equation (3.8), (3.9) along the jet lipline location $\mathbf{y} = (x, D/2, 0)$, the following procedure is used:

1. Obtain time-dependent velocity components v_i, density ρ, and pressure p from LES,
2. Calculate Favre-averaged velocity fluctuations, $\tilde{v}_i = \overline{\rho v_i}/\overline{\rho}$ and $v_i' = v_i - \tilde{v}_i$,
3. Calculate the fluctuating Reynolds stress tensor $T_{ij}' = \left(\rho v_i' v_j' - \widetilde{\bar{\rho} v_i' v_j'}\right)$,
4. Calculate the non-normalised source strengths $\alpha_{ijkl} = \overline{T_{ij}' T_{kl}'}$ and the normalization constant $C^{-1} = \max \alpha_{ijkl}$,
5. All source strengths are non-dimensionalised by the peak value of the largest correlation components in each case and only several major components have been considered following [61]. Similarly, dipole source strengths β_{ij} (3.9) can be obtained.

The corresponding lipline distributions obtained from LES of the heated SILOET jet are shown in Figure 3.4 and dimensionless source strengths are summarised in Tables 3.1, 3.2.

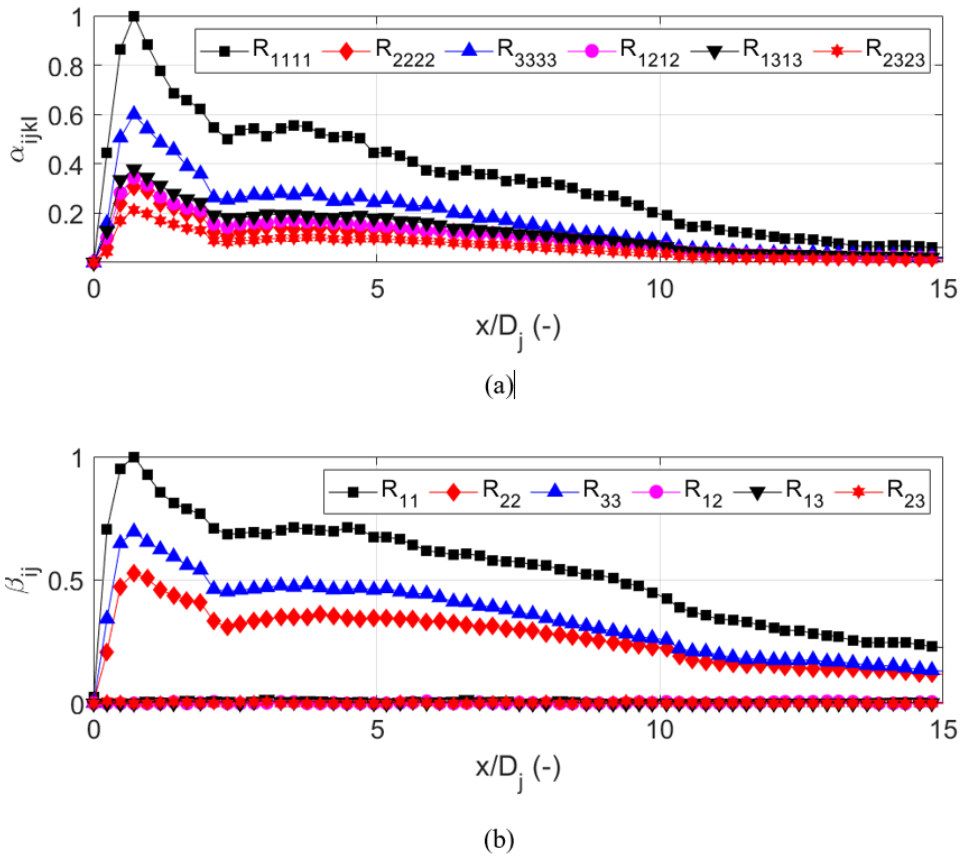

Figure 3.4: Strength distributions of the major source components along the jet lipline of the hot SILOET jet as a function of distance from the nozzle exit for quadrupole (a) and dipole sources (b).

α_{ijkl}	x/D_j									
	1	2	3	4	5	6	7	8	9	10
1111	1	0.75	0.61	0.61	0.53	0.50	0.45	0.38	0.26	0.21
2222	0.38	0.24	0.16	0.18	0.16	0.15	0.13	0.10	0.08	0.06
3333	0.79	0.47	0.35	0.32	0.31	0.27	0.21	0.16	0.13	0.08
1212 1221 2112 2121	0.38	0.26	0.18	0.20	0.17	0.16	0.14	0.11	0.08	0.06
1313 1331 3113 3131	0.44	0.30	0.24	0.23	0.21	0.19	0.15	0.12	0.09	0.06
2323 3223 2332 3232	0.27	0.17	0.12	0.12	0.12	0.10	0.08	0.06	0.05	0.03

Table 3.1: Dimensionless amplitudes of the elementary quadrupole sources.

β_{ij}	x/D_j									
	1	2	3	4	5	6	7	8	9	10
1111	1	0.80	0.72	0.72	0.68	0.66	0.62	0.56	0.48	0.42
2222	0.59	0.44	0.36	0.38	0.37	0.35	0.32	0.28	0.25	0.21
3333	0.76	0.59	0.51	0.50	0.48	0.45	0.40	0.35	0.31	0.25
12 21	0	0	0	0	0	0	0	0.01	0.01	0
13 31	0	0	0.01	0	0.02	0	0	0.01	0.01	0
23 32	0	0	0.01	0	0	0	0	0.01	0	0

Table 3.2: Dimensionless amplitudes of the elementary dipole sources.

3.4 Propagator

For typical noise source locations in the jet shear layers, noise frequencies, and far-field observer angles, the far-field noise propagation problem is solved with a semi-analytical vector adjoint Green's function technique. The propagator tensor in (3.8) following the results of the derivation from Chapter 1 is given as:

$$\hat{I}_{ij} = \sum_{n=0}^{\infty} \hat{I}_{ij}^{(n)}. \tag{3.10}$$

Here

$$\hat{\mathbf{I}}_{ij}^{(n)} = \begin{pmatrix} a_{11}^{(n)} \cos n\theta & a_{12}^{(n)} \cos n\theta & b_{13}^{(n)} \sin n\theta \\ a_{21}^{(n)} \cos n\theta & a_{22}^{(n)} \cos n\theta & b_{23}^{(n)} \sin n\theta \\ b_{31}^{(n)} \sin n\theta & b_{32}^{(n)} \sin n\theta & a_{33}^{(n)} \cos n\theta \end{pmatrix}, \tag{3.11}$$

where n is the azimuthal mode number, and the mode coefficients are related to the adjoint Green's function components in accordance with:

$$\begin{pmatrix} a_{11}^{(n)} & a_{12}^{(n)} & b_{13}^{(n)} \\ a_{21}^{(n)} & a_{22}^{(n)} & b_{23}^{(n)} \\ b_{31}^{(n)} & b_{32}^{(n)} & a_{33}^{(n)} \end{pmatrix}$$
$$= \begin{pmatrix} \left(\frac{\partial \hat{G}_{1n}^a}{\partial x} - \frac{\partial \tilde{u}}{\partial x}\hat{G}_{4n}^a - \tilde{u}\frac{\partial \hat{G}_{4n}^a}{\partial x} + \gamma_n\right) & \frac{\partial \hat{G}_{2n}^a}{\partial x} & \frac{\partial \hat{G}_{3n}^a}{\partial x} \\ \left(\frac{\partial \hat{G}_{1n}^a}{\partial r} - \frac{\partial \tilde{u}}{\partial r}\hat{G}_{4n}^a - \tilde{u}\frac{\partial \hat{G}_{4n}^a}{\partial r}\right) & \left(\frac{\partial \hat{G}_{2n}^a}{\partial r} + \gamma_n\right) & \frac{\partial \hat{G}_{3n}^a}{\partial r} \\ -\frac{n}{r}\left(\hat{G}_{1n}^a - \tilde{u}\hat{G}_{4n}^a\right) & \left(-\frac{n}{r}\hat{G}_{2n}^a - \frac{1}{r}\hat{G}_{3n}^a\right) & \left(\frac{n}{r}\hat{G}_{3n}^a + \frac{1}{r}\hat{G}_{2n}^a + \gamma_n\right) \end{pmatrix}, \tag{3.12}$$

where

$$\gamma_n = \frac{1}{2}\left(i\omega\hat{p}_n^a + \tilde{u}\,\frac{\partial \hat{p}_n^a}{\partial x}\right).$$

Similarly, in the case of dipole term (3.9) the corresponding component of the propagator is given by

$$\hat{I}_{i4} = \sum_{n=0}^{\infty} \hat{I}_{i4}^{(n)}, \tag{3.13}$$

where

$$\hat{\mathbf{I}}_{i4}^{(n)} = \begin{pmatrix} c_1^{(n)}\cos n\theta & c_2^{(n)}\cos n\theta & d_3^{(n)}\sin n\theta \end{pmatrix}. \tag{3.14}$$

and the mode coefficients are related to the adjoint Green's function components in accordance with

$$\begin{pmatrix} c_1^{(n)} & c_2^{(n)} & d_3^{(n)} \end{pmatrix} = \begin{pmatrix} \frac{\partial \hat{G}_{4n}^a}{\partial x} & \frac{\partial \hat{G}_{4n}^a}{\partial r} & -\frac{n}{r}\hat{G}_{4n}^a \end{pmatrix}. \tag{3.15}$$

By integrating around the azimuthal coordinate, the final expressions for the sound spectra generated by the ring of elementary quadrupole and dipole source are obtained

$$\hat{P}_A = \pi\alpha_{ijkl}\sum_{n=0}^{\infty}(1+\delta_{n0})\left(a_{ij}^{(n)}a_{kl}^{(n)*}+b_{ij}^{(n)}b_{kl}^{(n)*}\right) \tag{3.16}$$

and

$$\hat{P}_B = \pi\beta_{ij}\sum_{n=0}^{\infty}(1+\delta_{n0})\left(c_{i}^{(n)}c_{j}^{(n)*}+d_{i}^{(n)}d_{j}^{(n)*}\right), \tag{3.17}$$

respectively.

To analyse the effect of the jet temperature gradient on noise propagation, a decomposition of the corresponding acoustic integrands is performed component-by-component via considering individual terms in (3.16) and (3.17).

3.5 Analysis of the temperature effects

All the necessary parameters for acoustic modelling in the framework of generalised acoustic analogy have been obtained from the validated LES. Far-field acoustic predictions will be compared for the range of observer angles, frequencies and sources locations. To separate the jet flow heating effect on noise propagation from other effects, the adjoint Greens function equations are solved for the cold and the hot jet flow sound propagation models separately using a locally parallel Greens function approximation.

Figures (3.5), (3.12), (3.14)–(3.17) show relative noise spectra of the cold jet flow model in comparison with the hot jet flow model. The positive differences in noise spectra levels signify noise attenuation due to the temperature gradient effect while the negative values indicate that opposite effect. In Figures (3.5a) and (3.5b), noise spectra directivities of the high-frequency quadrupole noise sources in the early shear layers and the low-frequency dipole noise sources at the end of potential core of jet, respectively, are provided. For the high-frequency quadrupole sources (see Figure 3.5a), the temperature gradient attenuates far-field sound in comparison with the cold jet. The maximum noise attenuation is around 3.3dB

and corresponds to polar angles $65 - 70°$. The observed high-frequency sound attenuation can be associated with the large temperature gradient in the early shear layers that leads to an effective noise shielding effect especially for noise source components radiating in the stream-wise direction.

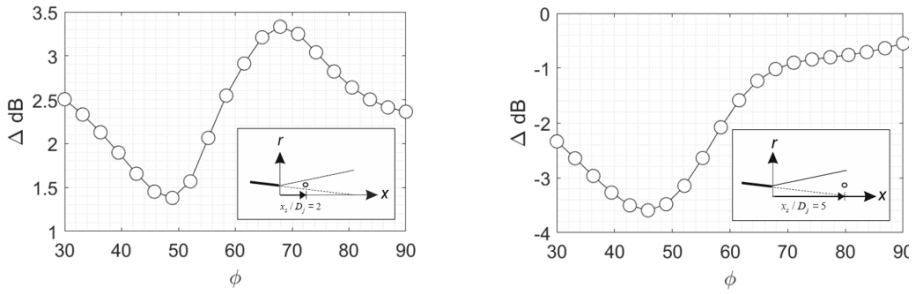

(a) $x_s / D_j = 2\,;\ St = 2\,.$ (b) $x_s / D_j = 5\,;\ St = 0.2$

Figure 3.5: Temperature gradient effect on sound radiated by the quadrupole sources in a fixed location in the jet shear layer typical of high and low frequency jet noise: change in the sound spectra directivity.

Figure (3.6a) shows that the peak high-frequency noise attenuation by the temperature gradient is caused by a strong attenuation of the stream-wise quadrupole source term R_{1111} in the hot jet flow. The sound integral decomposition into azimuthal modes demonstrates that the effect of sound attenuation by the temperature gradient is primarily due to the higher-order modes $n > 1$ as shown in Figure (3.6b).

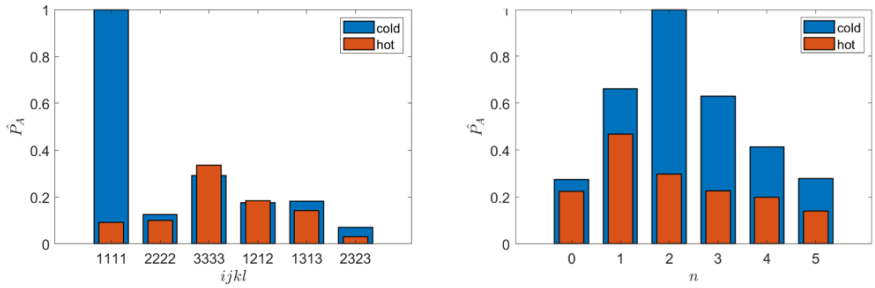

(a) $x/D_j = 2, St = 2, \phi = 65^\circ$ (b) $x/D_j = 2, St = 2, \phi = 65^\circ$

Figure 3.6: Acoustic energy budget of the high-frequency quadrupole sources radiating noise at 65° polar angle: components of different directivities (a) and different azimuthal modes (b). The amplitudes are normalised by the peak value in each case.

Analysis of the acoustic energy budget of the quadrupole sources at 90° angle (Figure 3.7a) shows that the stream-wise term R_{1111} continues to dominate at the large angles. The modal decomposition of the acoustic integral shows a further transfer of acoustic energy into high-order modes, which are attenuated by the jet temperature gradient, especially at $n = 1, 4$ and 5. The overall attenuation by the temperature gradient is partly cancelled by the sound amplification at $n = 0$ and $n = 2$.

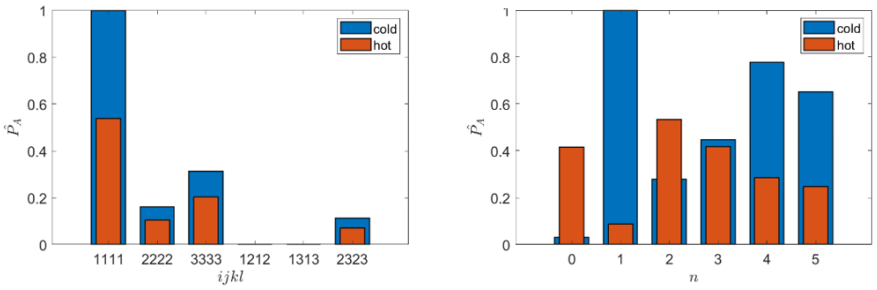

(a) $x/D_j = 2, St = 2, \phi = 90^\circ$ (b) $x/D_j = 2, St = 2, \phi = 90^\circ$

Figure 3.7: Acoustic energy budget of the high-frequency quadrupole sources radiating noise at 90° polar angle: components of different directivities (a) and different azimuthal modes (b). The amplitudes are normalised by the peak value in each case.

For sound radiating at small angles to the jet flow, the distribution of dominant sound source terms changes. In this case, the maximum contributor is the cross-term that radiates sound in the stream-wise and radial direction, R_{1212}. In terms of the acoustic mode budget, a significant attenuation of the high-frequency sound propagating at a shallow angle to the hot jet flow comes from the axisymmetric mode, $n = 0$.

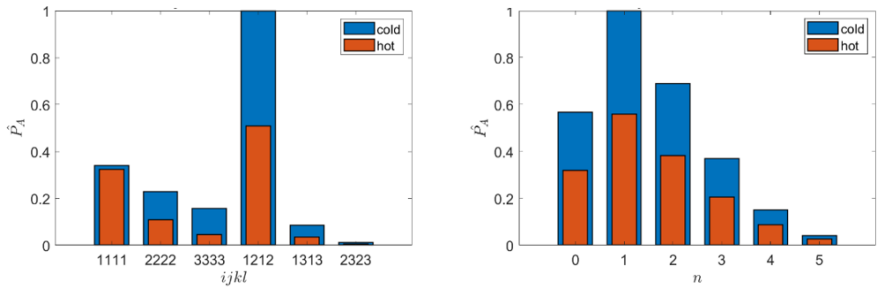

(a) $x/D_j = 2, St = 2, \phi = 30^\circ$ (b) $x/D_j = 2, St = 2, \phi = 30^\circ$

Figure 3.8: Acoustic energy budget of the high-frequency quadrupole sources radiating noise at 30° polar angle: components of different directivities (c) and different azimuthal modes (b). The amplitudes are normalised by the peak value in each case.

It is further interesting to analyse the origin of the less pronounced high-frequency noise attenuation effect of the temperature gradient at the intermediate polar angles, $45-50°$. In accordance with Figure (3.9), this can be attributed to a partial cancellation effect between the attenuated sound source in the cross-stream direction (R_{1212}) and the amplification of the stream-wise quadrupole term (R_{1111}). This interplay leads to a more-or-less uniform redistribution of the differences in radiated noise between the cold and the hot jet flow across all azimuthal modes. It can be hypothesised that the amplification of the stream-wise quadrupole noise component at intermediate polar angles relative to the cold jet may be caused by meanflow refraction due to a reduction in the effective time spent by acoustic waves in the hot jet flow where the local acoustic wavelength increases.

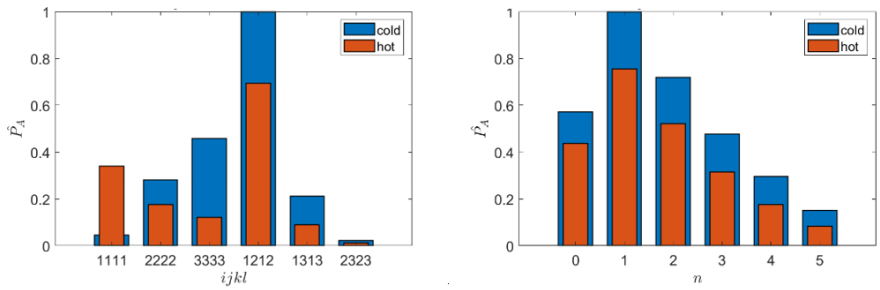

(a) $x/D_j = 2, St = 2, \phi = 45^\circ$ (b) $x/D_j = 2, St = 2, \phi = 45^\circ$

Figure 3.9: Acoustic energy budget of the high-frequency quadrupole sources radiating noise at 45° polar angle: components of different directivities (a) and different azimuthal modes (b). The amplitudes are normalised by the peak value in each case.

In contrast to high-frequencies, for low-frequency quadrupole noise (Figure 3.5b), the temperature gradient has an opposite effect: the propagated sound in the hot jet flow is amplified in comparison with the cold jet for all angles to the jet flow. The peak amplification is around 3.5dB and corresponds to polar angles $45-50°$. For small angles to the flow (Figure 3.10a,b), the sound amplification due to the temperature gradient primarily comes from the stream-wise component, R_{1111}

and the quadrupole radiating in the circumferential direction, R_{3333}. The sound amplification is mainly contributed by the axi-symmetric mode that is known to be a very important component of jet noise at low-frequencies associated with the effect of coherent structures in the jet flow [52], [24]. In the case of shallow polar angles, sound refraction by jet meanflow can be suggested as a possible major mechanism of sound amplification in the hot jet flow compared to the cold jet: due to a reduction in the effective time spent by acoustic waves in the hot jet flow in comparison with the cold jet (in comparison with discussion on Figure 3.8). For large angles to the jet (Figure 3.10c), the meanflow refraction in the hot jet flow competes with the shielding effect of the temperature gradient to attenuate sound, hence, the overal effect of the temperature on low-frequency noise propagation in the hot jet is small (Figure 3.5b).

The interplay of the two effects leads to an attenuation of the stream-wise quadrupole source component, R_{1111} but also an amplification of the quadrupole noise components which emit sound in the direction normal to the jet (R_{2222}, R_{3333}, and R_{2323}). This is also reflected in the modal destribution of the radiated sound: the effect of temperature gradient attenuates the axi-symmetric mode but, at the same time, amplifies higher-order modes, especially $n = 1$.

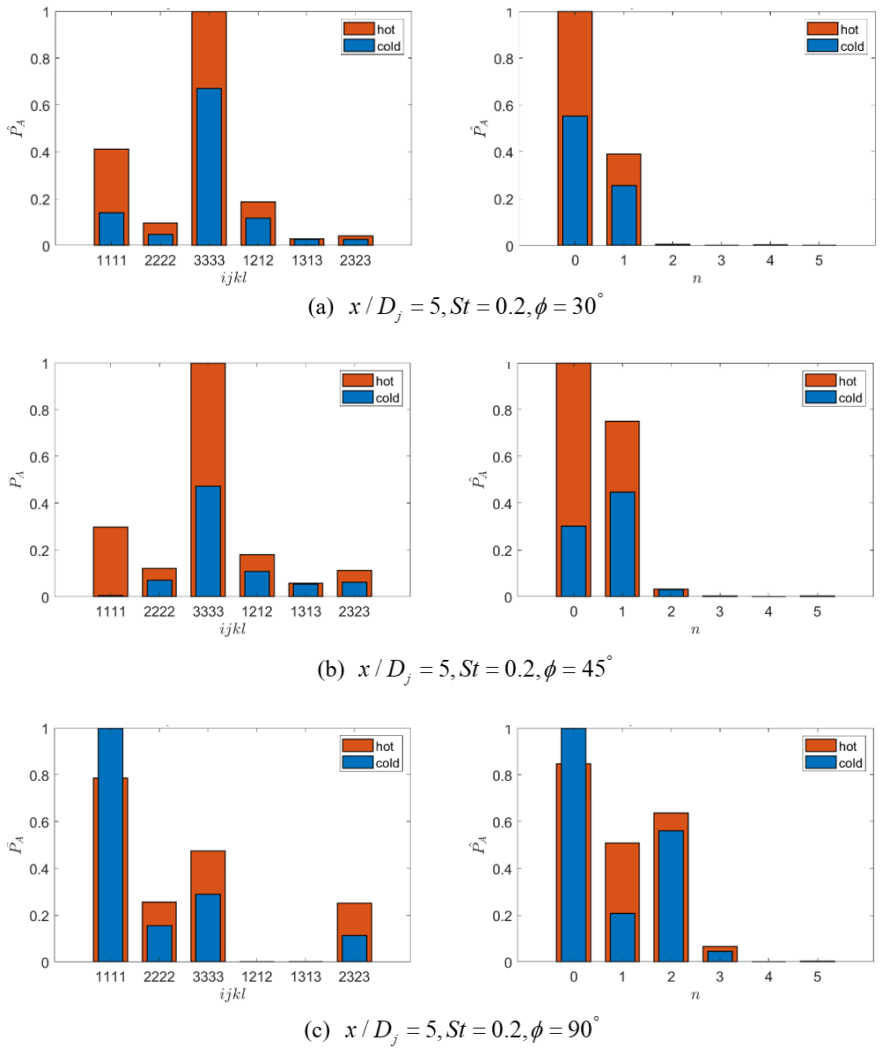

Figure 3.10: Acoustic energy budget of the low-frequency quadrupole sources corresponding to different directivities and azimuthal modes: at 30° polar angle (a), at 45° polar angle (b) and at 90° polar angle (c). The amplitudes are normalised by the peak value in each case.

In comparison with the quadrupole sources, the effect of the temperature on the dipole sources in the hot jet is always to attenuate noise as shown on Figure (3.11). The maximum attenuation of the dipole noise reaches 9dB at high frequencies at 90° polar angle (Figure 3.11a) and 5dB for low frequencies radiating at 30° angle (Figure 3.11b).

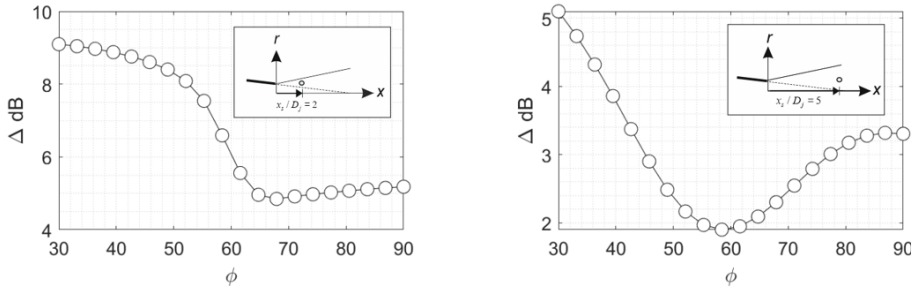

(a) $x_s / D_j = 2$; $St = 2$.

(b) $x_s / D_j = 5$; $St = 0.2$

Figure 3.11: Temperature gradient effect on sound radiated by the dipole sources in a fixed location in the jet shear layer typical of high and low frequency jet noise: change in the sound spectra directivity.

As shown in Figure (3.12a), for high-frequency noise propagation at the shallow polar angle, the effect of temperature gradient in the hot jet flow is mainly to attenuate the stream-wise component R_{11} as well as the radial component R_{22}. For the 90° angle (3.12b), the dominant dipole source component become the cross-stream ones, R_{22} and R_{33}, which are mostly affected by the jet temperature gradient. Comparison of the acoustic energy distribution across different azimuthal modes in Figure (3.12c) shows importance of all modes, including the axi-symmetric one especially for the small polar angles. For large polar angles, (3.12d) there is a partial noise cancellation effect when the temperature gradient attenuates the axi-symmetric and higher order modes, $n = 0$ and $n > 1$ but amplifies noise at $n = 1$.

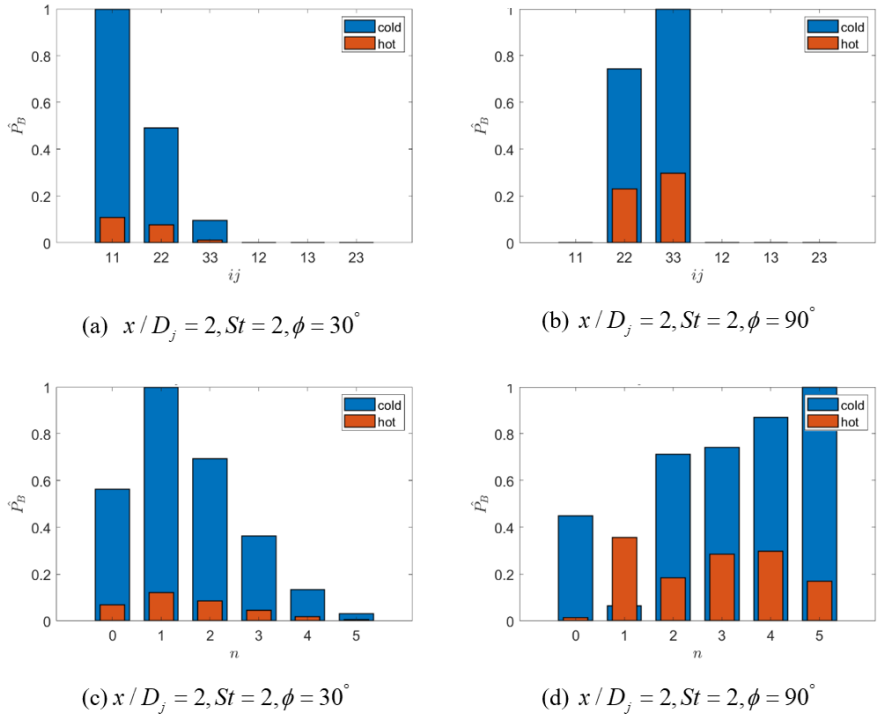

Figure 3.12: Acoustic energy budget of the high-frequency dipole sources at 30° and 90° polar angle corresponding to different directivities (a,b) and azimuthal modes (c,d). The amplitudes are normalised by the peak value in each case.

The low-frequency dipole noise is less affected by the temperature gradient at the intermediate polar angles ($\sim 65°$) where the difference in the far-field noise spectra predictions with the cold jet reduces to 2dB. In accordance with Figure (3.13), this change is associated with a redistribution of the acoustic energy when the dipole components in the jet-normal directions, R_{22} and R_{33} begin to play a more important role in comparison with the stream-wise component, R_{11}. Accordingly, the acoustic energy is redistributed from the axi-symmetric mode to higher-order modes which are less affected by shielding of the temperature gradient in this case.

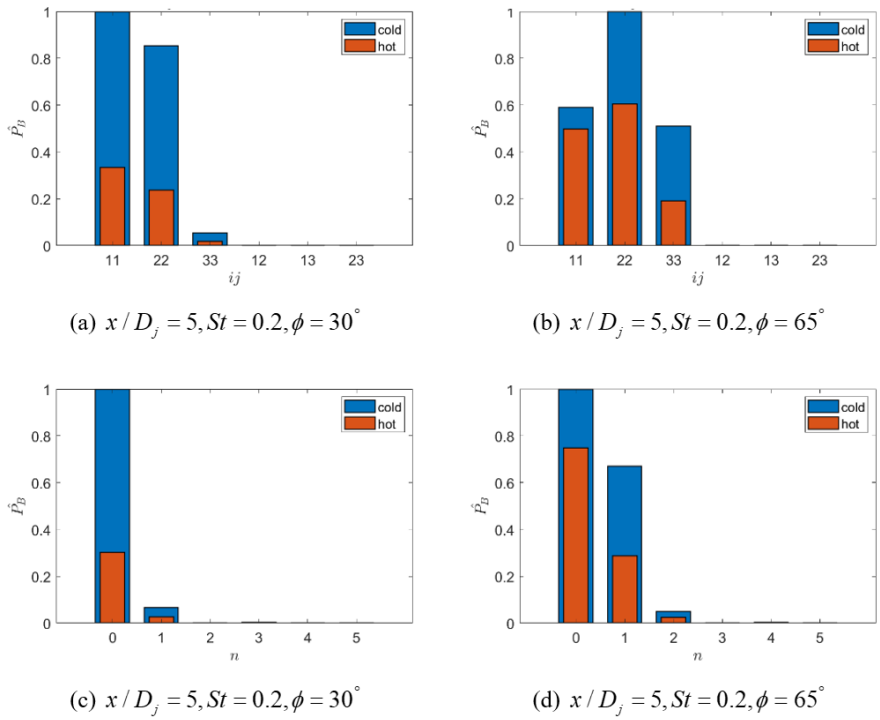

Figure 3.13: Acoustic energy budget of the low-frequency dipole sources at 30° and 65° polar angle corresponding to different directivities (a,b) and azimuthal modes (c,d). The amplitudes are normalised by the peak value in each case

The final set of the results is obtained by fixing the sound radiation angles of the quadrupole and dipole sources to 90° and 30° to the jet flow and then traversing the ring source in the stream-wise direction of the jet shear layer from $x/D_j = 1$ to the jet self-similarity region at $x/D_j = 10$. Figure (3.14) shows that the temperature effect on quadrupole noise at 90° polar angle is monotonically decreasing from the early shear layers at $x/D_j = 2 - 3$ to the jet self-similarity region $x/D_j = 10$. It can be noted that a non-monotonic change in the sound spectra due to the temperature gradient effect at $x/D_j = 1$ is likely to be caused by transitional behaviour of the LES jet flow solution due to the laminar inflow condition at the nozzle exit.

For the high-frequency noise (Figure 3.14a), the effect of the jet temperature on sound propagation is due to attenuation of the stream-wise component R_{1111}

and the reduction of amplitudes of high-order azimuthal modes (in comparison with Figure 3.7). For the low frequency noise radiation at the same angle, the temperature gradient effect is to amplify noise emitted in the vicinity of the end of potential core of the jet due to an enhanced radiation of the cross-stream jet components, R_{2222} and R_{3333} (in comparison with Figure 3.10c) which effect gradually declines further downstream of the jet where the local temperature approaches the ambient value.

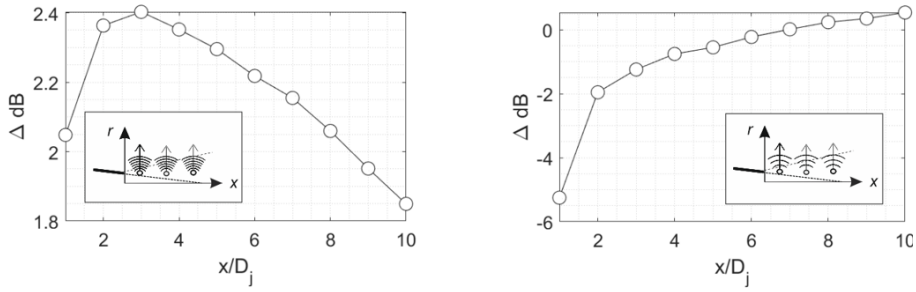

(a) ϕ=90°; $St = 2$ (b) ϕ=90°; $St = 0.2$

Figure 3.14: Temperature gradient effect on sound radiated by the quadrupole sources at 90° polar angle when changing the source location in the jet shear layer.

The effect of the temperature gradient on the dipole sound at 90° angle in Figure (3.15) monotonically decreases with the distance from the nozzle exit for all frequencies. The maximum attenuation effect of the temperature gradient on the dipole noise (∼5dB) is larger in comparison with that of the quadrupole sources (∼2dB) when considering jet locations $x/D_j > 1$ where the initial shear layers have already transitioned to turbulence. The difference between the quadrupole and the dipole noise attenuation can be attributed to a more efficient sound radiation by dipole sources, which makes the attenuated noise part also more significant in comparison with that of the quadrupole noise. For all dipole source locations, the breakdown of the acoustic energy budget at 90° polar angle shows that the dominant source components are those in the jet-normal direction, R_{22} and R_{33},

which mostly contribute to the first asymmetric, $n = 1$ and higher azimuthal source modes (in comparison with Figure 3.12).

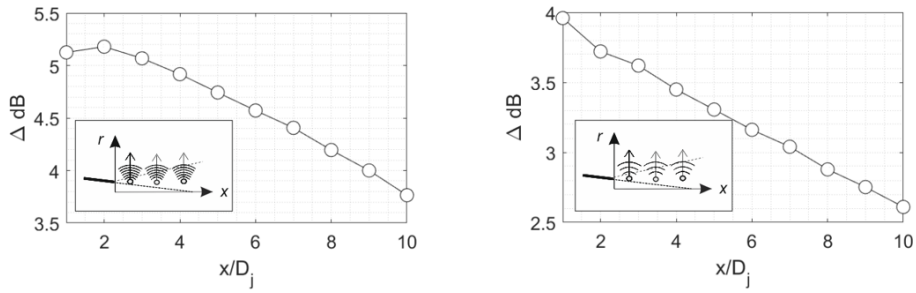

(a) ϕ=90°; $St = 2$ (b) ϕ=90°; $St = 0.2$

Figure 3.15: Temperature gradient effect on sound radiated by the dipole sources at 90° polar angle when changing the source location in the jet shear layer.

Figures (3.16)–(3.17) show the change in far-field sound spectra due to the temperature gradient effect in the same format as in Figures (3.14)–(3.15) but for sound radiated at 30° to the jet flow. For the high-frequency quadrupole sound propagation (Figure 3.16a), the effect of the temperature gradient is to quickly attenuate sound as the source distance from the nozzle exit increases. The attenuation of of the high-frequency noise at the shallow angle becomes almost complete (by 20dB) in the jet self-similarity region at $x/D_j = 10$. This attenuation is caused by the growth of the thermal shear layer that accompanies the jet spreading thereby creating an effective shielding for high-frequency sound propagating at small angles to the jet. Analysis of the acoustic energy budget shows qualitatively the same picture for all jet locations $x/D_j > 2$: the stream-wise direction component, R_{1111} and R_{1212} remain the most dominant terms (in comparison with Figure 3.8).

For the low-frequency quadrupole noise propagation as shown in Figure (3.16b), the maximum amplification occurs downstream of the end of the potential core of the jet, around $x/D_j = 5 - 9$, but the total effect in comparison with the

cold jet does not exceed 2.5 dB. Dominant quadrupole noise components include the circumferential component, R_{3333} and the stream-wise component, R_{1111} (compare with Figure 3.10). The azimuthal mode content of the low frequency sound propagation includes the axi-symmetric and the first asymmetric mode, $n = 0$ as well as higher-order modes for the high-frequency case.

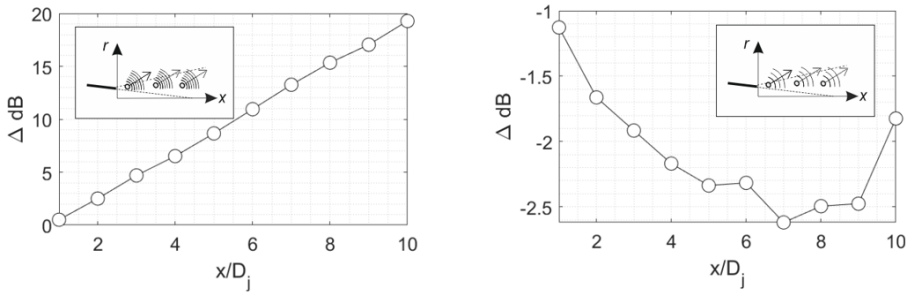

(a) ϕ=30°; St = 2 (b) ϕ=30°; St = 0.2

Figure 3.16: Temperature gradient effect on sound radiated by the quadrupole sources at 30° polar angle when changing the source location in the jet shear layer.

In comparison with the high-frequency quadrupole sound, the high-frequency dipole sound attenuation by the temperature gradient with distance from the nozzle exit is even faster: the attenuation reaches 15dB already at the end of the potential core of the jet, $x/D_j = 5$. The structure of the high-frequency dipole source at 30° angle remains approximately the same for all source solutions: the most domain components are in the stream-wise and radial jet direction, R_{11} and R_{22} which mainly include azimuthal modes $n = 0, 1, 2$, and 3 as shown in Figure (3.12). In contrast with the higher frequencies, for low-frequency dipole sound propagation, the noise attenuation effect of the temperature gradient decays with the distance from the nozzle exit: the noise reduction is 7dB at $x/D_j = 2$ and becomes 4dB at $x/D_j = 10$.

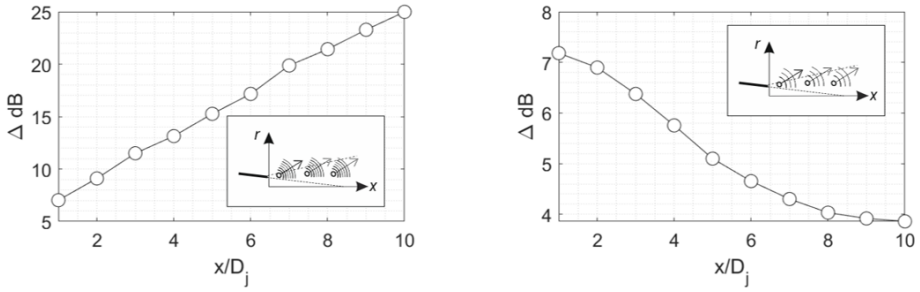

(a) ϕ=30°; $St = 2$ (b) ϕ=30°; $St = 0.2$

Figure 3.17: Temperature gradient effect on sound radiated by the quadrupole sources at 30° polar angle when changing the source location in the jet shear layer.

By analysing individual components of the acoustic integral as shown in Figure (3.18) , the observed reduction of the temperature gradient attenuation effect on the low-frequency dipole noise downstream of the jet can be explained by the acoustic energy redistribution to the single most dominant stream-wise source component, R_{11} downstream of the jet. This component seems to be strongly affected by the temperature gradient in the jet. This is accompanied by a redistribution of acoustic energy of the dipole source from almost fully axi-symmetric source at $x/D_j = 2.5$ to the source that includes both the axi-symmetric and the first asymmetric mode $n = 1$ at $x/D_j = 10$. The low-frequency dipole noise shielding by the temperature gradient seems to manly affect the radial source component, R_{22} and the axi-symmetric mode, which importance reduces downstream of the jet in this case.

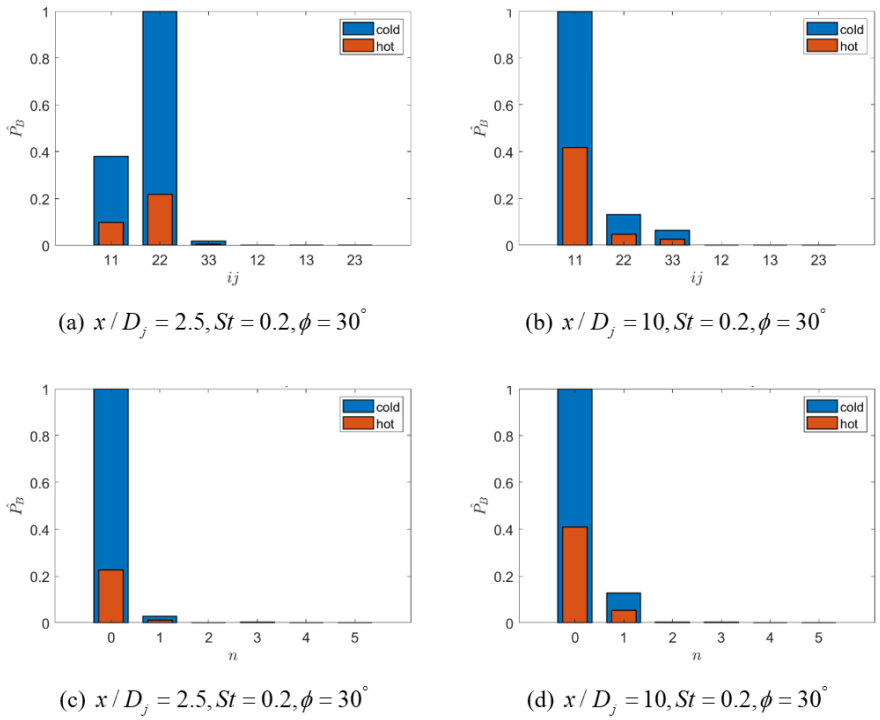

(a) $x/D_j = 2.5, St = 0.2, \phi = 30^\circ$ (b) $x/D_j = 10, St = 0.2, \phi = 30^\circ$

(c) $x/D_j = 2.5, St = 0.2, \phi = 30^\circ$ (d) $x/D_j = 10, St = 0.2, \phi = 30^\circ$

Figure 3.18: Acoustic energy budget of the low-frequency dipole sources at 30° polar angle in the early shear layers and the end of potential core region corresponding to different directivities (a,b) and azimuthal modes (c,d). The amplitudes are normalised by the peak value in each case.

Summary

The non-uniform temperature distribution effect on noise propagation in a hot jet flow has been analysed for conditions of the hot SILOET jet experiment. In the framework of the Goldstein generalised acoustic analogy, two elementary ring source models are considered in the jet shear layers. The models correspond to elementary quadrupole and dipole sources as representative of the considered jet case.

Distributions of the relative source strengths and the meanflow parameters of the jet are obtained from the statistically well-converged Large Eddy Simulation

solution which is validated in comparison with the far-field microphone SILOET data and predictions of the empirical sJet model that was previously calibrated on a large dataset of single-stream NASA jet flows.

Predictions of the far-field sound spectra radiated by the elementary sources are obtained using a semi-analytical vector adjoint Green's function method with and without taking into account the jet temperature gradient. Two series of numerical experiments are conducted. In the first set, the location of the elementary high- and low-frequency sources is fixed to early shear layers and the end of potential core location, respectively, to study the temperature gradient effect on noise directivity. In the second set of experiments, for two typical noise emission angles, 30° and 90° to the jet flow, the stream-wise location of the ring sources in the jet is changed to study the effect of the source position on noise propagation. Generally, the obtained results strongly suggest that taking into account the thermal layer of a hot jet is not only important for modelling of jet noise propagation at small angles to the jet flow but also at the 90° polar angle, where the sensitivity is especially strong for the dipole-type sources for many sound frequencies including the one which corresponds to the peak jet noise at $St_D = 0.2$.

In particular, the simulations reveal that the temperature gradient effectively shields the dipole noise and the quadrupole noise at high frequencies. The high-frequency quadrupole noise reduction by the temperature gradient is about 2.5dB on average. The temperature effect on high-frequency quadrupole noise directivity does not have a linear dependency on the polar angle. Analysis shows that the sound attenuation at large angles is mostly caused by damping of the stream-wise quadrupole source term R_{1111} that mostly contribute due to the higher-order azimuthal modes $n > 1$. For small polar angles, the cross-term, R_{1212} that radiates sound in the stream-wise and radial direction and the axi-symmetric source mode, $n = 0$ become important.

For intermediate polar angles, $45 - 50°$ there is a partial cancellation effect

between the attenuated sound source in the cross-stream direction (R_{1212}) and the amplification of the stream-wise quadrupole term (R_{1111}). In comparison with the high-frequency noise propagation, the presence of temperature gradient amplifies the low-frequency quadrupole noise. The peak amplification is around 3.5dB and corresponds to polar angles $45-50°$. This effect reduces at high polar angles. The sound amplification primarily comes from the stream-wise component, R_{1111} and the quadrupole radiating in the circumferential direction, R_{3333}. The quadrupole sound amplification is mainly due to enhancement of the axi-symmetric mode that is known to be the most significant component of jet noise at low-frequencies. In the case of small polar angles, sound refraction by jet meanflow can be suggested as a possible major mechanism of sound amplification in the hot jet flow compared to the cold jet: due to a reduction in the effective time spent by acoustic waves in the hot jet flow in comparison with the cold jet.

For dipole noise sources, the effect of the temperature gradient is always to decrease noise. The noise attenuation is maximum at small angles to the jet where it can reach 5-9dB and decays to 3-5dB at higher angles, depending on the frequency. The change in the emitted sound follows the change in the jet noise directivity which at the shallow angles is dominated by the stream-wise component R_11 and the radial component R_{22} whilst the sound attenuation at large angles is dominated by R_{22} and R_{33} components. The temperature gradient effect on the dipole noise tends to decline with increase of the polar angle following the decline of the axi-symmetric source mode component.

By computing the far-field noise spectra corresponding to different locations of the quadrupole ring source in the jet, it is shown that the temperature effect on quadrupole noise at 90° polar angle is monotonically decreasing from the early shear layers at $x/D_j = 2-3$ to the jet self-similarity region $x/D_j = 10$. The structure of the dominant source terms remains approximately the same for all source locations. For the dipole sources, the effect of temperature gradient at 90° angle

monotonically decreases with the distance from the nozzle exit for the high and the low frequencies. The maximum attenuation effect of the temperature gradient on the dipole noise is about 5dB which can be compared with the maximum 2dB attenuation obtained for the quadrupole sources as the same polar angle and range of locations in the jet. The difference between the attenuation of the sources of different directivity can be attributed to a more efficient sound radiation by dipole sources, which makes the attenuated noise part also larger in comparison with that of the quadrupole noise.

For high-frequency sound propagation at 30° angle to the jet flow, the temperature gradient effect on quadrupole and dipole noise sources quickly decays with distance from the nozzle exit. The attenuation becomes almost complete (by 20dB or more) in the jet self-similarity region at $x/D_j = 10$. The attenuation is caused by the growth of the thermal shear layer that accompanies the jet spreading thereby creating an effective shielding for high-frequency sound propagating at small angles to the jet. For the low-frequency quadrupole noise propagation, the maximum attenuation occurs downstream of the end of the potential core of the jet around $x/D_j = 5 - 9$ but the total effect in comparison with the cold jet does not exceed 2.5 dB.

In contrast with the higher frequencies, for low-frequency dipole sound propagation, the noise attenuation effect of the temperature gradient decays with the distance from the nozzle exit: the noise reduction is 7dB at $x/D_j = 2$ and becomes 4 dB at $x/D_j = 10$. In this case, analysis shows that the low-frequency dipole noise shielding by the temperature gradient seems to manly affect the radial source component, R_{22} and the axi-symmetric mode, which importance reduces downstream of the jet.

Chapter 4

RANS-based schemes for single-stream jet noise predictions

4.1 Review of RANS based jet noise prediction models

Acoustic predictions models based on RANS solutions have a reasonable computational cost in comparison with high fidelity methods such as LES. Using the RANS-based tools, the user can vary several operating conditions and nozzle geometries within a short time frame for acoustic predictions. The input required for these models includes meanflow fields and characteristic scales of turbulence which can be obtained from turbulent kinetic energy and dissipation rate. These quantities can be readily calculated using a number of commercial RANS CFD solvers such as ANSYS Fluent [39]. On the other hand, the high-order statistical moments such as the covariance of fluctuating turbulent stress (1.36) which are essential for the definition of the acoustic source amplitude and scales are not available from RANS. Typically, one needs to use some calibration to derive the acoustic parameters from the RANS fields. The calibration typically involves acces

to the experimental far-field noise measurements, e.g. to find the best set of model coefficient for one observer angle, e.g. 90° angle to the jet axis and then use the obtained parameters for all other angles. In some cases, however, it is possible to use LES data to derive the required calibration coefficients directly from the flow solution.

In this Chapter, several RANS-based acoustic models are considered and their predictions are compared for the conditions of the cold and the heated SILOET jet experiment.

The fine-scale jet noise model by Tam and Auriault [21] is considered first. The development of this model was motivated by the analogy with the kinetic theory of gases. In the framework of this model, the statistics of the turbulent source is modeled as an auto-covariance of the convective derivative of the fluctuating Reynolds stresses, which is approximated by a Gaussian function. As it was pointed out in the work of Morris and Farassat [66], the Tam and Auriault model can be re-arranged to an acoustic analogy form. Similar to acustic analogy models, the source coefficients of the fine scale model can be obtained from a RANS solution where a set of calibration parameters is used.

An example of popular acoustic analogy model for jet noise based on RANS is the model that has been developed in the series works of Khavaran [27], [29], [30] . These models are based on a simplified version of the Goldstein generalised acoustic analogy. In particular, the simiplifications adopted in the Khavaran model include the following: it (i) agglomerates all individual source terms corresponding to different directivity into a single effective source strength based on the isotropic turbulence model, (ii) uses an additional calibration parameter to estimate the eddy convection velocity based on the jet flow velocity value at the nozzle exit and the local flow velocity, and (iii) considers the effective sound sources in the reference frame moving with the jet flow, which results in an explicit convective application factor.

In comparison with the Tam and Auriualt model, the Khavaran model for heated jet noise predictions [29] is designed to predict noise both large and small polar angles to the jet. It also includes noise contributions from the sources based on the fluctuating Reynolds stresses typical of the isothermal jets as well as the enthalpy fluctuation source term that is important for heated jets. The momentum and enthalpy sources in this model are assumed to be statistically independent.

The third type of models considered here is the implementation of Goldstein generalised acoustic analogy by Karabasov et al.[5]. In comparison with the Khavaran model, this model includes several noise source components of different directivity. Keeping the individual source directivity was important to correctly take into account the effect of amplification or attenuation of the noise sources due to the individual propagation effects by each term thereby reproducing the well-known directivity features of jet noise without introducing additional empirical parameters such as the adjustable eddy condvection speed of the Khavaran model.

Additional important feature of the generalised acoustic analogy model implementation by Karabasov et al. is that the source modelling is performed in the nozzle reference frame thereby making it easy to compare with the LES solutions that are typically obtained in the nozzle frame. However, the generalized acoustic analogy implementation by Karabasov et al. [5] has been limited to single-stream unheated jets. Therefore, one of the goals of the current thesis is to extend it to heated and co-axial jet cases.

4.2 Implementation of the Tam and Auriault model

Following Tam and Auriault [21], the far-field pressure is expressed as a convolution of the relevant Green's function and the convective derivative of the effective sound

source

$$p(\mathbf{x},t)=\int_V\int_{-\infty}^{\infty}\left(\int_{-\infty}^{\infty}p_a(\mathbf{x},\mathbf{x_1},\omega)\exp(-i\omega(t-t_1))d\omega\right)\frac{Dq_s(\mathbf{x_1},t_1)}{Dt_1}dt_1d\mathbf{x}_1, \tag{4.1}$$

where p_a is the adjoint pressure component of the corresponding vector adjoint Green's function and D/Dt is the convective derivative. The entire source including the moving frame effects is modelled statistically in accordance with the Gaussian representation of the appropriate two-time two-space auto-correlation function:

$$\overline{\frac{Dq_s(\mathbf{x_1},t_1)}{Dt_1}\frac{Dq_s(\mathbf{x_2},t_2)}{Dt_2}}\sim\exp\left[-\frac{|\Delta_1|}{\tilde{u}\tau_s}-\frac{\ln 2}{l_s^2}\left((\Delta_1-\tilde{u}\tau)^2+\Delta_2^2+\Delta_3^2\right)\right]. \tag{4.2}$$

After a number of assumptions, which include , including the locally parallel flow and the compact source scale approximations, the final prediction formula for the far field-noise power spectral density is given by

$$S(\mathbf{x},\omega)=4\pi\Big(\frac{\pi}{\ln 2}\Big)^{3/2}\int_V|p_a(\mathbf{y},\mathbf{x},\omega)|^2\frac{\hat{q}_s^2l_s^3}{c^2\tau_s}\frac{\exp\left[-\omega^2l_s^2/\bar{u}^2(4\ln 2)\right]}{1+\omega^2\tau_s^2(1-\bar{u}/c_\infty\cos\phi)^2}d\mathbf{y}. \tag{4.3}$$

Here functions (l_s), (τ_s) are characteristic size of fine-scale turbulence and characteristic decay time of the same, respectively. The scales can be determined from RANS solution and defined as

$$l_s=c_\ell\frac{\kappa^{1.5}}{\varepsilon}, \tag{4.4}$$

$$\tau_s=c_\tau\frac{\kappa}{\varepsilon}, \tag{4.5}$$

where κ is averaged turbulent kinetic energy and ε is the dissipation rate of small-scale turbulence,

$$\hat{q}_s^2/c^2=A^2\left(\frac{2}{3}\bar{\rho}\kappa\right)^2. \tag{4.6}$$

The empirical constants c_l, c_τ and A are determined by the best fit to the far field experimental data of SILOET experiment at 90° observer angle. It can be noted

that in the current implementation of this model for the SILOET jet, the obtained best-fit calibration parameters are different in comparison with the original values suggested in [21].

	Tam and Auriault [21]	Best fit SILOET
c_l	0.256	0.5
c_τ	0.233	0.4
A	0.755	0.55

Table 4.1: Calibration coefficients to close acoustic model of Tam and Auriault.

The far-field spectra predictions of the Tam and Auriault model for both sets of coefficients are provided in the results section.

4.3 Implementation of the Khavaran model

In comparison with the fine-scale Tam and Auriault model, the far-field noise spectral density of the Khavaran model is given as a linear combination of two independent sources. On source is responsible for the fluctuating Reynolds stresses and the other stands for the fluctuating enthalpy noise. It is assumed that the momentum and the enthalpy sources are statistically independent. The two sources correspond to subscripts A and B in the formula below

$$\overline{p^2}(x, r, \omega) = AF_A + BF_B, \tag{4.7}$$

$$F_A = |\cos^2\phi + Q\sin\phi|^2 F, \quad F_B = (1 - M^s\cos\phi)^2 \frac{15}{16}\frac{c_\infty^2}{\kappa}\frac{\overline{h_t'^2}}{\widetilde{h^2}}F, \tag{4.8}$$

$$F = \frac{\rho_\infty^2 I_{1111} k^4 (1 - M^s\cos\phi)^2 |\cos^2\phi + Q\sin\phi|^2}{(4\pi R)^2(1 - M_c\cos\phi)^2}\sum_{n=0}^{\infty}(1 + \delta_{0n}) f_n f_n^*. \tag{4.9}$$

Here $k = \omega/c_\infty$ is the wave number, $M^s = U/c_\infty$ is the acoustic Mach number, $M_c = U_c/c_\infty$ is the convective Mach number, U_c is the convective velocity (effec-

tive velocity of turbulent eddies). I_{1111} is the source,f_n are modes of the Green's function, $\overline{h_t'^2}/\tilde{h^2}$ is the enthalpy factor.

$$Q^2 = \Phi^2 - \cos^2\phi, \quad \Phi^2 = \frac{\rho}{\rho_\infty}(1 - M^s\cos\phi)^2. \tag{4.10}$$

In addition to the convective amplification factor in the denominator of (4.9) that is a consequence of specifying the sources in the moving frame, an important parameter of the Khavaran's model is the convective velocity U_c, which is defined as

$$U_c = aU(x,r) + bU_j \tag{4.11}$$

with non-negative coefficients a and b. It should be noted that $a+b$ is not equal to 1 necessarily, for example, in [27] the suggested values are: $a = 0.25$, $b = 0.5$. It can be pointed out that the parameters a and b are additional calibration parameters of the Khavaran model. The amplitude coefficients, A and B are found by the best fit of noise spectra predictions to the experimental data for the polar angle 90° for both the isothermal and the heated jet cases. Then, the same set of A and B is used for the noise spectra predictions at the polar angles $60^\circ$and 30° to the jet flow. The B term in (4.8) is the amplitude of the fluctuating enthalpy noise term $\overline{h_t'^2}/\tilde{h^2}$, where h is the enthalpy and h_t' is the fluctuation of total enthalpy, which is important for heated jet noise.

In accordance with [29] the source component is given by

$$I_{1111}(\mathbf{y},\omega) = \frac{4{l_s}^3}{5\pi^2}\left(\overline{u_1^2}\right)^2 H(\omega^s)N(k\ell), \tag{4.12}$$

where

$$H(\omega^s) = \frac{\tau_s}{1 + (\omega^s\tau_s/2)^2}, \quad \omega^s = (1 - M_c\cos\phi)\omega, \tag{4.13}$$

$$N(2\pi\chi) = \frac{5}{8\chi^5}\left(3\arctan\chi - \chi\frac{5\chi^2+3}{(1+\chi^2)^2}\right) \tag{4.14}$$

is the so-called non-compactness factor. The turbulence length- and time-scale are defined similar to Tam and Auriault (4.4), (4.5). The fluctuation of total enthalpy h_t' which comes in $\overline{h_t'^2}/\tilde{h}^2$ is not available from RANS solution directly, therefore, the following empirical model is suggested in the work of Khavaran [29]

$$\overline{h_t'}/\widetilde{h} \approx F_T, \tag{4.15}$$

where

$$F_T = \left(\left|\frac{dT_t}{dr}\right| \frac{D_j}{T_\infty}\right)^{\zeta} \frac{(1-1/\mathrm{NTR})^{\delta}}{6}\chi, \quad \chi = \begin{cases} \chi_0 + (1-\chi_0)t, & t \le 1, \\ 1, & t > 1, \end{cases} \tag{4.16}$$

where $t = x/L_c$, where L_c is the length of the potential core in the jet, $\zeta = 0.2$, $\chi_0 = 0.7$, $\delta = 1 + 1/(3\mathrm{NPR})$, and NTR and NPR are the nozzle temperature ratio and the nozzle pressure ratio parameters, respectively.

Figure 4.1 shows F_T function for the heated SILOET jet case.

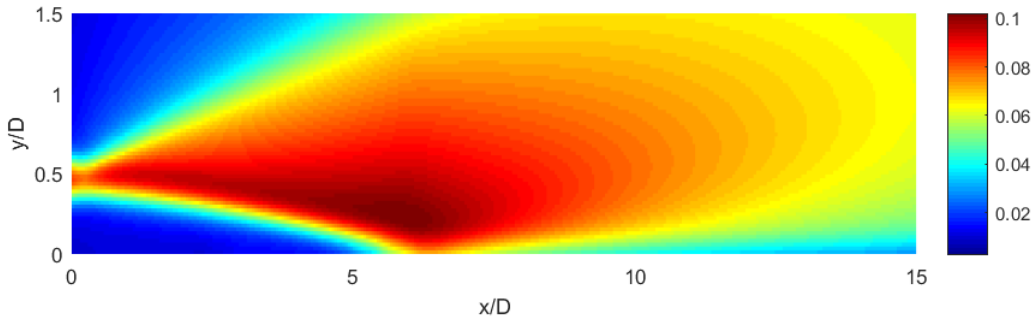

Figure 4.1: Distribution of the fluctuating enthalpy source function F_T obtained from the RANS calculation of the heated SILOET jet case.

Following [29], the relevant Green's function in the laboratory frame, which includes a correction for the convective amplification, is defined as

$$G(\mathbf{x}, \mathbf{y}, \omega) = \frac{-\mathrm{i}}{4\pi R} \frac{1 - M^s \cos\phi}{1 - M_c \cos\phi} e^{\mathrm{i}kR} \sum_{n=0}^{\infty} f_n(r^s, k, \phi) \cos n(\theta - \theta^s), \tag{4.17}$$

where modes f_n are the solutions of the Rayleigh-type equation:

$$\frac{d}{dr}\left(\frac{r}{\Phi^2}\frac{d}{dr}g_n\right)+\frac{r}{\Phi^2}\left(k^2Q^2-\frac{n^2}{r^2}\right)g_n=0,\quad g_n=(1-M^s\cos\phi)^3 f_n. \tag{4.18}$$

The verification of the propagation part of the Khavaran model for a heated jet flow is presented in Appendix C. The calibration coefficients of this jet noise model obtained for the SILOET jets are $c_l=0.5$, $c_\tau=0.4$ in (4.12); $A=9$, $B=3$ in (4.7) and $a=0$, $b=0.8$ in (4.11). The sound spectra predictions resulting from this choice of coeffients are considered in the results section.

4.4 Generalised acoustic analogy model with including the individual source directivity and the fluctuating enthalpy source

In comparison with the Khavaran model, the implementation of the generalised acoustic analogy by Karabasov et al. [5] retains individual source directivity, operates in the nozzle reference frame, and also uses LES to inform the RANS-based source scales. In this thesis, the same approach to implementation of the generalised acoustic analogy is adopted while extending it to account for the temperature effect following the Khavaran model [29]. Assuming that the fluctuating Reynolds stress source and the the fluctuating enthalpy source are not correlated, the power spectral density breaks down into the "cold" and the "heated" source contributions,

$$\hat{P}(\mathbf{x},\omega)=P_A+P_B \tag{4.19}$$

$$\hat{P}_A(\mathbf{x},\omega)=\int_V\int_V \hat{R}_{ijkl}(\mathbf{y},\boldsymbol{\Delta},\omega)\hat{I}_{ij}(\mathbf{y},\omega;\mathbf{x})\hat{I}^*_{kl}(\mathbf{y}+\boldsymbol{\Delta},\omega;\mathbf{x})d\boldsymbol{\Delta}d\mathbf{y}, \tag{4.20}$$

$$\hat{P}_B(\mathbf{x},\omega)=\int_V\int_V \hat{R}_{i4j4}(\mathbf{y},\boldsymbol{\Delta},\omega)\hat{I}_{i4}(\mathbf{y},\omega;\mathbf{x})\hat{I}^*_{k4}(\mathbf{y}+\boldsymbol{\Delta},\omega;\mathbf{x})d\boldsymbol{\Delta}d\mathbf{y}, \tag{4.21}$$

where, similar to (4.7), indices A and B stand for the cold and the heated source parts, respectively, and their corresponding stresses are

$$T'_{ij} = \left(\rho v'_i v'_j - \bar{\rho}\widetilde{v'_j v'_j}\right), \quad H'_{j'} = \left(\rho v'_j h'_0 - \bar{\rho}\widetilde{v'_j h'_0}\right). \tag{4.22}$$

The fluctuating quadrupole source is approximated by the same Gaussian-exponential model as in [21]

$$R_{ijkl}(\mathbf{y}, \boldsymbol{\Delta}, \tau) = A_{ijkl}(\mathbf{y}) \exp\left[-\frac{|\Delta_1|}{\tilde{u}\tau_s} - \frac{\ln 2}{l_s^2}\left((\Delta_1 - \tilde{u}\tau)^2 + \Delta_2^2 + \Delta_3^2\right)\right]. \tag{4.23}$$

To approximate the fluctuating enthalpy term, it is assumed that the former scales with the velocity auto-correlation function,

$$R_{i4j4}(\mathbf{y}, \boldsymbol{\Delta}, \omega) \sim C \cdot R_{ij}(\mathbf{y}, \boldsymbol{\Delta}, \omega) F_T(\mathbf{y}), \tag{4.24}$$

where C is some constant proportionality coefficient.

Here the velocity autocorrelation function

$$R_{ij}(\mathbf{y}, \boldsymbol{\Delta}, \tau) = \overline{v'_i(\mathbf{y}, t) v'_j(\mathbf{y} + \boldsymbol{\Delta}, t + \tau)} \tag{4.25}$$

is approximated similar to the quadrupole sources (4.23) using a Gaussian-exponential shape function

$$R_{ij}(\mathbf{y}, \boldsymbol{\Delta}, \tau) = B_{ij}(\mathbf{y}) \exp\left[-\frac{|\Delta_1|}{\tilde{u}\tau_s} - \frac{\ln 2}{{l_s}^2}\left((\Delta_1 - \tilde{u}\tau_s)^2 + {\Delta_2}^2 + {\Delta_3}^2\right)\right]. \tag{4.26}$$

Assuming that the compact source scale and the locally parallel jet flow approximations are valid, as used in the case of the Tam and Auriault and the Khavaran models, the final noise spectra prediction formula becomes

$$\hat{P}(\mathbf{x}, \omega) = \int_V \left(A_{ijkl}(\mathbf{y}) W(\mathbf{y}) \hat{I}_{ij} \hat{I}^*_{kl} + B_{ij}(\mathbf{y}) W(\mathbf{y}) \hat{I}_{i4} \hat{I}^*_{k4}\right) d\mathbf{y} = \hat{P}_A + \hat{P}_B, \tag{4.27}$$

The mean flow gradients are obtained from the RANS solution and the function $W(\mathbf{y})$ which emerges as a result of the integration, is:

$$W(\mathbf{y}) = \left(\frac{\pi}{\ln 2}\right)^{3/2} \frac{2l_s^3\tau_s}{1+\left(\omega(1-\tilde{u}/c_\infty\cos\phi)\tau_s\right)^2} \exp\left(-\frac{(\omega l_s/\tilde{u})^2}{4\ln 2}\right), \tag{4.28}$$

where

$$A_{ijkl}(\mathbf{y}) = C^A_{ijkl}(2\bar{\rho}\kappa)^2, \quad B_{ij}(\mathbf{y}) = C^B_{ij}\rho_\infty c_\infty^4 \bar{\rho}\kappa \frac{\overline{h_t'^2}}{\widetilde{h^2}}. \tag{4.29}$$

Here C^A_{ijkl} and C^B_{ij} are dimensionless source strength parameters obtained from LES solution as discussed in Chapter 3 the resulting values are summarised in table 4.2 and averaged over the jet shear layer. The enthalpy term $\overline{h_t'^2}/\widetilde{h^2}$ is approximated using the empirical function F_T as in the Khavarn model [29]. As noted in the introduction, in comparison with the Tam and Auriault and Khavaran models, the present model uses the LES to calculate dimensionless correlation amplitudes required to supplement the RANS flow solution. In this work those coefficients are based on the heated SILOET jet. In comparison with tables 3.1 and 3.2 from Chapter 3, all the normalisation is done on the square of the turbulent kinetic energy (κ^2) and the dimensionless source strengths, which are obtained by averaging over the jet shear layer, are summarised in Tables 4.2 and 4.3. It can be reminded that index 1- is in the jet flow direction and 2,3 are in the normal plane to the jet.

ij, kl	11,11	22,22	33,33	12,12; 12,21; 21,12; 21,21	13,13; 13,31; 31,13; 31,31	23,23; 23,32; 31,13; 31,31
	0.64	0.114	0.17	0.175	0.175	0.069

Table 4.2: Non-dimensional quadrupole source amplitudes.

ij	11	22	33	12,	13	23
	1.06	0.47	0.47	0.7	0.7	0.0690.47

Table 4.3: Non-dimensional dipole source amplitudes.

The length and time scales are determined from RANS and the same dimensionless scaling coefficients are used for the term A and B, c_ℓ= 0.5; c_τ= 0.4. The dimensionless strength parameters of the fluctuating Reynolds tress and the enthalpy source are $A = 0.2$ and $B = 1$, respectively.

4.5 Results of the acoustic modelling

Figs.4.2-4.6 show the noise spectra predictions for the three considered RANS-based acoustic models for jet nose predictions for the isothermal and heated SILOET jets at the 90°, 60°and 30°polar angles. Experimental data are presented in the same figures for comparison. In each model, the set of suitable calibration coefficients is fixed for all jet cases and polar angles. The calibration parameters are obtained by fitting the 90°noise spectra predictions to the far-field noise data in each case. In the case of the Tam and Auriault and the Khavaran models, there are two sets of predictions shown: one is based on the best calibration parameters found in this work and the other one is obtained for the recommended parameters from the original publications. As expected, it was impossible to find a single set of the calibration parameters for the fine-scale Tam and Auriault model which would lead to satisfactory noise spectra predictions for all observer angles. For the current best set of calibration parameters, the differences for spectra predictions in comparison with the experiment are about 6dB for all angles other than 90° (Fig.4.2). It can also be seen that for the recommended set of calibration parameters the shape of the predicted spectra is markedly offset at all angles (Fig.4.3). The noise spectra predictions of the Khavaran model are within 2-3dB from the

experiment for both the cold and the heated jets for all three angles and for the same range of frequencies $0.04 < St < 2-3$ (Fig.4.4). However, it should be noted that these good noise predictions are based on assuming quite a large convective velocity of the source compared to the standard value $U_c \sim 0.65U_j$. Similar to the Tam model, the recommended set of parameters applied to the Khavaran model leads to the spectra predictions being largely offset in comparison with the experimental data (Fig.4.5). Finally, the results of the new model developed in this thesis for the cold and the heated jet cases are presented in Fig.4.6. The noise spectra predictions within 2dB from the experiment for both the isothermal and the heated jet for all three angles and most frequencies within $0.04 < St < 2 - 3$.

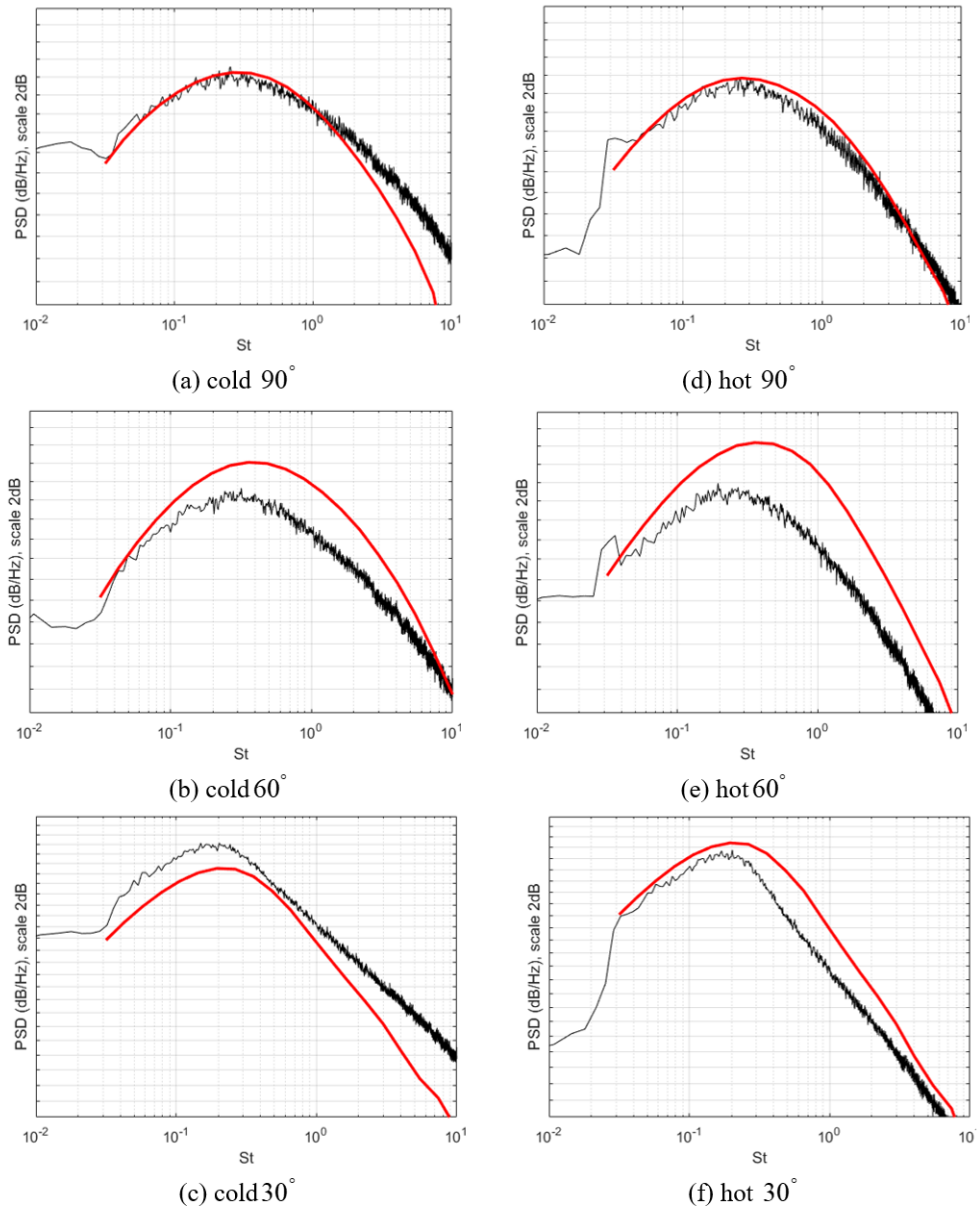

Figure 4.2: Far-field noise spectra predictions of the Tam and Auriaut model for cold (a, b, c) and hot (d, e, f) static SILOET jet for the 90°, 60°and 30°polar angle for the best fitted calibration parameters.

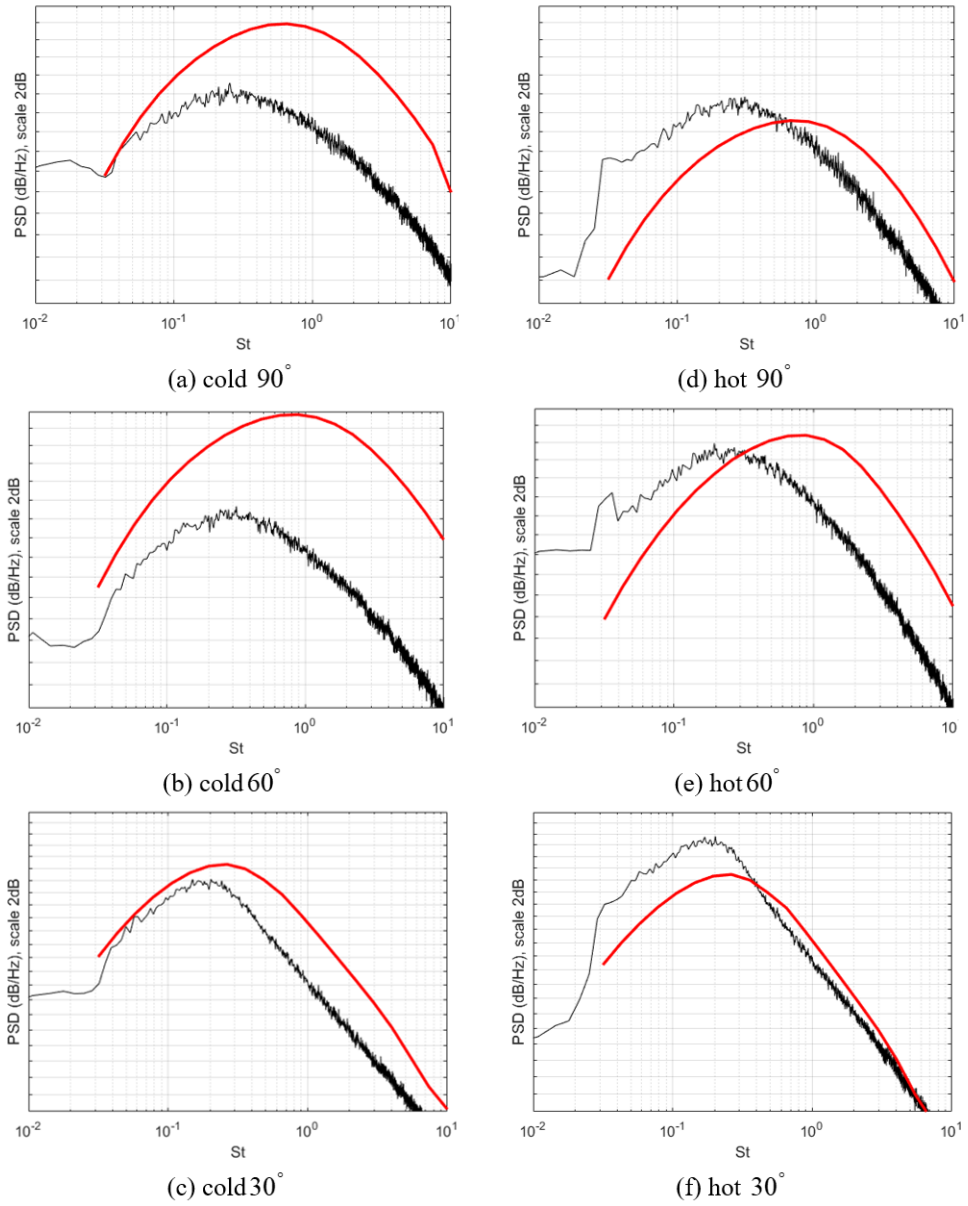

Figure 4.3: Far-field noise spectra predictions of the Tam and Auriaut model for cold (a, b, c) and hot (d, e, f) static SILOET jet for the 90°, 60°and 30°polar angle for the recommended set of calibration parameters from [21].

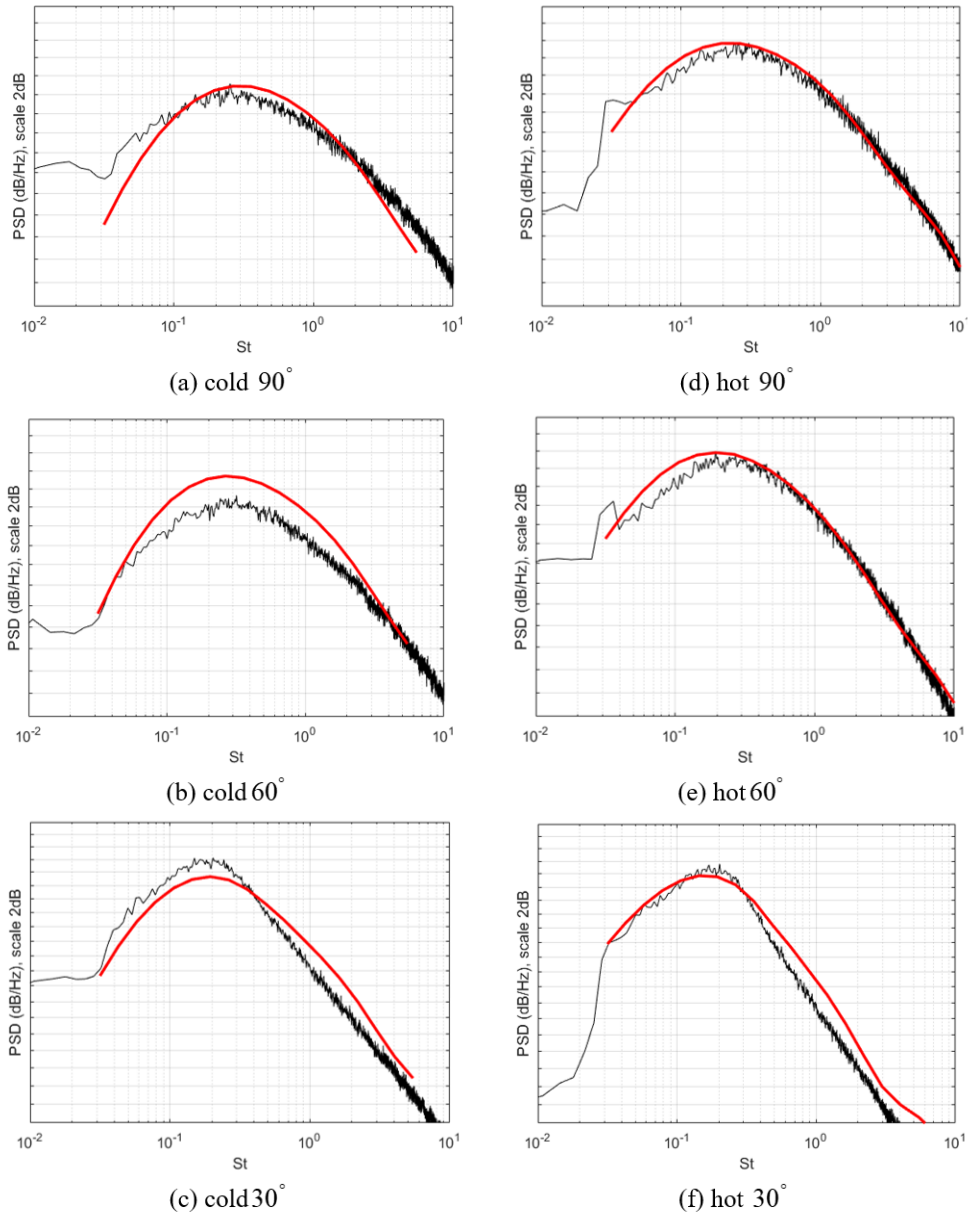

Figure 4.4: Far-field noise spectra predictions of the Khavaran model for the cold (a, b, c) and the hot (d, e, f) static SILOET jet for the 90°, 60°and 30°polar angle to the jet flow and for the best fitted calibration parameters.

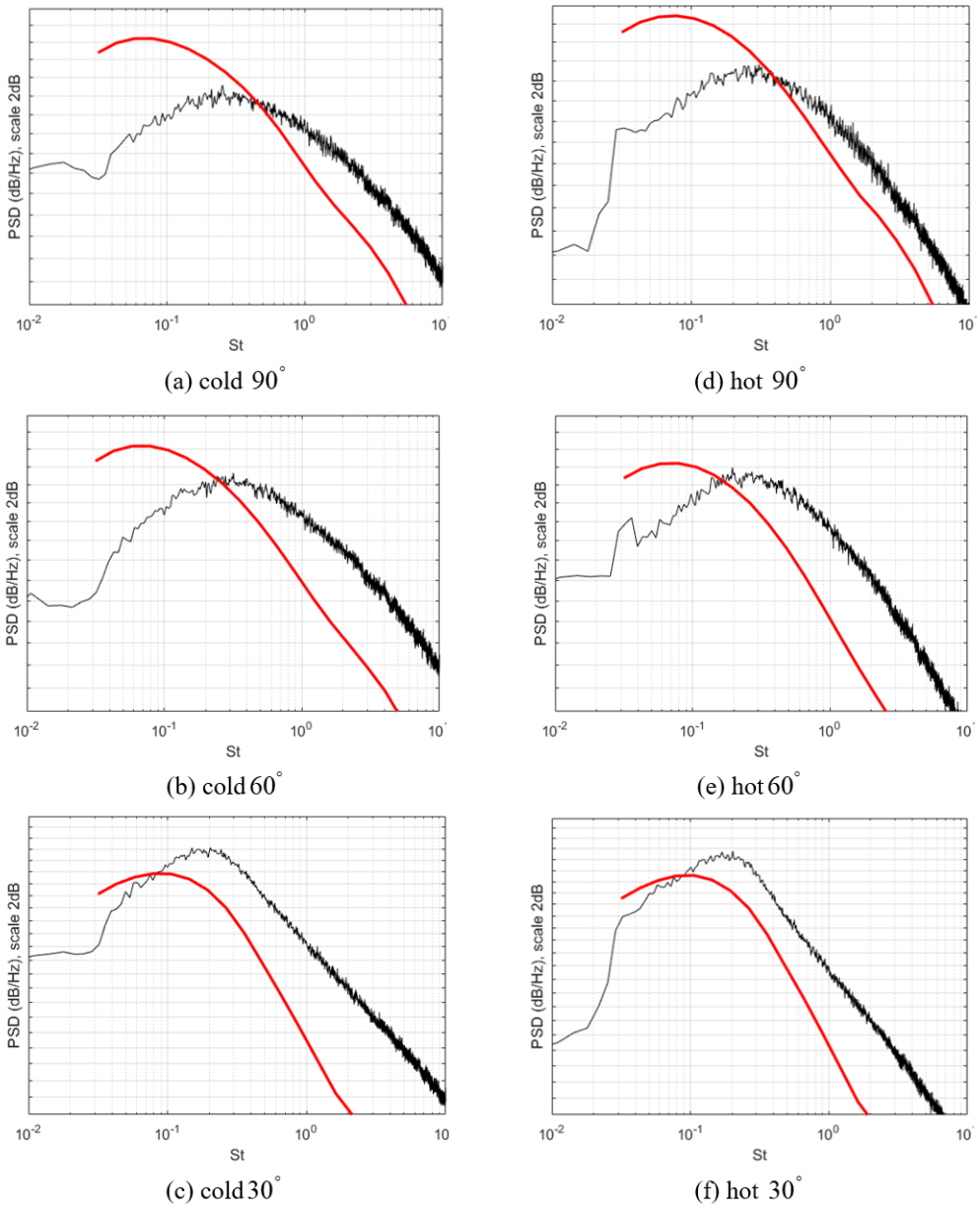

Figure 4.5: Far-field noise spectra predictions of the Khavaran model for cold (a, b, c) and hot (d, e, f) static SILOET jet for the 90°, 60°and 30°polar angle to the jet flow for the recommended set of calibration parameters from [26].

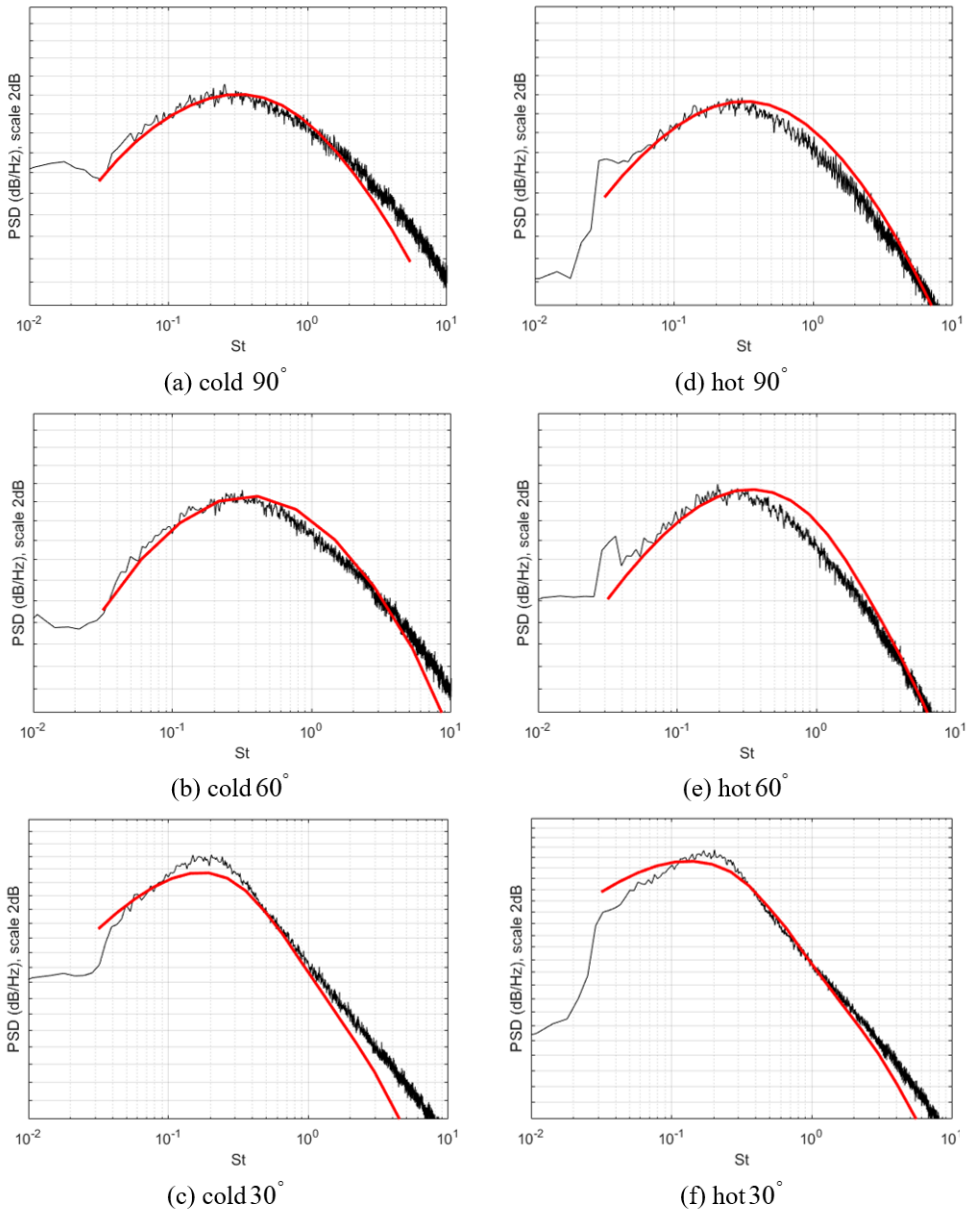

Figure 4.6: Far-field noise spectra predictions of the new implementation of the Goldstein generalised acoustic analohgy model for cold (a, b, c) and hot (d, e, f) static SILOET jet for the 90°, 60°and 30°polar angle.

Summary

Three popular jet noise models have been implemented for conditions of the cold and the heated single-stream SILOET jet noise experiment. The considered models are the Tam and Auriault fine-scale source model [21], the Khavaran model [29] for hot jet noise and the new implementation based on extending the model of Karabasov et al. [5] to heated jets. The last two models are based on the Goldstein generalised acoustic analogy in comparison with Tam and Auriault model which is based on kinetic gas theory.

The fine-scale source model of Tam and Auriault is capable of predicting noise from isothermal and heated jets at large observer angles only and accuracy of the predictions quickly deteriorates for angles away from the the 90° polar angle where the model was calibrated.

The model of Khavaran gives good noise predictions for a wide range of polar angles. However, the model include additional calibration parameters and one of them is based on empirical tuning of the convection velocity that is difficult to justify from physical considerations.

An improved heated jet noise model is developed that is based on extension of the implementation of the Goldstein generalised acoustic analogy developd by Karabasov et al. [5]. The model uses LES to obtain dimensionless source amplitudes thereby limiting the use of calibration parameters based on the far-field. The results of the model are in a good agreement (2dB) with the experimental data for the SILOET jets for a wide range of observer angles and frequencies ($0.04 < St < 2 - 3$). It is shown that the suggested model predictions compare favorably with those of the heated jet noise model by Khavaran, which is also based on the idea of presenting the total noise source as a linear combination of the fluctuating Reynolds stress term and the enthalpy term. In comparison with the Khavaran model, the new jet noise model takes into account the directivity of

major quadrupole and dipole source terms thanks to the use of LES data.

Chapter 5

Coaxial jet noise modelling

5.1 Source modelling for coaxial jet

In this Chapter, the new RANS-based acoustic model of heated jet noise that was presented in Chapter 4 is extended for modelling of co-axial jet noise cases corresponding to conditions of the CoJeN experiment. In addition to addressing the added geometrical and physical complexities, another goal of this Chapter is to develop a co-axial jet noise prediction method based on LES data and keep it completely free from the far-field noise calibration thereby making it distinct from many RANS-based jet noise schemes in the literature. Furthermore, given the expense of LES in comparison with RANS simulations, the concept of using a limited number of LES calculations as a means of providing a solid foundation forrelevant non-dimensionalizations of the acoustic model will be discussed using the idea of the similitude scaling of jet flows.

To remind the reader, the close-form expression for noise spectra predictions that was obtained in Chapter 4 for the suggested heated jet noise model is

$$\hat{P}(\mathbf{x},\omega) = \hat{P}_a + \hat{P}_b, \tag{5.1}$$

which includes the momentum part corresponding to the quadrupole noise typical of cold jets

$$\hat{P}_a = \int_V \frac{R_{ijkl}}{R_{1111}} \frac{R_{1111}}{(2\kappa)^2} \frac{1}{\bar{\rho}^2} \kappa^2(\mathbf{y}) W(\mathbf{y}) \hat{I}_{ij} \hat{I}^*_{kl} d\mathbf{y} \tag{5.2}$$

and the temperature part corresponding to the dipole noise typical of heated jets

$$\hat{P}_b = \int_V \frac{R_{i4j4}}{R_{ij} F_T} \frac{R_{ij}}{\kappa \bar{\rho}} \kappa(\mathbf{y}) W(\mathbf{y}) \hat{I}_{i4} \hat{I}^*_{k4} d\mathbf{y}. \tag{5.3}$$

In comparison with the acoustic models considered in Chapter 4, in the case of a dual-stream jet a set of dimensionless amplitude parameters is obtained for both the bypass/core and the core/ambient shear layers. In addition, the source strengths are split into two components. One of them corresponds to the directivity effect of individual source components and the other corresponds to the source amplitude scaling on the square of the turbulent kinetic energy. Each of these rations is extracted from the LES data of the same CoJeN cases. Details of the LES modelling are provided in [64]. Notably, in comparison with the previous RANS-LES acoustic models, the calibration parameters obtained from LES correspond to averaging over the jet shear layer locations. Details of the averaging procedure are provided in Section 5.2. This leads to the following formula for noise spectra predictions

$$\hat{P}_a \simeq \int_V \left\langle \frac{R_{ijkl}}{R_{1111}} \right\rangle \left\langle \frac{R_{1111}}{(2\kappa)^2} \right\rangle \frac{1}{\bar{\rho}^2} \kappa^2(\mathbf{y}) W(\mathbf{y}) \hat{I}_{ij} \hat{I}^*_{kl} d\mathbf{y} \tag{5.4}$$

and

$$\hat{P}_b \simeq \int_V \frac{\langle R_{i4j4} \rangle}{\langle R_{ij} \rangle \langle F_T \rangle} \frac{\langle R_{ij} \rangle}{\langle \kappa \rangle \bar{\rho}} \kappa(\mathbf{y}) W(\mathbf{y}) \hat{I}_{i4} \hat{I}^*_{k4} d\mathbf{y}, \tag{5.5}$$

where $\langle \ldots \rangle$ represents averaging over each jet shear layer and also some interpolation of the dimensionless source parameters in the radial direction in the case when both the inner and the outer jet shear layers are present. The parameters of the acoustic model for the momentum (quadrupole) source include the relative amplitudes of different quadrupole source components $\langle R_{ijkl}/R_{1111} \rangle$ and the relative

strength of the stream-wise correlation component $\langle R_{1111}/\kappa^2 \rangle$. For the fluctuating enthalpy (dipole) source, the model parameters include the relative strengths of different dipole source components $\langle R_{ij}/R_{11} \rangle$ and the relative strength of the stream-wise velocity autocorrelation component $\langle R_{11}/\kappa \rangle$. The shear layer locations, where the model parameters are evaluated and calibrated on the LES data, correspond to locations of the maximum turbulent velocity fluctuation.

Specifically, the so-called aerodynamic radii of the jet are considered. The aerodynamic radii of the OP1.7 and the OP1.3 jets are determined by the peaks of the root-mean-square axial turbulent velocity profiles, as obtained from the LES solution ad shown in Figure 5.1. In addition to the first peak at $r/D_j = 0.38$ corresponding to the bypass/ambient shear layer location in both the jets, the secondary peak emerges for the dual-stream OP1.3 jet at $r/D_j = 0.18$ as a characteristic mark of the core/bypass shear layer.

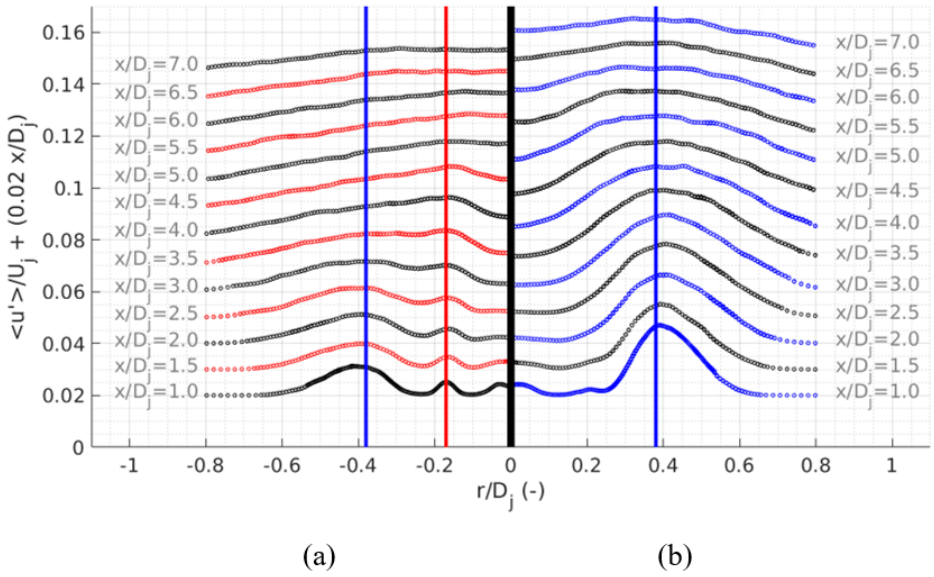

Figure 5.1: Mean velocity fluctuations for several axial locations for OP 1.3 (a) and OP 1.7 (b). The line at +/-0.38 and -0.18 indicate the positions of the bypass and core aerodynamic radii, respectively.

The results computed from the LES solution for the source amplitudes are

first used to examine the accuracy of a few common assumptions made in the current source model following [30]: (i) the correlation between the momentum and the temperature source in comparison with the momentum-momentum and the temperature-temperature terms (5.4), (5.5). (ii) the covariance of the fluctuating enthalpy stress is approximately proportional to a product of the corresponding velocity covariance function and the empirical function (4.24) .

To probe the first assumption, the acoustic integrand $\hat{R}_{2424}(\mathbf{y},0,\omega)\hat{I}_{24}\hat{I}^*_{24}(\mathbf{y},\omega;\mathbf{x})$ corresponding to the source strength in (5.5) is compared with the amplitudes of the fluctuating Reynolds stress- enthalpy sources, $\hat{R}_{1114}(\mathbf{y},0,\omega)\hat{I}_{11}\hat{I}^*_{14}(\mathbf{y},\omega;\mathbf{x})$, $\hat{R}_{2224}(\mathbf{y},0,\omega)\hat{I}_{22}\hat{I}^*_{24}(\mathbf{y},\omega;\mathbf{x})$ and $\hat{R}_{3334}(\mathbf{y},0,\omega)\hat{I}_{33}\hat{I}^*_{34}(\mathbf{y},\omega;\mathbf{x})$ which were neglected in the current implementation. For simplicity of the comparison of different source terms which must involve different Green's function propagator terms, the observer position is fixed at 90° to the jet flow. Figure 5.2 shows the results for the OP1.3 jet in the core and the bypass shear layers for 2 typical sound frequencies ($St_D = 0.2$ and 2), where the Strouhal number is based on the bypass jet parameters. It can be noted that the effect of the asymmetric source terms responsible for the velocity/temperature interaction noise is negligible in comparison with the auto-covariance of the fluctuating enthalpy stress $\hat{R}_{2424}(\mathbf{y},0,\omega)$.

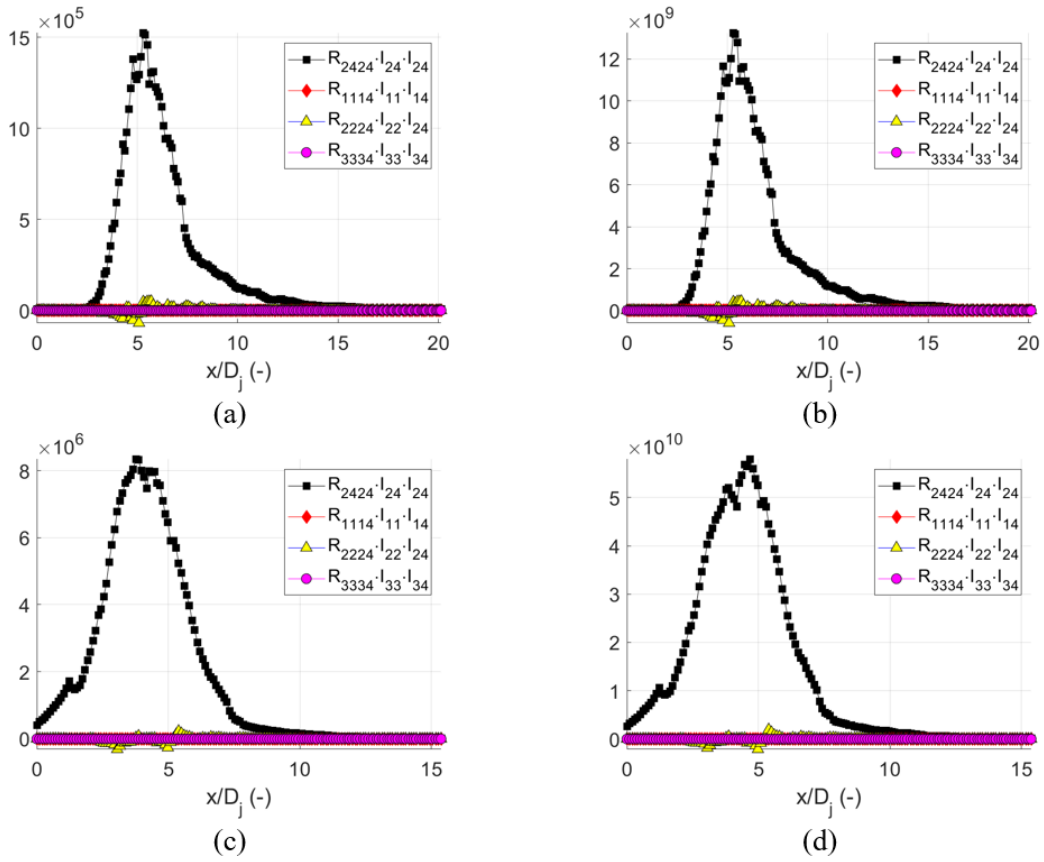

Figure 5.2: Comparison of the effect of the pure fluctuating enthalpy source against the fluctuating enthalpy/velocity source for the OP1.3 jet case: in the bypass shear layer (a, b) and the core shear layer (c,d) at observer angle 90° and sound frequencies $St_D = 0.2$(a, c), $St_D = 2$(b, d).

To examine the accuracy of the second assumption, the amplitudes of the major noise source terms in the heated jet, R_{i4j4} for all three velocity components $i = 1, 2, 3$ are averaged along the core/bypass aerodynamic radius over the jet locations $2 < x/D_j < 12$. The selected source components and their location correspond to the peak fluctuating enthalpy noise that includes the velocity component in the stream-wise direction. The computed values of the auto-covariance of the fluctuating enthalpy stress are divided by the product of the corresponding velocity autocorrelation amplitudes and the empirical function from which are av-

eraged over the same jet locations, $\frac{\langle R_{i4j4}\rangle}{\langle R_{ij}\rangle\langle F_T\rangle}$ and the results obtained for different velocity components are summarized in Table (5.1).

i	1	2	3
$\frac{\langle R_{i4j4}\rangle}{\langle R_{ij}\rangle\langle F_T\rangle}$	2.96	2.83	2.32

Table 5.1: Proportionality between the auto-covariance of the fluctuating enthalpy stress and the velocity autocorrelation function

It can be noted, that the proportionality coefficient is reasonably constant within a 20% error. To sum up, the neglect of the correlation between the momentum and the temperature sources and the assumption about the linear scaling of the fluctuating enthalpy source with the auto-correlation velocity function appear to be reasonable in consistence with the reference LES solution for the heated CoJeN jet flow. Both the above assumptions were previously used in the literature [29], [30] but in accordance with the author's knowledge, the current work is first where the validity of both these assumptions is rigorously accessed using the high-fidelity jet flow data as discussed in [67]. Having validated the heated jet noise model assumptions, amplitudes of the major quadrupole R_{ijkl} and dipole R_{ij} terms are computed along the bypass/ambient and the core/bypass (excluding OP1.7) aerodynamic radii locations of the jets. As before, $i, j, k = 1, 2, 3$ denote the velocity components where 1 is in the jet flow direction, 2 is radial, and 3 is azimuthal.

5.2 Correlation amplitudes extraction from LES data

Results for the cold single-stream like OP1.7 jet are considered first. Figure (5.3) shows distributions of 6 major amplitudes of the quadrupole sources along the external (bypass/ambient) aerodynamic radius as normalized by the peak amplitude

of R_{1111}. For the use in the reduced-order acoustic model, the relative strengths, $\langle R_{ijkl}/R_{1111}\rangle$are averaged over the axial coordinate and the resulting dimensionless correlation coefficients are summarized in Table (5.2) It can be seen that for the selected averaging interval, $2 < x/D_j < 12$ the dimensionless correlation amplitudes are relatively insensitive to the averaging interval.

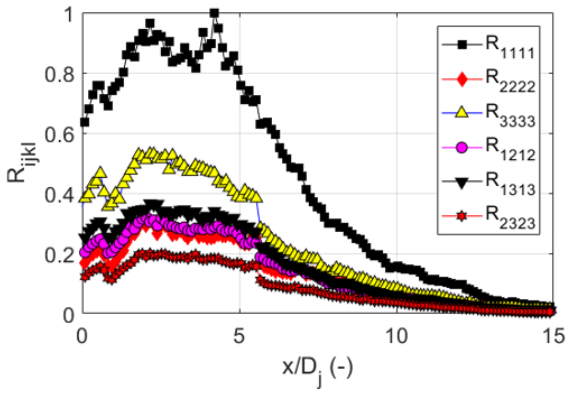

Figure 5.3: Quadrupole source amplitudes for the OP1.7 jet along the core/bypass aerodynamic radius

$ij, kl/$ averaging interval	22,22	33,33	12,12; 12,21 21,12; 21,21	13,13; 13,31; 31,13; 31,31	23,23; 23,32; 32,23; 32,32
(2, 10) D_j	0.323	0.500	0.322	0.364	0.202
(2, 12) D_j	0.336	0.493	0.323	0.365	0.203

Table 5.2: Relative correlation amplitudes of the quadrupole sources along the bypass/ambient shear layer of the OP1.7 jet

Next, heated-core OP1.3 jet is considered to extract source amplitudes. Figures (5.4) and (5.5) present results for OP1.3 jet for the quadrupole and dipole source amplitudes, respectively. Each figure shows the correlation component distributions along the external and the internal aerodynamic radius of this dual-stream jet flow.

The quadrupole sources correspond to the same 6 major correlation components as for the OP1.7 jet. Interestingly, these are the same major correlation

amplitudes which were found important in the previous studies of single-stream axi-symmetric jets [5]. For the dipole source components as shown in Figure (5.5), only the three diagonal terms, R_{ii} are important, which correspond to the auto-covariance of the fluctuating enthalpy stresses, R_{i4j4}.

Similar to the OP1.7 jet, for each jet location and source type, the relative strengths, $\langle R_{ijkl}/R_{1111}\rangle$and $\langle R_{ij}/R_{11}\rangle$ are averaged over the axial coordinate and the resulting dimensionless correlation coefficients. The results are summarized in Tables (5.3), (5.4) for the quadrupole source amplitudes and in Tables (5.5), (5.6) for the dipole sources. Again, it can be noted that for the selected averaging interval, $2 < x/D_j < 12$ the dimensionless correlation amplitudes are relatively insensitive to the averaging interval.

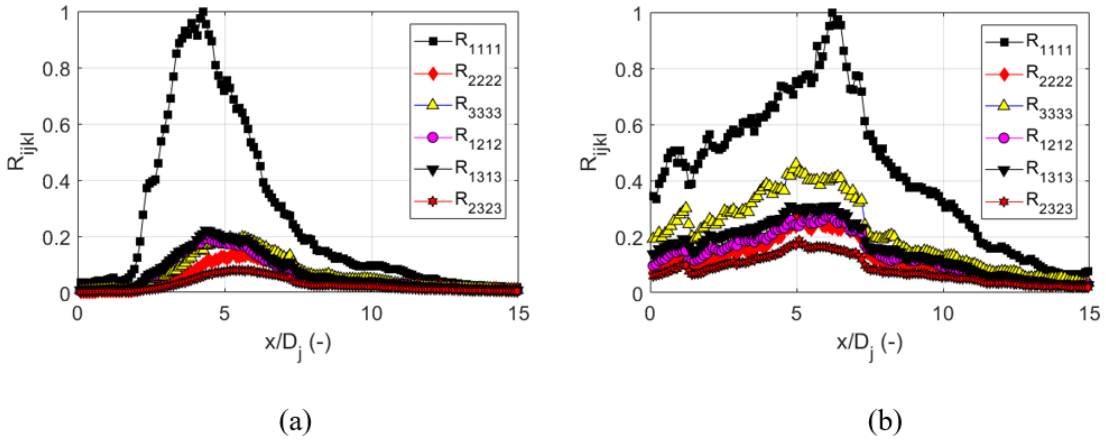

Figure 5.4: Quadrupole source amplitudes for the OP1.3 jet along the core/bypass (a) and the bypass/ambient (b) aerodynamic radius

$ij, kl/$ averaging interval	22,22	33,33	12,12; 12,21 21,12; 21,21	13,13; 13,31; 31,13; 31,31	23,23; 23,32; 32,23; 32,32
(2, 10) D_j	0.220	0.303	0.255	0.290	0.127
(2, 12) D_j	0.257	0.328	0.276	0.308	0.143

Table 5.3: Relative correlation amplitudes of the quadrupole sources along the core/bypass shear layer of the OP1.3 jet

$ij, kl/$ averaging interval	22,22	33,33	12,12; 12,21 21,12; 21,21	13,13; 13,31; 31,13; 31,31	23,23; 23,32; 32,23; 32,32
(2, 10) D_j	0.268	0.468	0.301	0.352	0.182
(2, 12) D_j	0.285	0.468	0.305	0.352	0.186

Table 5.4: Relative correlation amplitudes of the quadrupole sources along the bypass/ambient shear layer of the OP1.3 jet

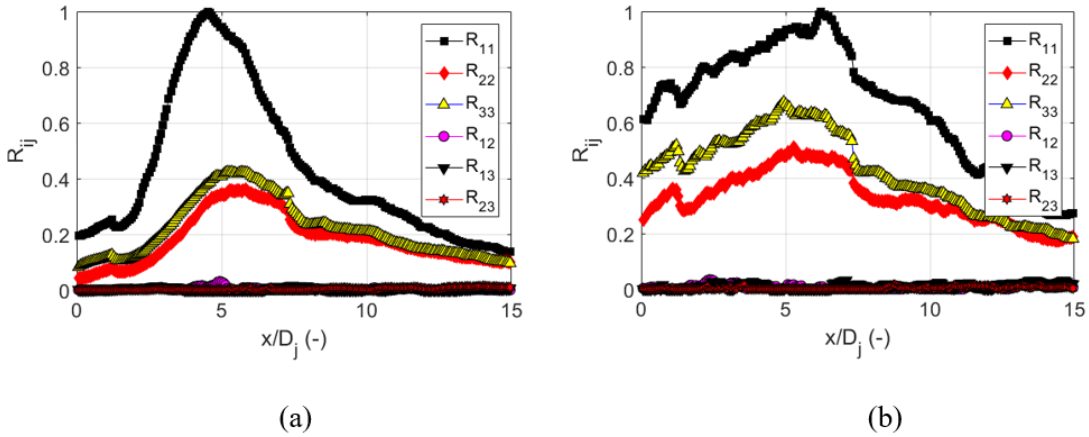

Figure 5.5: Dipole source amplitudes for the OP1.3 jet along the core/bypass (a) and the bypass/ambient (b) aerodynamic radius

$ij/$ averaging interval	22	33	12,	13	23
(2, 10) D_j	0.415	0.499	0	0.002	0.002
(2, 12) D_j	0.450	0.524	0.002	0.006	0.007

Table 5.5: Relative correlation amplitudes of the dipole sources along the core/bypass shear layer of the OP1.3 jet

ij/ averaging interval	22	33	12,	13	23
(2, 10) D_j	0.481	0.627	0.001	0.010	0.005
(2, 12) D_j	0.495	0.624	0	0.013	0

Table 5.6: Relative correlation amplitudes of the dipole sources along the bypass/ambient shear layer of the OP1.3 jet

To conclude the non-dimensionalization of the correlation amplitudes, the relative amplitudes of the stream-wise correlation components scaled on the average turbulent kinetic energy, $\langle R_{1111}/\kappa^2\rangle$and $\langle R_{11}/\kappa\rangle$ are calculated for the OP1.7 and OP1.3 jets. The computed values, which correspond to the external shear layer and the end of the potential core location of each jet, are summarized in Table 5.7

OP1.7, $\langle R_{1111}/\kappa^2\rangle$	$\langle R_{1111}/\kappa^2\rangle$	$\langle R_{11}/\kappa\rangle$
0.779	1.14	0.82

Table 5.7: Relative quadrupole and dipole source strengths scaled by the turbulent kinetic energy

5.3 Jet flow similarity

As discussed in the previous section, the acoustic source amplitudes can be non-dimensionalized reasonably well by the turbulent kinetic energy. Moreover, the amplitude effect can be separated from the acoustic integrand by using some averaging over the jet volume. In comparison with the source amplitudes, the correlation time ,(τ_s) and length, (l_s) scales vary rapidly in the jet volume and cannot be easily decoupled from other terms of the integral including the propagation effects.

Additionally, the acoustic correlation scales are significantly different from the standard turbulence time and space scales, which can be defined from the average

turbulent kinetic energy and the turbulence dissipation rate. Furthermore, direct evaluation of the correlation scales from LES in each point of the jet shear layers is very expensive due to complexity of the covariance function of fluctuating turbulent stresses R_{ijkl} and can lead to significant errors in the jet locations corresponding to small turbulent intensity where the signal to statistical noise ratio is small [56]. Besides, an intensive use of the high-fidelity tool such as LES for calibration of a low-order model would defeat the purpose of the low-order model as of a fast design method that provides rapid predictions of jet noise for a class of flows which share some similarity. Hence, in comparison with the previous hybrid RANS/LES implementations of the Goldstein generalized acoustic analogy model [5], which attempt to extract the length scales from LES in a set of control points and use a simple interpolation in the rest of the jet using the RANS solution, the evaluation of acoustic length scales in the current work is based on a different approach.

Specifically, following [68], [31], the current approach is to exploit the similitude of jet flows in order to develop an improved non-dimensionalization of the jet noise sources. To proceed with the analysis, it should be noted that jets of different flow conditions do not have the same flow features such as meanflow velocity or fluctuations at the same absolute location from the nozzle exit even when normalized by the perfectly expanded jet velocity and jet diameter. One of the main drivers in flow physics is the length of the potential core, followed by the jet spread [70].

Following the work of Bridges [31], the two-parameter functional form is used to collapse the centerline velocity distribution of CoJeN jet flows:

$$\frac{U}{U_j} = 1 - \exp\left\{\frac{2\alpha}{1 - \frac{x}{\beta D_j}}\right\} \tag{5.6}$$

where α and β stand for case-dependent dimensionless parameters for jet spreading rate and potential core length. Because of the wake of the central body, the fit needs to be adapted. The decay rate of the centerline velocity is fitted to

the similitude form after the wake effect is sufficiently mixed out.

The LES solutions of the original centreline meanflow velocity profiles of the 6 CoJeN jet flows from exhibit a notable variation depending on the jet core velocity and temperature as shown on Figure 5.6a. However, once the similitude shape parameters are obtained for each jet, their centerline meanflow velocity profiles collapses as a function of the dimensionless coordinate (see Figure 5.6b)

$$\left(\frac{x}{D_j} - \beta\right) / (\alpha\beta). \tag{5.7}$$

When the same non-dimensionalzation is applied for the centerline distributions of the turbulent kinetic energy from the same dataset of the CoJeN LES solutions (Figure 5.6c), the different turbulent kinetic energy profiles show a reasonable collapse (Figure 5.6d). Although it can be noted that the collapse of the turbulent kinetic energy profiles is not as perfect as the collapse of the meanflow velocities.

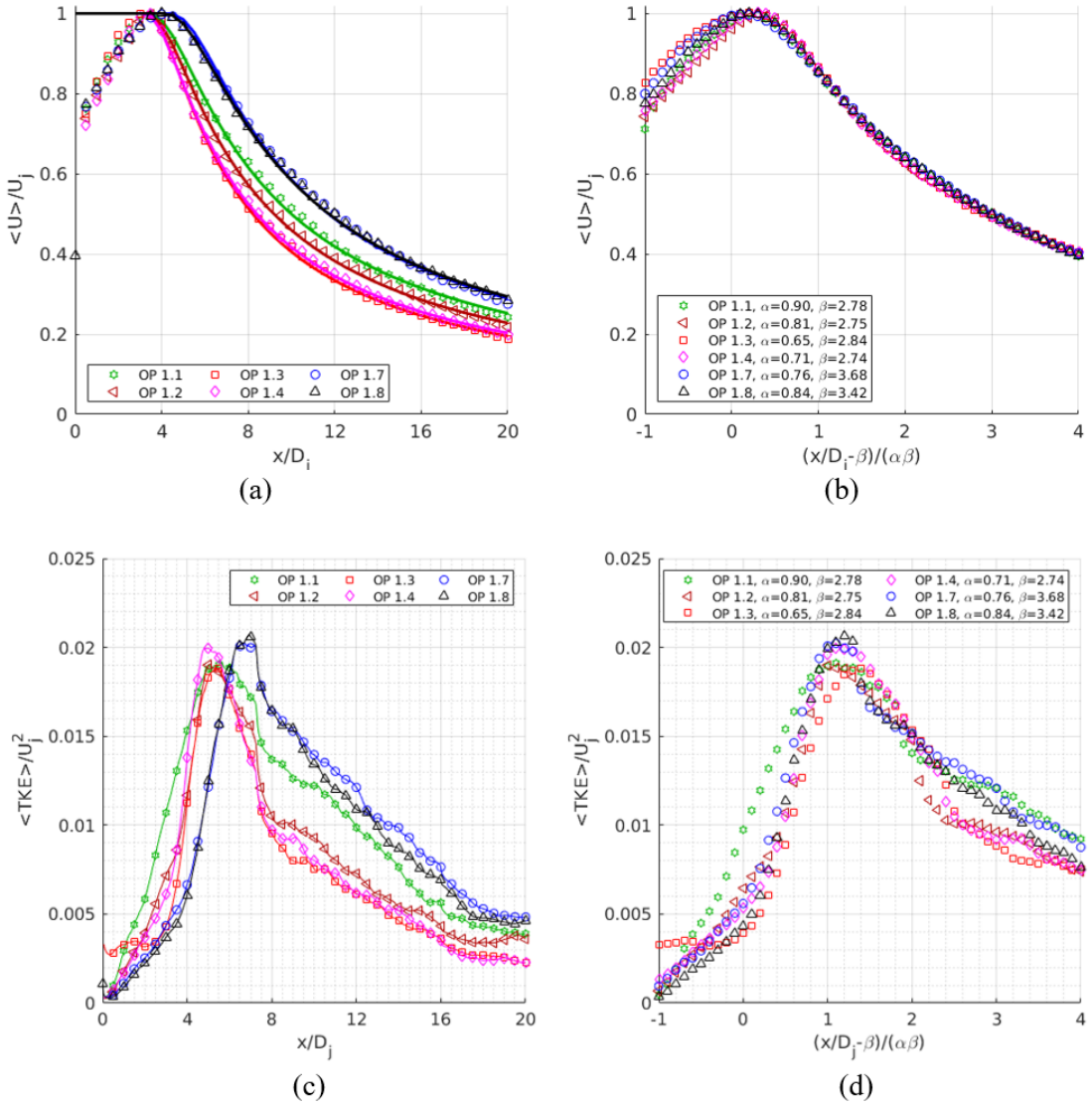

Figure 5.6: Using a two-parameter similitude fit function to collapse the centerline distributions of the CoJeN jets corresponding to the LES solutions of: meanflow velocity (a),(b) and time-averaged turbulent kinetic energy (c),(d).

5.3.1 Non-dimensionalization of correlation length and time scales

The same idea of jet flow similarity can be applied in order to non-dimensionalize the correlation time and space length scales where, in addition to the parameters

of the jet spreading rate and the potential core length, α and β, the bypass nozzle diameter, D_j, the core stream velocity, U_j and the eddy convection velocity, U_c are used in the non-dimensionalization.

For example, Figure 5.7 compares the distribution of the stream-wise correlation space, L_η, where $\eta = (\eta_1, 0, 0)$and time length scales, L_τ, of the different CoJeN jets along the external aerodynamic radius. The space and the time scales shown in the figure correspond to the steam-wise correlation component,R_{1111}. It should be noted that in the LES data the correlation space and time scales, L_η and L_τ, are non-dimensionalized by the bypass nozzle diameter and the eddy convection velocity.

To compare the acoustic scales from different CoJeN jets, the potential core length and the decay rate parameters, β and α, as well as the convection velocity, $U_c$and the jet core stream velocity are further used in the non-dimensionalization.

Following the non-dimensionalization, the acoustic scales of all the CoJeN jets are reasonably well approximated by a linear fit function $a + b\bar{x}$ where $\bar{x} = \left(\frac{x}{D_j} - \beta\right)/(\alpha\beta)$ for a range of acoustically important locations along the external aerodynamic radius. The goodness of a linear approximation suggests that the acoustic length scale of the jet flow grows linearly following the external shear layer development.

Furthermore, it can be noted that the linear fit function has a similar positive slope parameter, b across the different CoJeN jet cases. In comparison with this, the free constant of the linear function, a shows more variation between the different jet cases. Possibly, this variation could be associated with the accuracy of obtaining the similitude shape parameters, β and α in each CoJeN jet case.

The liner fit functions which correspond to the dimensionless parameters extracted from the Particle Image Velocimetry (PIV) data corresponding to the cold single-stream jet flows at SP (Set Point) 3 and 7 operational conditions from the NASA SHJAR database [69] are shown on the same plots for reference. The agree-

ment between the dimensionless acoustic scales of the various CoJeN jets and those of the NASA data is also reasonable.

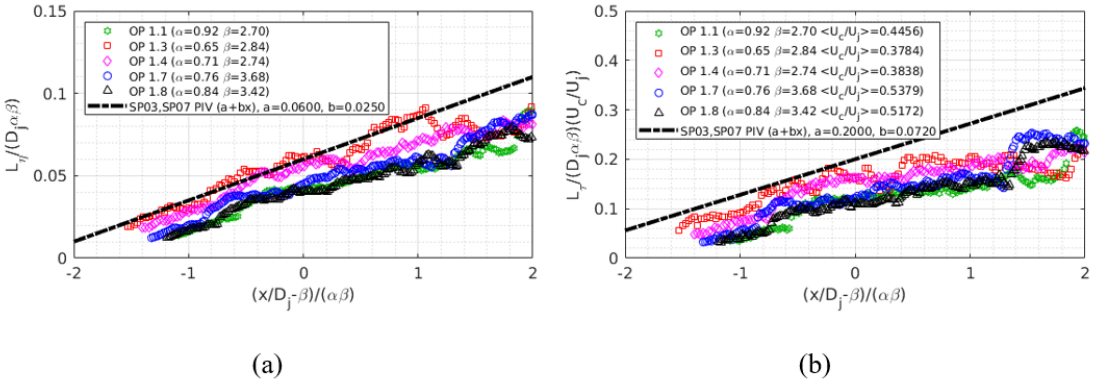

(a) (b)

Figure 5.7: The normalized space (a) and time (b) scales extracted from the correlations R_{1111} for the bypass aerodynamic radius obtained from LES for the 6 CoJeN jet cases.

In comparison with the external shear layers, the evolution of the acoustic scales inside the dual-stream jet is much more complex. This is illustrated in Figure 5.8 which compares the distribution of dimensionless correlation space and time scale along the external and the internal aerodynamic radius of the OP1.3 jet case. The same non-dimensionalization is used as in Figure 5.7. In contrast with the external shear layers, the development of the space and time correlation length scale is non-monotonic in accordance with the three distinct zones in dual-stream jet flows: the initial flow region, the interaction region, and the mixed flow region [71]. The non-monotonicity of the acoustic scales reflects the transition from the initial jet region to the onset of the interaction region at $\frac{x}{D_j} - \beta \approx -0.4\alpha\beta$ and the transition from the interaction region to the mixed flow region at $\frac{x}{D_j} = \beta$. At each of these three jet regions, the evolution of acoustic scales can still be approximated by a linear fit function, but parameters of the fit function are quite different, which corresponds to the growth or decay of the acoustic length scale, as relevant for the jet flow physics there.

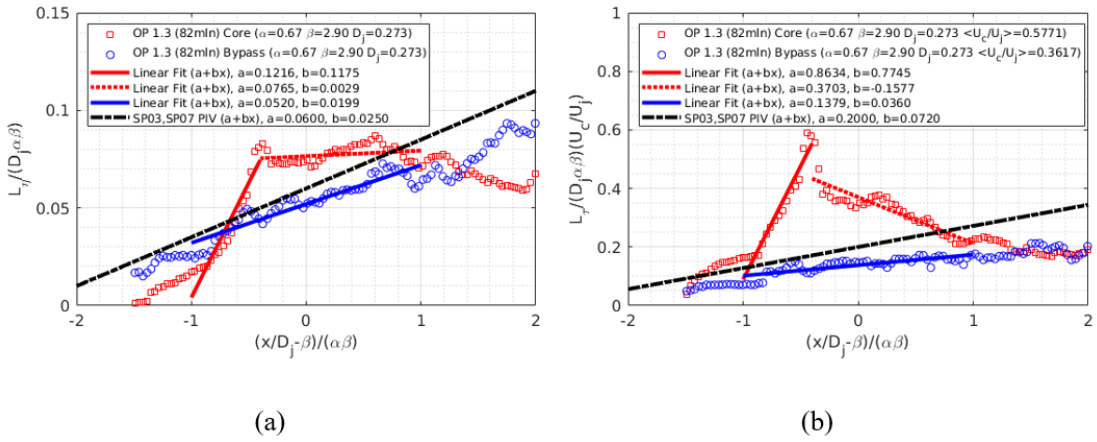

Figure 5.8: The normalized space (a) and time (b) scales extracted from the correlations R_{1111} for both the core and bypass aerodynamic radius both obtained from LES for the OP1.3 CoJeN jet

5.3.2 Non-dimensionalization of correlation amplitudes

Getting back to the discussion on the jet similarity along the external aerodynamic radii, Figure 5.9 compares the distribution of relative amplitudes of several major correlation components, $R_{ijkl}\left(\mathbf{y};\eta=0,\tau=0\right)$of all 6 CoJeN cases.

The non-dimensionalization is performed based on the mean turbulent kinetic energy in Figure 5.9 (top left) and using the largest correlation amplitude corresponding to the stream-wise propagation direction, $R_{1111}\left(\mathbf{y};\eta=0,\tau=0\right)$ in the rest of Fig 5.9a. It can be noted that the ratio of R_{1111} to the turbulent kinetic energy $\kappa=\left(\left\langle v_1'\right\rangle^2+\left\langle v_2'\right\rangle^2+\left\langle v_3'\right\rangle^2\right)/2$ inside the jet approximately stays constant within the range of 1.1–1.4 for all the jet flows. This range of values is in agreement with the usual assumptions about the relative amplitudes of turbulent velocity fluctuations in high-speed axi-symmetric jet flows $\left\langle v_1'\right\rangle\approx 1.5\left\langle v_2'\right\rangle\approx 1.5\left\langle v_3'\right\rangle$ that leads to the estimate of R_{1111}/κ^2.

The fluctuating enthalpy amplitudes are shown in fig.5.9b, which shows datasets corresponding OP1.2,1.3,14,1.7 and 1.8. All amplitudes are normalized by the local value of R_{1414} which corresponds to the biggest amplitude. The OP1.1

dataset follows the same trends as the other 5 CoJeN jets but has the biggest scatter, hence, was excluded from the figures.

Despite the bigger scatter in the fluctuating enthalpy amplitudes in comparison with the fluctuating Reynolds stresses, it can be noted that the auto-covariance terms R_{2424} and R_{3434} correspond to two families of datasets which oscillate about the values of 0.4 and 0.6. respectively. The values of the asymmetric source terms fluctuate about the zero level, which suggest that their statistical importance could be small in comparison with the auto-covariance terms.

For all CoJeN cases considered, the non-negligible relative source amplitudes normalized by the R_{1111} component collapse to the 6 distinct families corresponding to different noise directivities: R_{2222}, R_{3333}, R_{1212}, R_{1313}, R_{1133}, and R_{1122}. It can be noted that asymmetric terms such as R_{1133} and R_{1122} are small. The relative values show a small variation around the mean values from case to case and with the position along the external aerodynamic radius. For comparison with the relative amplitude values which have been computed for the OP1.7 and OP1.3 jets (Tables 5.2 and 5.3), the mean values across all 6 CoJeN cases are summarized in Table 5.8.

Interestingly, the relative source amplitudes shown in the Table 5.8 are the same dominant source components that were considered in the previous models of cold single-stream jets based on the Goldstein generalized acoustic analogy [5]. One notable difference in comparison with the single-stream jet models is that the relative source strengths of diagonal terms, R_{2222}, R_{3333} of the CoJeN jet flows appear to be amplified by a factor 2–3.

R_{2222}/R_{1111}	R_{3333}/R_{1111}	R_{1212}/R_{1111}	R_{1313}/R_{1111}	R_{2323}/R_{1111}	R_{1122}/R_{1111}
0.3	0.5	0.3	0.35	0.2	0.1

Table 5.8: Mean values of the relative correlation amplitudes of the quadrupole sources in the bypass/ambient shear layer among 6 CoJeN cases

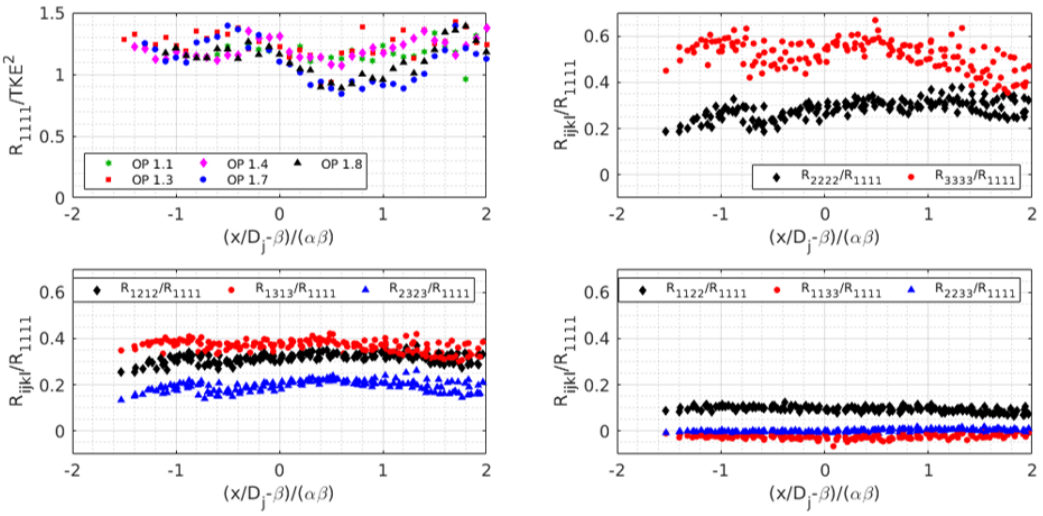

(a)

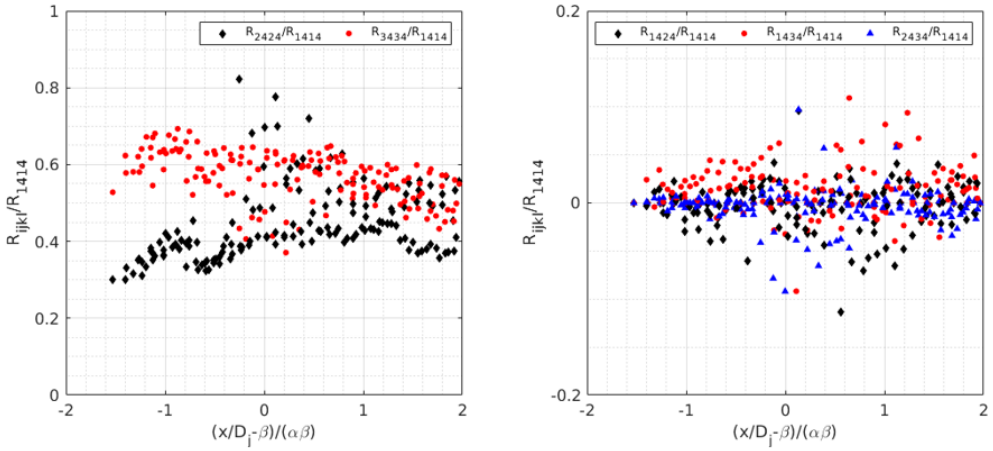

(b)

Figure 5.9: Amplitudes of the effective sounds sources in accordance with the generalised acoustic analogy: R_{1111} component normalized by the turbulent kinetic energy (top-left) and different R_{ijkl}components obtained from LES for the 6 CoJeN jet cases (a) and the covariances of the fluctuating enthalpy stresses normalised by R_{1414} for all CoJeN cases except OP1.1(b).

5.4 Acoustic Length scale modeling based on RANS and LES

To proceed with the low-order modeling, the same similitude scaling analysis should now be performed for the RANS solutions of the same CoJeN jets. As discussed in Chapter 2, while capturing the potential core length of the jet reasonably well, the RANS solutions do not capture the effect of the wake behind the central body. This result in some differences between the similitude function from RANS and the LES solutions as demonstrated in Figure 5.10 for the case of the OP1.7 jet meanflow velocity. Furthermore, it can be seen that, because of the central body effect, the best fit parameters are not uniquely defined even for the LES flow, which can also explain the imperfect collapse of the turbulent kinetic energy and correlation scale profiles of the LES of different CoJeN jet flows in Figures 5.6 and 5.7.

For the potential core length parameter, β, the best fit to the RANS solution is consistent with the LES within the scatter of the fit function values. It can be noted that capturing the correct potential core length of the jet is very important since geometrical parameters in the jet mixing layers, which are crucial for jet noise, scale with this length. In comparison with β, the spreading rate, α predicted by the RANS solution is significantly outside the variation of the fit function to the LES solution. Hence, for most jet cases considered in the current study, it is found that a good choice of the non-dimensionalization parameters is based on adopting the potential core length parameter, β from the RANS solution and the spreading rate, α is taken from the LES.

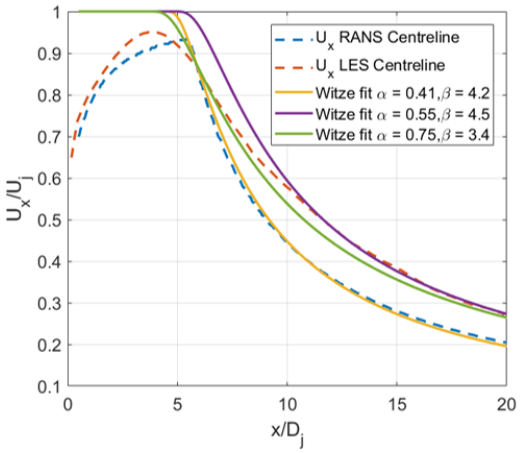

Figure 5.10: Similitude functions based on the LES and the RANS solutions: using a two-parameter similitude fit function to collapse the centerline distributions of the OP1.7 CoJeN jets.

Once the similitude parameters of the jet are determined, the acoustic correlation scales in the jet can be fully defined from the similitude fit function $a + b\overline{x}$ at each axial coordinate $\overline{x} = \left(\frac{x}{D_j} - \beta\right)/(\alpha\beta)$ of the jet shear layers. This provides a new way of evaluation of the dimensionless length scales for the RANS-based acoustic model in accordance with the following algorithm:

- define the acoustic time and space correlation lengthscales using the turbulent scales obtained from the RANS solution, $\tau_s = c_\tau \kappa/\varepsilon$ and $l_s = c_l \kappa^{3/2}/\varepsilon$, where are $c_\tau$and c_l are the unknown parameters to be determined

- non-dimensionalize the acoustic scales using

$$L_\tau = c_\tau u_x \frac{\kappa/\varepsilon}{D_j}/(\alpha\beta)$$

and

$$L_\eta = c_l \frac{\kappa^{3/2}/\varepsilon}{D_j}/(\alpha\beta)$$

for the time and the space lengthscales, respectively,

- consider the linear fit functions $a + b\overline{x}$ corresponding to the largest jet noise source term R_{1111} in the jet shear layers
- obtain the parameters c_τ and c_l by matching the dimensionless correlation scales L_τ and L_η to the time and space linear fit functions $a+b\bar{x}$, respectively, at the end of the jet potential core location, where $\frac{x}{D_j} = \beta$
- apply the same algorithm for different jets as well as different (core/bypass and bypass/ambient) shear layer locations of dual-stream jets using the appropriate local RANS fields in each case.

Figure 5.11 demonstrates the process of determining the dimensionless acoustic scales in the bypass/ambient shear layer of the OP1.7 jet. The same process for the same jet is illustrated in Figure 5.12a and b for the core/bypass shear layer. Figure 5.12c and d show the results for the OP1.3 jet case, which include the scales in both the bypass/ambient shear layer and the core/bypass shear layer.

The correlation scales inside the jet and outside the jet, especially along the internal and the external shear layers of a dual-stream jet, do not share the same behavior. However, the differences in the scale behaviors are captured by the corresponding linear fit functions in each case. For example, these differences can be accounted for in the definition of the dimensionless time and space scale parameters, c_τ and c_l in the primary and the secondary shear layers of the OP1.3 jet. For the acoustic model of the dual-stream jet, c_τ and c_l can be approximated by a continuous functions which is equal to the core/bypass parameters inside the jet core, the bypass/ambient parameters outside the jet, and an interpolated value in between the two shear layers (see Figure 5.13).

Interestingly, the acoustic lengthscale parameters in the bypass/ambient shear of the OP1.7 and the OP1.3 jet are the same ($c_\tau = 0.233$, $c_l = 0.256$) as the empirical best fit parameters suggested by Tam and Auriault [21], who evaluated these parameters from an extensive calibration of their fine-scale jet noise model

with respect to a large database of single-stream jet noise measurements.

Besides the correlation scales, the relative source amplitudes of the OP1.3 jet along the core/bypass and the bypass/ambient shear layers are also significantly different (see Tables 5.3, 5.4 and 5.5, 5.6). Therefore, a similar interpolation procedure is used to obtain the correlation amplitudes inside the jet similar to the correlation scales.

It can be noted that in comparison with the previous RANS-based jet noise models informed by LES [5], [57], the current approach for computing the acoustic scales avoids the local point-to-point interpolations from LES to RANS flow solutions. Instead, the LES-to-RANS interpolation of the suggested approach focuses on common patterns of the jet flows. These patterns are related to the similitude of jet flows, which effectively includes an averaging over the jet shear layer locations. Furthermore, the new approach can also include averaging over several jet flows of the same class, thus, reducing the need for additional LES runs.

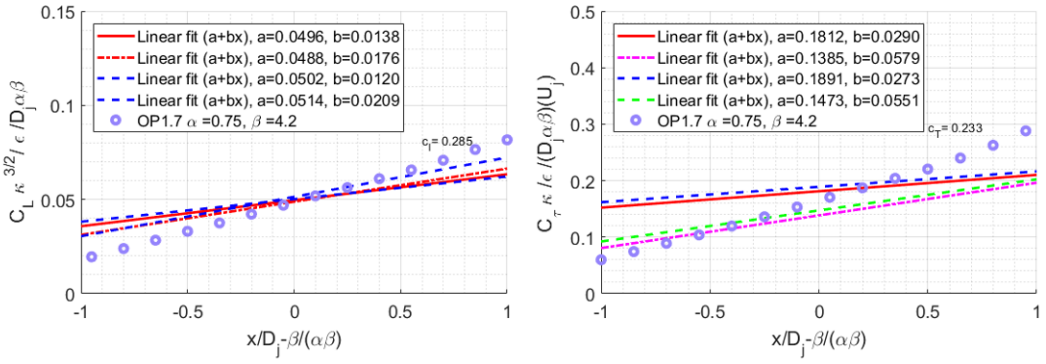

Figure 5.11: Evaluation of the dimensionless acoustic correlation scales in the shear layer of the OP1.7 jet for space (a) and time (b) lengthscales. .

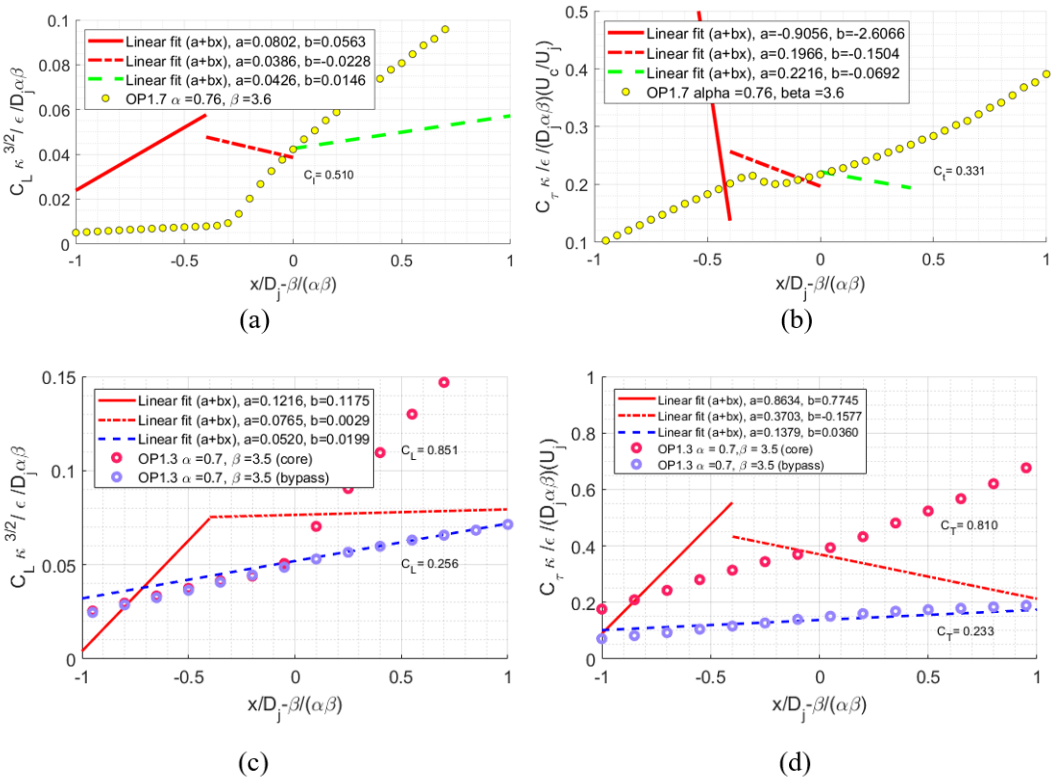

Figure 5.12: Evaluation of the dimensionless acoustic correlation scales of the OP1.7 jet in the core for space (a) and time (b) lengthscales and in the core/bypass (core) as well as in the core/bypass (bypass) shear layers of the OP1.3 jet for space (c) and time (d) lengthscales.

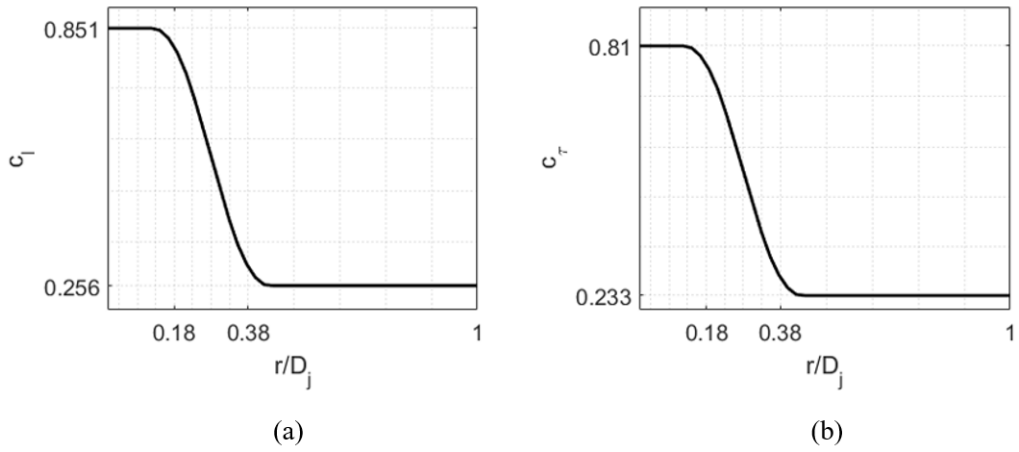

Figure 5.13: Reconstruction of continuous acoustic space (a) and time (b) lengthscale parameters in the two-stream OP1.3 jet.

5.5 Validation of the coaxial jet noise model

Developed jet nose prediction model for coaxial jet noise prediction is compared to the experimental measurements in this section.

Figuress. 5.14 and 5.15 compare the results of the suggested acoustic model for the OP1.7 and the OP1.3 CoJeN jets, respectively. In the case of the cold single-stream OP1.7 jet, the model only involves the quadrupole source (5.2) and the dimensionless correlation amplitudes and the length scales are evaluated in the bypass/ambient shear layer.

In the case of the heated-core OP1.3 jet, the model includes both the quadrupole and the dipole source terms as well as the dimensionless source parameters along the two shear layers. It can be noted that the noise spectra prediction of the OP1.7 jet (Figures 5.14) are within 1-2dB from the experiment for observer angles 30° – 90° to the jet flow and frequencies $0.1 < St_D < 5$, where the Strouhal number is defined on the bypass nozzle diameter and the bypass stream velocity. Interestingly, for the 30o polar angle, the noise spectra are captured within 1dB.

For the OP1.3 jet (see Figure 5.15), the model predictions are within 2-3dB

from the experiment for observer angles 30° – 90° to the jet flow and frequencies $0.03 - 0.04 < St_D < 3 - 4$. Furthermore, it can be noted that the peak noise frequencies of the OP1.3 jets are correctly captured for all observer angles and the accuracy of predicting the peak noise levels is 2dB.

The noise spectra predictions for the rest of the CoJeN cases, OP1.1, OP1.2, OP1.4 along with the corresponding time and length scale fits in the core/bypass and the bypass/ambient shear layers are provided in Appendix D. The agreement with the experiment for most frequencies including the peak noise is within 2-3dB for all cases except OP1.2 and OP1.4 jets (Figures D3, D5). The predictions for the latter two jets at the intermediate 60° angle show some 4dB over prediction relative to the experiment at low frequencies $St_D < 0.1$ (OP1.2) and high frequencies $St_D > 1$ (OP1.4). In both these cases, the RANS solution fails to capture the same potential core length of the jet within 20% in comparison with the LES calculation thereby both the potential core length parameter, β and the spreading rate, were taken directly from the LES. Therefore, it is believed that the reduction in accuracy of the suggested acoustic model in the case of the two CoJeN jets is caused by the inaccuracy of the RANS solution.

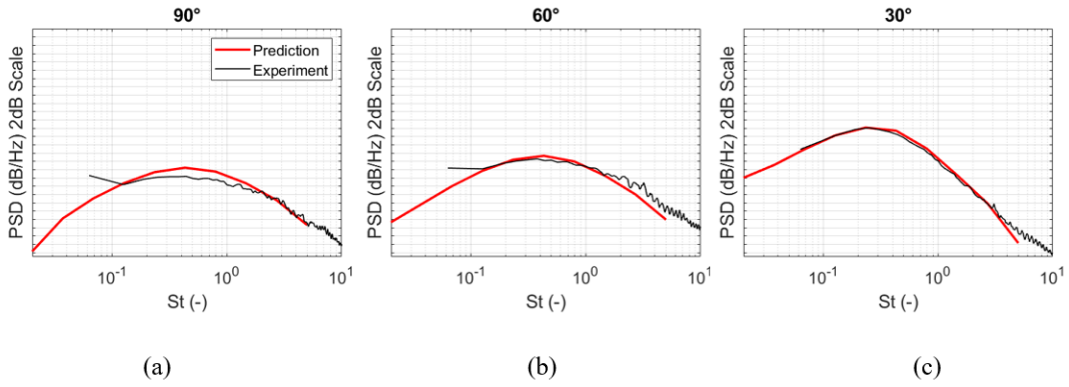

Figure 5.14: Comparison of the reduced-order model predictions with the experiment for the OP1.7 CoJeN jet at 90o(a), 60o (b), and 30o (c) polar angles to the jet flow.

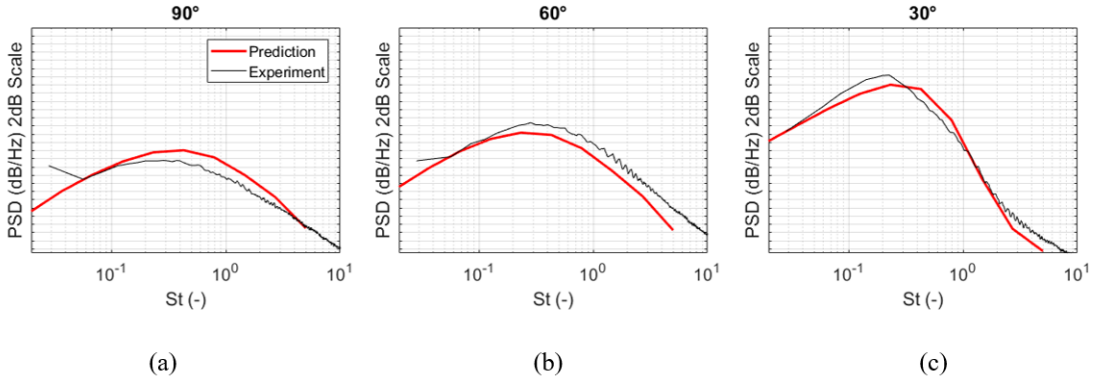

Figure 5.15: Comparison of the reduced-order model predictions with the experiment for the CoJeN OP1.3 jet at 90o(a), 60o (b), and 30o (c) polar angles to the jet flow.

5.6 Sensitivity analysis of the coaxial jet noise model

Having validated the acoustic model against the experiment, the next step is to analyse the effect of some commonly made assumptions: (i) ignoring the radial variation of the relative source amplitude and length scales inside the jet and (ii) ignoring the separate dipole source (5.3) representing the temperature noise source of the heated jet.

The assumptions will be tested in application for the two CoJeN jet cases, OP1.3 and OP1.7. Figures 5.16 (a,b,c) and Figures (d,e,f) show the acoustic model predictions for the OP1.7 and OP1.3 jet, respectively, where the interpolation of the source parameters inside the jet is disabled by assuming that the source parameters are the same as in the bypass/ambient shear layer. For the OP1.7 jet, the neglect of the source scale variations inside the jet leads to a small reduction in accuracy the noise spectra predictions for most frequencies remain within 1-2dB from the experiment. This is as expected for a single-stream-like jet. For the dual-stream OP1.3 jet, the same approximation neglects the effect of the bypass/core

shear layer on the dimensionless source parameters so that the effect of the dual-stream jet flow is only retained on the RANS solution. Under this simplification, which effectively ignores the importance of the jet interaction region in co-axial jet flow, the acoustic time and length scales in the jet core stream are underpredicted. This results in a shift of the peak noise frequencies for all angles and a significant underprediction of noise levels especially at 30° angle to the jet flow ($\sim 8-9$dB) in comparison with the experiment.

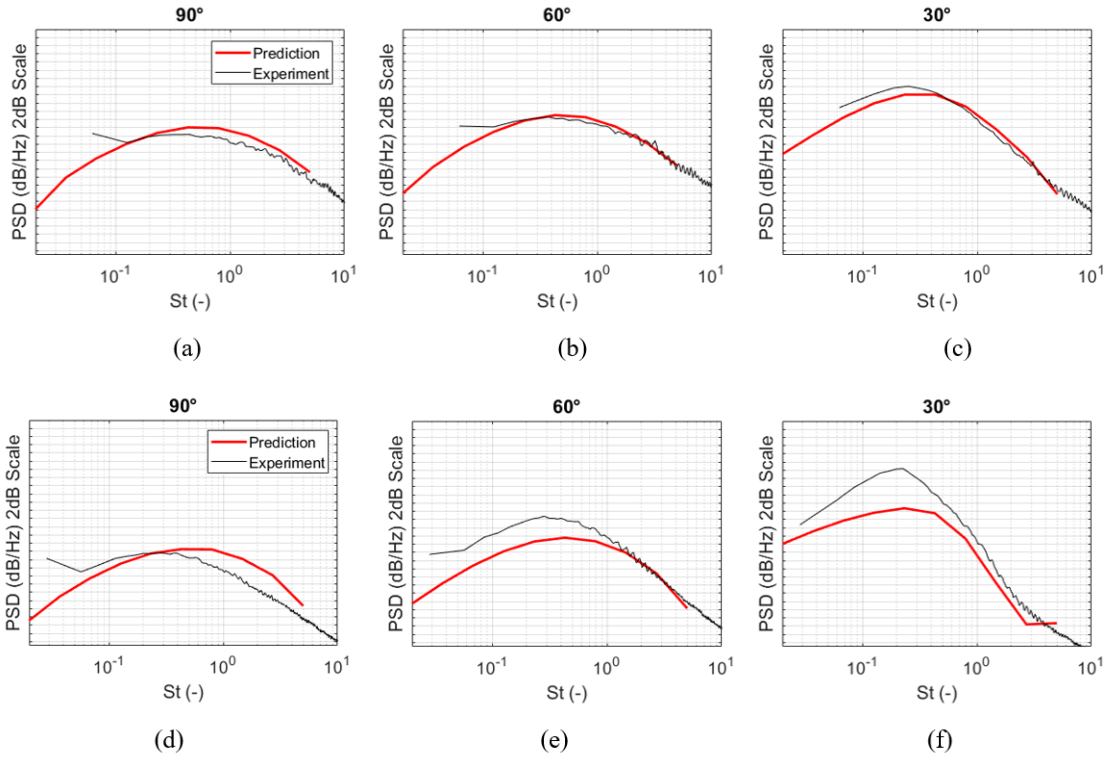

Figure 5.16: Effect of neglecting the radial variation of the acoustic source parameters inside the CoJeN OP1.7 (a),(b),(c) and OP1.3 jet (a),(b),(c) at different polar angles to the jet flow.

Figure 5.17 shows predictions of the acoustic model for the OP1.3 jet where the dual-stream jet noise structure in the jet is retained in accordance with the complete model but the dipole source representing the temperature noise source is disabled. In comparison with the neglect of the dual-stream source structure

(comp. with Figure 5.16), the neglect of the temperature source results in a less drastic reduction of the model fidelity. Indeed, in comparison with the full model, the predictions of the model which only includes the quadrupole sources are attenuated by 1dB on average. This attenuation increases the error of the "cold jet" acoustic model for the OP1.3 jet to about 3-4dB. Interestingly, the order of magnitude of this error is similar to the errors of the less accurate RANS solutions in the case of OP1.2 and OP1.4 jets (Appendix D).

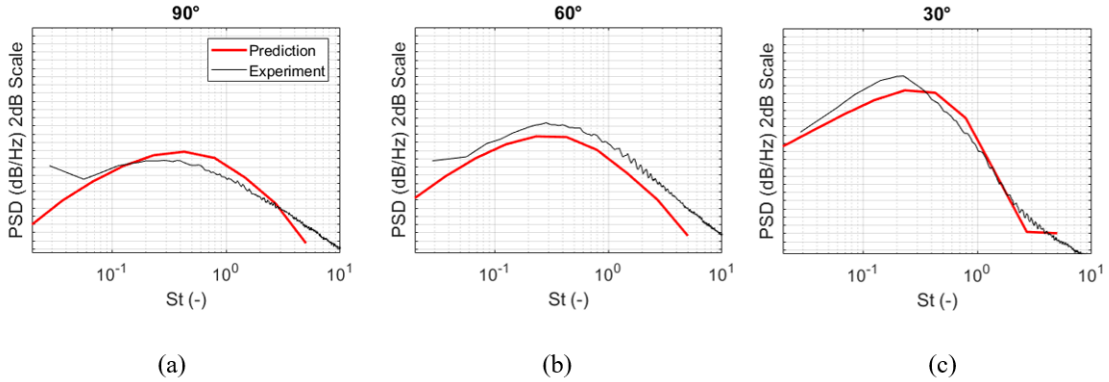

Figure 5.17: Effect of neglecting the hot temperature source in the CoJeN OP1.3 jet for acoustic spectra predictions at 90o(a), 60o (b), and 30o (c) polar angles to the jet flow.

It should be also noted that, due to a certain uncertainty of the similitude scaling of the coaxial jet flows, the source scales of the acoustic model can be extracted from the linear fit functions discussed in section 5.4 within 10-20% error. Figure 5.18 compares the noise spectra predictions of the suggested model for the OP1.7 when the acoustic time and space scales are varied by +/- 20% with respect to the previously evaluated values. Similarly, Figure 5.19 compares the noise spectra predictions of the suggested model for the OP1.3 when the acoustic time and space scales in both the shear layers are simultaneously increased or decreased by 20% with respect to the computed values. From comparison with the original spectra predictions (comp. with Figure 5.15), the acoustic scale variation by +/-20% leads to +/-2B error and +/-3dB error for the OP1.7 and the OP1.3

jet, respectively. A similar analysis shows that a 10% variation of the acoustic scales leads to +/1dB error for the same two CoJeN jets

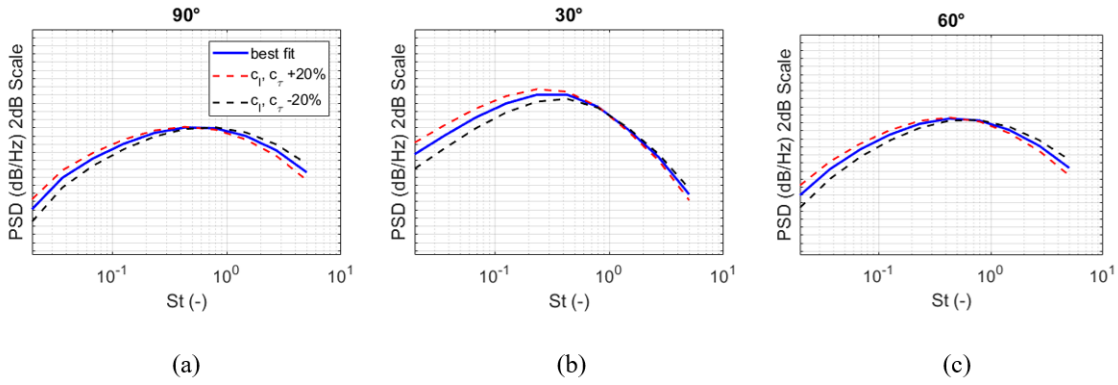

Figure 5.18: Sensitivity of the noise spectra predictions to a variation of the dimensionless scale parameters c_l and c_τ in the shear layer of the CoJeN OP1.7 jet at 90o(a), 60o (b), and 30o (c) polar angles to the jet flow.

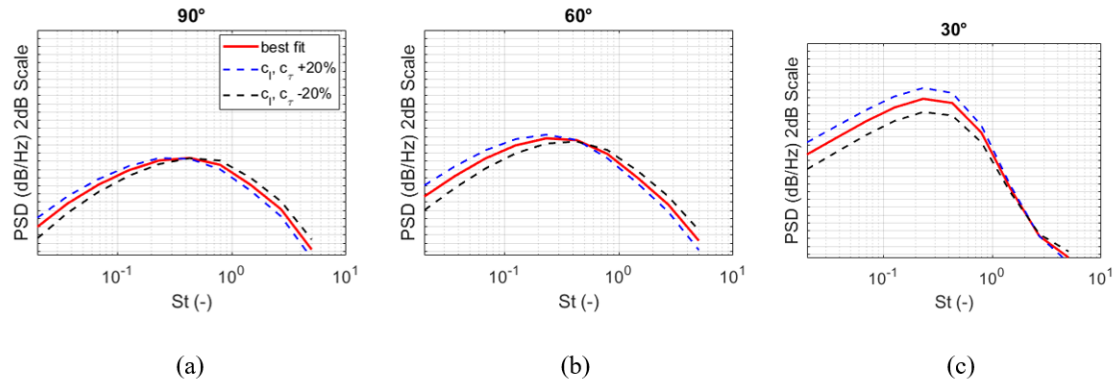

Figure 5.19: Sensitivity of the noise spectra predictions to a variation of the dimensionless scale parameters c_l and c_τ in the two shear layers of the CoJeN OP1.3 jet at 90o(a), 60o (b), and 30o (c) polar angles to the jet flow.

5.7 Overall Sound Pressure Levels

To conclude the results section, the capability of the suggested acoustic model to capture the difference is sound pressure levels between different CoJeN jet cases is

investigated. Band limited Over All Sound Pressure Level (OASPL) predictions of all 6 CoJeN jet cases and the corresponding experimental data are compared in the frequency band $0.1 < St_D < 3$ for microphone angles 30°, 60°, and 90°. Figure 5.20 shows the results obtained for relative OASPL in dB for different pairs of the CoJeN cases: OP1.2 vs OP1.1, OP1.3 vs OP1.2, and OP1.3 vs OP1.1 (an increase of the core stream velocity), OP1.1 vs OP1.4 (an increase of the bypass stream velocity), OP1.2 vs OP1.4 and OP1.3 vs OP1.4. It can be noted that in most cases, the difference in dB is captured within the error of 0.5-1dB in comparison with the experiment. The outlier cases include the relative predictions in comparison with the most challenging OP1.3 jet case which showed 2-3dB difference with the experiment.

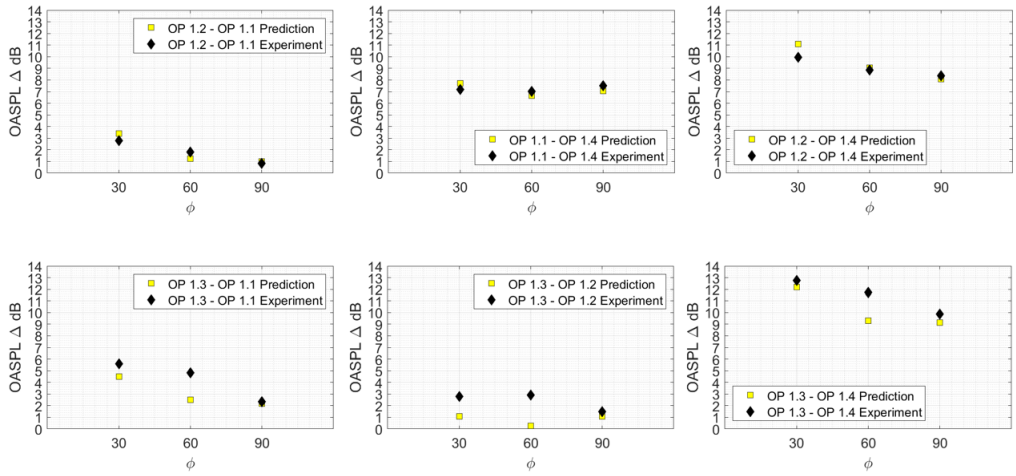

Figure 5.20: Prediction of the relative change in Over All Sound Pressure Levels (OASPL) between different CoJeN cases.

Summary

A new reduced-order acoustic model is developed for co-axial heated jet noise predictions. The model is based on the Goldstein generalized acoustic analogy [17], includes both the fluctuating Reynolds stress and the enthalpy source, and is

based on the RANS flow solutions. In addition to common assumptions for reduced order-models of its class, following the semi-empirical model of Khavaran and Bridges [Khavaran and Bridges 2010], the suggested model neglects the correlation between the fluctuating velocity and the temperature as well as assumes the direct proportionality between the auto-covariance of the fluctuating enthalpy stress with the velocity autocorrelation function. It is shown that both these assumptions are reasonably well satisfied for the heated jet flow case considered in the validation part. For sound propagation modeling, following Goldstein and Leib [28], the locally parallel flow equations are solved with taking into account the critical layer singularity in the case of the supersonic jet flow (CoJeN OP1.3 case).

The acoustic model is validated in comparison with the far-field measurements performed by QinetiQ for the jet flows corresponding to Operation Point (OP) 1.1,1.2,1.3,1.4, and 1.7 The jets correspond to the five cases which differ by core and bypass jet conditions from the database of the EU Coaxial Jet Noise experiment (CoJeN). All jets issue from the same short-cowl co-axial nozzle with a central body.

In most cases, the spectra predictions are within 2-3dB from the experiment for observer angles 30° – 90° to the jet flow and frequencies $0.1 < St_D < 5$, where the Strouhal number is defined on the bypass nozzle diameter and the bypass stream velocity. In all cases, the model correctly captures the peak noise frequencies and the corresponding peak noise levels within 1-2dB. The model is implemented in the user-friendly MATLAB/Octave environment and is suitable for rapid turn-around-time calculations: the sound spectra calculations on the standard personal laptop take several minutes for 3 microphone angles and 20 noise frequencies.

The new coaxial model is used to analyze the effect of some commonly made assumptions in jet noise modeling on the accuracy of far-field noise predictions for the heated dual-stream jet noise. In the case of an effective single stream jet

(OP1.7), the neglect of the scale variation inside the jet core has a minor effect on the noise spectra predictions. In the case of a dual-stream jet (OP1.3), the neglect of the variation of the dimensionless acoustic source, which emerges inside the jet due to the interaction of the shear layers, leads to a large (8-9dB) underprediction of peak jet noise. This finding is in agreement with the Institute of Sound and Vibration Research (ISVR) 4-source co-axial jet noise model [71] that regards the interaction noise as a very important contributor for jet noise especially for small angles to the jet flow. It is further demonstrated that neglect of the fluctuating enthalpy noise leads to attenuated sound spectra predictions by approximately 1dB in comparison with the full model. However, the overall accuracy of predictions in this case drops to 3-4dB. Furthermore, a similar reduction of accuracy is reported in the cases when the RANS solution is not sufficient to capture the correct length of the potential core of the jet within 20% in comparison with the LES data (for OP1.2 and OP1.4 jet cases). Hence, neither the exclusion of the heated jet noise source part from the model nor its operation with insufficiently accurate RANS flow solutions is recommended.

For the complete acoustic model in application to the dual-stream OP1.3 jet, it is further demonstrated that the noise spectra predictions are also reasonably insensitive to a variation of the acoustic scale parameters within uncertainty of their calculation from the LES-based fit functions. Predictive power of the suggested acoustic model to capture the difference is sound pressure levels between different CoJeN jet cases is investigated. Band limited Over All Sound Pressure Level (OASPL) predictions of all five CoJeN jet cases and the corresponding experimental data are compared in the frequency band $0.1 < St_D < 3$ for microphone angles 30°, 60°, and 90°. In most cases, the difference in the far-field sound due to a change of the core and /or bypass stream velocity and the core temperature is captured within 0.5-1dB in comparison with the experiment.

In comparison with previous multi-stream jet noise prediction schemes, the

suggested model is completely free from calibrations based on the far-field measurements. This is achieved by using the LES solution to inform the RANS-based source modeling. In comparison with the previous hybrid RANS-based jet noise models informed by LES, the current approach for computing the acoustic scales avoids the local point-to-point interpolations from LES to RANS flow solutions. Instead, the suggested model utilizes a non-dimensionalization based on the jet potential core and the spreading rate to focus on common patterns of different axi-symmetric jet flow solutions. The focus on common patterns in the jet flows rather than trying to precisely match flow solutions in specific jet locations allows one to reconstruct the acoustic model parameters with an automatic averaging over the jet shear layer as well as, potentially, over several jet flows of the same class to reduce the LES cost. The additional averaging is expected to make the suggested approach more robust against the statistical error in comparison with the previous hybrid RANS/LES models which rely on the local point field calibrations. The robustness is especially important for the computation of the acoustic time and space scale parameters that are prone to uncertainty in the jet flow areas of low turbulent intensity, where the signal to noise ratio is small.

Conclusions and Future work

The focus of this thesis was on temperature effects on sound propagation. In the framework of the generalised acoustic analogy it is possible to consistently separate the meanflow terms from the effective sources thus enabling a consistent treatment of the temperature and propagation effects thereby it was chosen as the base in the current work.

The non-uniform temperature distribution effect on noise propagation in a hot jet flow has been analysed for conditions of the hot SILOET jet experiment.

The effect of a locally amplified sound speed in the hot jet flow on far-field noise radiated a ring of point sources has been analysed for conditions of the SILOET jet experiment. The dipole-type and quadrupole-type sources correspond to auto-covariance the turbulent fluctuating Reynolds stresses and the fluctuating enthalpy stresses in the momentum and energy equations of the Goldstein generalised acoustic analogy, which are represented by delta functions in space and random processes in time. To fully concentrate on the propagation effects, the relative amplitudes of the source terms are calculated from the Large Eddy Simulation solution of the same jet and non-dimensionalised by the peak source term amplitude in each case.

To separate the jet flow heating effect on noise propagation from other effects, the adjoint Greens function equations are solved for the cold and the hot jet flow sound propagation models separately using a locally parallel Greens function approximation. In each axial section of the jet flow, the adjoint Greens function is

obtained by numerically solving a series of Rayleigh-type equations in each stream-wise section of the jet. The cold and the hot jet noise propagation models are defined so that they correspond to the same mean-flow velocity profiles obtained from LES while the definition of the sound speed was different. In the cold flow case, the variation of the sound speed is suppressed by making the local sound speed equal to the ambient sound speed value. In the hot jet model, the actual time-averaged local sound speed from the LES is used.

For subsequent low order modelling RANS solutions for three different nozzle geometries were performed. The considered jet cases include single-stream jets corresponding to the SILOET experiment, dual-stream jets with a central body corresponding to the CoJeN experiment and supersonic under-expanded LTRAC jets. Most of the considered jet cases are heated. RANS solutions are in a good agreement with the reference solutions, which makes these solution suitable for a further use in the low-order acoustic modelling.

An improved heated jet noise model was developed that is based on extension of the implementation of the Goldstein generalised acoustic analogy by [5]. The model uses LES to obtain dimensionless source amplitudes thereby limiting the use of calibration parameters based on the far-field. The results of the model are in a good agreement with the experimental data for the SILOET jets for a wide range of observer angles and frequencies. It is shown that the suggested model predictions compare favorably with those of the heated jet noise model developed by Khavaran [29], which is also based on the idea of presenting the total noise source as a linear combination of the fluctuating Reynolds stress term and the enthalpy term. In comparison with the Khavaran model, the new jet noise model takes into account the directivity of major quadrupole and dipole source terms thanks to the use of LES data.

A new reduced-order acoustic model was extended for co-axial heated jet noise predictions. In addition to common assumptions for reduced order-models of its

class, the suggested model neglects the correlation between the fluctuating velocity and the temperature as well as assumes the direct proportionality between the auto-covariance of the fluctuating enthalpy stress with the velocity autocorrelation function. It was shown that both these assumptions are reasonably well satisfied for the heated jet flow case considered. The acoustic model was validated in comparison with the far-field measurements jet flows corresponding to the five operating conditions which differ by core and bypass jet conditions.

The acoustic model has been validated in comparison with the far-field noise measurements of five co-axial jet flows, which issue from the same short cowl nozzle with a central body and correspond to a range of core-stream temperatures and acoustic Mach numbers.

In comparison with previous multi-stream jet noise prediction schemes, the suggested model is completely free from calibrations based on the far-field measurements. This is achieved by using the LES solution to inform the RANS-based source modeling. In comparison with the previous hybrid RANS-based jet noise models informed by LES, the current approach for computing the acoustic scales avoids the local point-to-point interpolations from LES to RANS flow solutions. Instead, the suggested model utilizes a non-dimensionalization based on the jet potential core and the spreading rate to focus on common patterns of different axi-symmetric jet flow solutions. The focus on common patterns in the jet flows rather than trying to precisely match flow solutions in specific jet locations allows one to reconstruct the acoustic model parameters with an automatic averaging over the jet shear layer as well as, potentially, over several jet flows of the same class to reduce the LES cost. The additional averaging is expected to make the suggested approach more robust against the statistical error in comparison with the previous hybrid RANS/LES models which rely on the local point field calibrations. The robustness is especially important for the computation of the acoustic time and space scale parameters that are prone to uncertainty in the jet flow areas

of low turbulent intensity, where the signal to noise ratio is small.

In this work it was shown that it is possible to lower down the level of empiricism for RANS-based models. Furthermore, there is a question for the future work if the acoustic source parameters and correlation scales to be extracted from LES for the low-order modelling can be universal for jets of similar flow conditions. In this sense, it would be useful to reduce the need of having a new LES solution for every jet noise calculation in order to inform RANS-based model. Thereby, reducing computational cost of jet noise prediction scheme. The motivation here is to construct the relevant database of these parameters and making it accessible to the wide range of researchers in academia and in industry.

The use of LES mean-flow data would be beneficial for reduced order acoustic modelling in order to evaluate sensitivity of the model. However, the use of RANS is considered as a faster solution but a lower-fidelity flow solution in comparison with LES for computing the mean-flow velocity and turbulent kinetic energy in the jet flow, which quantities could be further used in low-order jet noise modeling schemes.

Appendix A

Solution of the locally parallel flow equations

Using the following notations $\mathbf{G}^a = (\rho^a, u_1^a, u_2^a, u_3^a, p) = (\rho^a, u^a, v^a, w^a, p^a)$. in the framework of [28], for each observer location the following adjoint acoustic propagation equations are considered

$$\frac{\partial}{\partial t}\rho^a + \widetilde{v_i}\frac{\partial}{\partial y_i}\rho^a + \frac{u_i^a}{\bar{\rho}}\frac{\partial}{\partial y_i}\widetilde{\theta_{ij}} = 0, \tag{A.1}$$

$$\frac{\partial}{\partial t}u_i^a + \frac{\partial}{\partial y_i}\rho^a - \widetilde{v_j}\frac{\partial}{\partial y_j}u_i^a - u_j^a\frac{\partial \widetilde{v_j}}{\partial y_i} + \widetilde{c^2}\frac{\partial}{\partial y_i}p^a + p^a\frac{(\gamma-1)}{\rho}\frac{\partial}{\partial y_i}\tilde{\theta}_{ij} = 0, \tag{A.2}$$

$$\frac{\partial}{\partial t}p^a + \tilde{v}_j\frac{\partial}{\partial y_i}p^a + \frac{\partial}{\partial y_i}u_i^a - (\gamma-1)p^a\frac{\partial \tilde{v}_j}{\partial y_i} = \delta(\mathbf{x}-\mathbf{y}), \tag{A.3}$$

$$\frac{\partial}{\partial t}\rho^a + \tilde{u}\frac{\partial}{\partial x}\rho^a + \tilde{v}\frac{\partial}{\partial r}\rho^a + \frac{u^a}{\bar{\rho}}\frac{\partial}{\partial y_\alpha}\tilde{\theta}_{xy_\alpha} + \frac{v^a}{\bar{\rho}}\frac{\partial}{\partial y_\alpha}\tilde{\theta}_{ry_\alpha} = 0. \tag{A.4}$$

Assuming a locally parallel mean flow, for each axial section of the locally parallel jet flow field, equations (A.1)–(A.4) can be rewritten in the cylindrical coordinate

system,

$$\frac{\partial}{\partial t}u_a+\tilde{u}\frac{\partial}{\partial x}u^a+\tilde{v}\frac{\partial}{\partial x}u^a+\frac{\partial}{\partial x}\rho^a-u^a\frac{\partial\tilde{u}}{\partial x}-v^a\frac{\partial\tilde{v}}{\partial x}+\widetilde{c^2}\frac{\partial}{\partial x}p^a+p^a\frac{(\gamma-1)}{\tilde{\rho}}\frac{\partial}{\partial y_\alpha}\tilde{\theta}_{xy_\alpha}=0, \tag{A.5}$$

$$\frac{\partial}{\partial t}v_a+\tilde{u}\frac{\partial}{\partial x}v^a+\tilde{v}\frac{\partial}{\partial x}v^a+\frac{\partial}{\partial x}\rho^a-u^a\frac{\partial\tilde{u}}{\partial r}-v^a\frac{\partial\tilde{v}}{\partial r}+\widetilde{c^2}\frac{\partial}{\partial r}p^a+p^a\frac{(\gamma-1)}{\tilde{\rho}}\frac{\partial}{\partial y_\alpha}\tilde{\theta}_{ry_\alpha}=0, \tag{A.6}$$

$$\frac{\partial}{\partial t}w^a+\tilde{u}\frac{\partial}{\partial x}w^a+\tilde{v}\frac{\partial}{\partial r}w^a+\frac{\tilde{v}}{r}w^a+\frac{1}{r}\frac{\partial}{\partial\phi}\rho^a+\frac{1}{r}\widetilde{c^2}\frac{\partial}{\partial\phi}p^a=0, \tag{A.7}$$

$$\frac{\partial}{\partial t}p^a+\tilde{u}\frac{\partial}{\partial x}p^a+\tilde{v}\frac{\partial}{\partial r}p^a+\frac{\partial}{\partial x}u^a+\frac{1}{r}\frac{\partial}{\partial r}rv^a+\frac{1}{r}\frac{\partial}{\partial\phi}w^a-(\gamma-1)p^a(\frac{\partial\tilde{u}}{\partial x}+\frac{1}{r}\frac{\partial r\tilde{v}}{\partial r})=0. \tag{A.8}$$

After applying Fourier Transform to (A.5)–(A.8), the acoustic propagation equations for each azimuthal mode n becomes:

$$i\omega\hat{\rho}_n^a+\tilde{u}\frac{\partial}{\partial x}\hat{\rho}_n^a=0, \tag{A.9}$$

$$i\omega\hat{u}_n^a+\tilde{u}\frac{\partial}{\partial x}\hat{u}_n^a+\frac{\partial}{\partial x}\hat{\rho}_n^a+\tilde{c}^2\frac{\partial}{\partial x}\hat{\rho}_n^a=0, \tag{A.10}$$

$$i\omega\hat{v}_n^a+\tilde{u}\frac{\partial}{\partial x}\hat{v}_n^a+\frac{\partial}{\partial r}\hat{\rho}_n^a-\hat{u}_n^a\frac{\partial\tilde{u}}{\partial r}+\tilde{c}^2\frac{\partial}{\partial r}\hat{\rho}_n^a=0 \tag{A.11}$$

$$i\omega\hat{w}_n^a+\tilde{u}\frac{\partial}{\partial x}\hat{w}_n^a-\frac{n}{r}\hat{\rho}_n^a-\tilde{c}^2\frac{n}{r}\hat{p}_n^a=0, \tag{A.12}$$

$$i\omega\hat{p}_n^a+\tilde{u}\frac{\partial}{\partial x}\hat{p}_n^a+\frac{\partial}{\partial x}\hat{u}_n^a+\frac{1}{r}\frac{\partial}{\partial r}r\hat{v}_n^a+\frac{n}{r}\hat{w}_n^a=0. \tag{A.13}$$

Since the coefficients of the above equations no longer depend on the axial coordinate, the following substitution is used

$$\hat{X}(x,r)=\hat{X}(r)e^{-ikx\cos\phi},\quad k=\frac{\omega}{c},\quad k'=k\cos\phi,\quad \omega'=\omega-\tilde{u}k'. \tag{A.14}$$

This leads to the following system of ordinary differential equations

$$i\omega'\hat{u}_n^a - ik'\widetilde{c^2}\hat{p}_n^a = 0, \tag{A.15}$$

$$i\omega'\hat{v}_n^a - \hat{u}_n^a\frac{\partial\tilde{u}}{\partial r} + \widetilde{c^2}\frac{\partial}{\partial r}\hat{p}_n^a = 0, \tag{A.16}$$

$$i\omega'\hat{w}_n^a - \widetilde{c^2}\frac{n}{r}i\omega'\hat{p}_n^a = 0, \tag{A.17}$$

$$i\omega'\hat{p}_n^a - ik'\hat{u}_n^a + \frac{1}{r}\frac{\partial}{\partial r}r\hat{v}_n^a + \frac{n}{r}\hat{w}_n^a = 0. \tag{A.18}$$

This yields the following ordinary differential equation for the amplitude $f_n(r)$:

$$\frac{d^2}{dr^2}f_n + A\frac{d}{dr}f_n + Bf = 0, \tag{A.19}$$

where A and B are defined from equations (A.15)–(A.18) so that

$$A = \frac{1}{r} + \frac{1}{\widetilde{c^2}}\frac{d\widetilde{c^2}}{dr}, \tag{A.20}$$

$$B = \frac{\omega'^2}{\widetilde{c^2}} - k'^2 - \frac{k'}{\omega'}\left(\frac{1}{r}\frac{d\tilde{u}}{dr} + 2\frac{k'}{\omega'}\left(\frac{d\tilde{u}}{dr}\right)^2 + \frac{d^2\tilde{u}}{dr^2} + \frac{1}{\widetilde{c^2}}\frac{d\widetilde{c^2}}{dr}\frac{d\tilde{u}}{dr}\right) - \frac{n^2}{r^2}. \tag{A.21}$$

By using equation (A.15)

$$\hat{u}_n^a = \frac{1}{\omega'}k'\tilde{c^2}\hat{p}_n^a, \tag{A.22}$$

equation (A.16)

$$\hat{v}_n^a = \frac{1}{\mathrm{i}\omega'}\left(\hat{u}_n^a\frac{d\tilde{u}}{dr} - \tilde{c^2}\frac{d\hat{p}_n^a}{dr}\right), \tag{A.23}$$

equation (A.17)

$$\hat{w}_n^a = \frac{1}{\mathrm{i}\omega'}\tilde{c^2}\frac{n}{r}\hat{p}_n^a. \tag{A.24}$$

By substitute these three expressions in (A.18), one obtains

$$\mathrm{i}\omega'\hat{p}_n^a - \mathrm{i}k'\frac{1}{\omega'}k'\tilde{c^2}\hat{p}_n^a + \frac{1}{r}\frac{d}{dr}\left(r\frac{1}{\mathrm{i}\omega'}\left(\hat{u}_n^a\frac{d\tilde{u}}{dr} - \tilde{c^2}\frac{d\hat{p}_n^a}{dr}\right)\right) + \frac{n}{r}\frac{1}{\mathrm{i}\omega'}\tilde{c^2}\frac{n}{r}\hat{p}_n^a = 0 \tag{A.25}$$

or

$$\left(\mathrm{i}\omega' - i\,\frac{k'^2}{\omega'}\,\tilde{c^2} + \frac{1}{\mathrm{i}\omega'}\,\tilde{c^2}\,\frac{n^2}{r^2}\right)\hat{p}_n^a + \frac{1}{r}\,\frac{d}{dr}\left(r\,\frac{1}{\mathrm{i}\omega'}\,\hat{u}_n^a\,\frac{d\tilde{u}}{dr}\right) - \frac{1}{r}\,\frac{d}{dr}\left(r\,\frac{1}{\mathrm{i}\omega'}\,\tilde{c^2}\,\frac{d\hat{p}_n^a}{dr}\right) = 0. \tag{A.26}$$

Here

$$\frac{d}{dr}\left(r\,\frac{1}{\mathrm{i}\omega'}\,\hat{u}_n^a\,\frac{d\tilde{u}}{dr}\right) = \frac{d}{dr}\left(r\,\frac{1}{\mathrm{i}\omega'^2}\,k'\tilde{c^2}\,\frac{d\tilde{u}}{dr}\,\hat{p}_n^a\right) = \frac{da}{dr}\,\hat{p}_n^a + a\,\frac{d\hat{p}_n^a}{dr}, \tag{A.27}$$

where

$$a = r\,\frac{1}{\mathrm{i}\omega'^2}\,k'\tilde{c^2}\,\frac{d\tilde{u}}{dr}, \tag{A.28}$$

$$\frac{d}{dr}\left(r\,\frac{1}{\mathrm{i}\omega'}\,\tilde{c^2}\,\frac{d\hat{p}_n^a}{dr}\right) = \frac{db}{dr}\,\frac{d\hat{p}_n^a}{dr} + b\,\frac{d^2\hat{p}_n^a}{dr^2}, \tag{A.29}$$

and

$$b = r\,\frac{1}{\mathrm{i}\omega'}\,\tilde{c^2}. \tag{A.30}$$

Thus, we obtain

$$\left(\mathrm{i}\omega' - i\,\frac{k'^2}{\omega'}\,\tilde{c^2} + \frac{1}{\mathrm{i}\omega'}\,\tilde{c^2}\,\frac{n^2}{r^2}\right)\hat{p}_n^a + \frac{1}{r}\left(\frac{da}{dr}\,\hat{p}_n^a + a\,\frac{d\hat{p}_n^a}{dr}\right) - \frac{1}{r}\left(\frac{db}{dr}\,\frac{d\hat{p}_n^a}{dr} + b\,\frac{d^2\hat{p}_n^a}{dr^2}\right) = 0 \tag{A.31}$$

or

$$\left(\mathrm{i}\omega' - i\,\frac{k'^2}{\omega'}\,\tilde{c^2} + \frac{1}{\mathrm{i}\omega'}\,\tilde{c^2}\,\frac{n^2}{r^2} + \frac{1}{r}\,\frac{da}{dr}\right)\hat{p}_n^a + \left(\frac{a}{r} - \frac{1}{r}\,\frac{db}{dr}\right)\frac{d\hat{p}_n^a}{dr} - \frac{b}{r}\,\frac{d^2\hat{p}_n^a}{dr^2} = 0 \tag{A.32}$$

and also

$$-\frac{b}{r} = -\frac{\tilde{c^2}}{\mathrm{i}\omega'}. \tag{A.33}$$

By reducing this equation, we obtain

$$\frac{d^2\hat{p}_n^a}{dr^2} + A\frac{d\hat{p}_n^a}{dr} + B\hat{p}_n^a = 0, \tag{A.34}$$

where

$$A = -\frac{\mathrm{i}\omega'}{\tilde{c^2}}\left(\frac{a}{r} - \frac{1}{r}\frac{db}{dr}\right), \tag{A.35}$$

$$B = -\frac{\mathrm{i}\omega'}{\tilde{c^2}}\left(\mathrm{i}\omega' - i\,\frac{k'^2}{\omega'}\,\tilde{c^2} + \frac{1}{\mathrm{i}\omega'}\,\tilde{c^2}\,\frac{n^2}{r^2} + \frac{1}{r}\,\frac{da}{dr}\right). \tag{A.36}$$

Expanding this last equation and taking into account the fact that $k' = k\cos\phi$ does not depend on r, $\omega' = \omega - \tilde{u}k'$ depends on r only in $\tilde{u}$ and thus

$$\frac{d\omega'}{dr} = -k'\,\frac{d\tilde{u}}{dr}, \quad \frac{d}{dr}\,\frac{1}{\omega'} = \frac{1}{\omega'^2}\,k'\,\frac{d\tilde{u}}{dr}. \tag{A.37}$$

one has

$$A = -\frac{\mathrm{i}\omega'}{\tilde{c^2}}\left(\frac{1}{\mathrm{i}\omega'^2}\,k'\tilde{c^2}\,\frac{d\tilde{u}}{dr} - \frac{1}{r}\,\frac{d}{dr}\left(r\,\frac{1}{\mathrm{i}\omega'}\,\tilde{c^2}\right)\right), \tag{A.38}$$

where

$$\frac{d}{dr}\left(r\,\frac{1}{\mathrm{i}\omega'}\,\tilde{c^2}\right) = \frac{1}{\mathrm{i}\omega'}\,\tilde{c^2} + r\tilde{c^2}\,\frac{1}{\mathrm{i}\omega'^2}\,k'\,\frac{d\tilde{u}}{dr} + r\,\frac{1}{\mathrm{i}\omega'}\,\frac{d\tilde{c^2}}{dr}. \tag{A.39}$$

Hence, the final equation for A:

$$A = -\frac{\mathrm{i}\omega'}{\tilde{c^2}}\left(\frac{1}{\mathrm{i}\omega'^2}\,k'\tilde{c^2}\,\frac{d\tilde{u}}{dr} - \frac{1}{r}\,\frac{1}{\mathrm{i}\omega'}\,\tilde{c^2} - \tilde{c^2}\,\frac{1}{\mathrm{i}\omega'^2}\,k'\,\frac{d\tilde{u}}{dr} - \frac{1}{\mathrm{i}\omega'}\,\frac{d\tilde{c^2}}{dr}\right) = \frac{1}{r} + \frac{1}{\tilde{c^2}}\,\frac{d\tilde{c^2}}{dr}. \tag{A.40}$$

To re-express B, one obtains

$$\frac{da}{dr} = \frac{k'}{i}\left(\frac{1}{\omega'^2}\,\tilde{c^2}\,\frac{d\tilde{u}}{dr} + \frac{2}{\omega'}\,\frac{1}{\omega'^2}\,k'\,\frac{d\tilde{u}}{dr}\,r\,\tilde{c^2}\,\frac{d\tilde{u}}{dr} + \frac{d\tilde{c^2}}{dr}\,r\,\frac{1}{\omega'^2}\,\frac{d\tilde{u}}{dr} + \frac{d^2\tilde{u}}{dr^2}\,r\,\frac{1}{\omega'^2}\,\tilde{c^2}\right) \tag{A.41}$$

or

$$\frac{da}{dr} = \frac{k'\tilde{c^2}}{\mathrm{i}\omega'^2}\left(\frac{d\tilde{u}}{dr} + r\,\frac{2k'}{\omega'}\left(\frac{d\tilde{u}}{dr}\right)^2 + r\,\frac{1}{\tilde{c^2}}\,\frac{d\tilde{c^2}}{dr}\,\frac{d\tilde{u}}{dr} + r\,\frac{d^2\tilde{u}}{dr^2}\right). \tag{A.42}$$

It follows that

$$B = \frac{\omega'^2}{\tilde{c^2}} - k'^2 - \frac{n^2}{r^2} - \frac{k'}{\omega'}\left(\frac{1}{r}\,\frac{d\tilde{u}}{dr} + \frac{2k'}{\omega'}\left(\frac{d\tilde{u}}{dr}\right)^2 + \frac{1}{\tilde{c^2}}\,\frac{d\tilde{c^2}}{dr}\,\frac{d\tilde{u}}{dr} + \frac{d^2\tilde{u}}{dr^2}\right). \tag{A.43}$$

This results in deriving the final expressions (A.20) and (A.21).

Appendix B

Analytical solution for the Green's function

Let $\hat{\mathbf{G}}_n^a = (\hat{\rho}_n^a, \hat{u}_n^a, \hat{v}_n^a, \hat{w}_n^a, \hat{p}_n^a)$. Consider the case of an infinitely thin mixing layer at the lipline $R_0 = D/2$, when the solution can be found analytically. For external zone $r > R_0$ and internal zone $r < R_0$ we use subscripts e and i, respectively.

The following solution ansatz is used:

$$\hat{G}_4^a = \frac{\mathrm{i}\omega}{4\pi c^2 R}\, e^{\mathrm{i}k(R - x\cos\phi)} \sum_{n=0}^{\infty} f_n(r)\cos n\theta. \tag{B.1}$$

At the jump $r = R_0$, the pressure variable has discontinuity of the first kind. So, the solution is presented in the form

$$f_n(r) = \begin{cases} f_{ne}(r), & r > R_0, \\ f_{ni}(r), & r < R_0. \end{cases} \tag{B.2}$$

Assuming that $\tilde{u}$ and $\tilde{c}$ are constants in both internal and external zones, leads to

$$\lambda^2 = \frac{\omega'^2}{\tilde{c}^2} - k'^2 = \text{const}, \quad \omega'_e = \omega, \quad \omega'_i = \omega - \tilde{u}_i k', \tag{B.3}$$

$$\lambda_e^2 = k^2 - (k\cos\phi)^2 = k^2\sin^2\phi, \quad \lambda_i^2 = \frac{\omega_i'^2}{\tilde{c_i^2}} - k'^2. \tag{B.4}$$

In the external zone, one has:

$$f_{ne} = A_n J_n(\lambda_e r) + a_n H_n^{(1)}(\lambda_e r), \tag{B.5}$$

where

$$A_n = A_0(-i)^n \varepsilon_n, \quad A_0 = \frac{\mathrm{i}\omega}{4\pi R c^2}. \tag{B.6}$$

In internal zone, one obtains:

$$f_{ni} = b_n J_n(\lambda_i r), \tag{B.7}$$

where the coefficients b_n are so far unknown.

To match the two solutions and find the unknown a_n, b_n, at the jump $r = R_0$ suitable compatibility are derived.

Firstly, these rely on assuming that all solution components are bounded. Secondly, $\hat{v}_n^a$ is continuous, thus

$$[\hat{v}_n^a]_{r=R_0} = 0. \tag{B.8}$$

This means that

$$\hat{v}_{ni}^a|_{r=R_0} = \hat{v}_{ne}^a|_{r=R_0}\,. \tag{B.9}$$

From equation (A.16) we have

$$\hat{v}_n^a = \frac{1}{\mathrm{i}\omega'}\left(\hat{u}_n^a \frac{d\tilde{u}}{dr} - \tilde{c^2}\frac{d\hat{p}_n^a}{dr}\right). \tag{B.10}$$

At the jump $\frac{d\tilde{u}}{dr}\big|_{r=R_0} = 0$.Thus, the first condition for $\hat{p}_n^a$ is obtained:

$$\left[\frac{\tilde{c^2}}{\omega'}\frac{d\hat{p}_n^a}{dr}\right]_{r=R_0} = 0. \tag{B.11}$$

For equation (A.13)

$$\left[\frac{\partial}{\partial x}\,\hat{u}_n^a + \frac{1}{r}\,\frac{d}{dr}\,(r\,\hat{v}_n^a) + \frac{n}{r}\,\hat{w}_n^a\right]_{r=R_0} = 0. \tag{B.12}$$

From this equation and (A.18) one finds the second condition for $\hat{p}_n^a$:

$$[\omega'\hat{p}_n^a]_{r=R_0} = 0. \tag{B.13}$$

Condition (B.13) means

$$\omega'_i\hat{p}_{ni}^a|_{r=R_0} = \omega'_e\hat{p}_{ne}^a|_{r=R_0} \tag{B.14}$$

or

$$\omega'_i b_n J_n(\lambda_i R_0) = \omega\left(A_n J_n(\lambda_e R_0) + a_n H_n^{(1)}(\lambda_e R_0)\right). \tag{B.15}$$

Similarly, from condition (B.11) one obtains

$$\frac{\tilde{c_i^2}}{\omega'_i}\,b_n\lambda_i J'_n(\lambda_i R_0) = \frac{c^2}{\omega}\,\lambda_e\left(A_n J'_n(\lambda_e R_0) + a_n (H_n^{(1)})'(\lambda_e R_0)\right), \tag{B.16}$$

where $J'_n = dJ_n/dt$, $(H_n^{(1)})' = dH_n^{(1)}/dt$.

Thus, one arrives

$$s_1 b_n J_n(t_1) = A_n J_n(t_2) + a_n H_n^{(1)}(t_2), \tag{B.17}$$

$$s_2 b_n J'_n(t_1) = A_n J'_n(t_2) + a_n (H_n^{(1)})'(t_2), \tag{B.18}$$

where

$$t_1 = \lambda_i R_0, \quad t_2 = \lambda_e R_0, \quad s_1 = \frac{\omega'_i}{\omega}, \quad s_2 = \frac{\tilde{c_i^2}}{c^2}\frac{\omega}{\omega'_i}\frac{\lambda_i}{\lambda_e}. \tag{B.19}$$

Solving the linear system of equations (B.17)–(B.18), we find the required coefficients

$$a_n = \frac{A_n}{\Delta}\left(s_2 J'_n(t_1) J_n(t_2) - s_1 J_n(t_1) J'_n(t_2)\right), \tag{B.20}$$

$$b_n = \frac{A_n}{\Delta}\left(J_n(t_2)(H_n^{(1)})'(t_2) - J'_n(t_2) H_n^{(1)}(t_2)\right), \tag{B.21}$$

where

$$\Delta = s_1 J_n(t_1)(H_n^{(1)})'(t_2) - s_2 J'_n(t_1) H_n^{(1)}(t_2). \tag{B.22}$$

The expression for b_n can be further rearranged for simplicity of implementation.

$$J_n(t_2)(H_n^{(1)})'(t_2) - J'_n(t_2) H_n^{(1)}(t_2) = W(J_n, H_n^{(1)})(t_2) = \frac{2\mathrm{i}}{\pi t_2}. \tag{B.23}$$

Appendix C

Verification of the Khavaran model implementation

In order to verify the implemented Khavaran jet noise model [27], [29], [30] the so-called ring source directivity factor of the Khavaran model is computed and compared with the reference solution. For the sake of verification, the numerical solution is applied for the following analytical flow profiles as suggested in [27].

$$\frac{\rho(r)}{\rho_\infty} = 1, \quad M(r) = M_\infty + \frac{M_j - M_\infty}{2}\left\{1 - \tanh(r - \frac{D_j}{2})\right\}, \quad r \geq 0, \qquad \text{(C.1)}$$

where $M_j = 0.9$, $D_j = 6$. For the first profile we set $M_\infty = 0$, for the second profile $M_\infty = 0.18$ and for the third profile we have

$$M(r) = \frac{M_\infty}{2}\left\{1 - \tanh(r - 2D_j)\right\}, \quad r > 1.5D. \qquad \text{(C.2)}$$

The three input flow profiles are shown in fig.C.1.

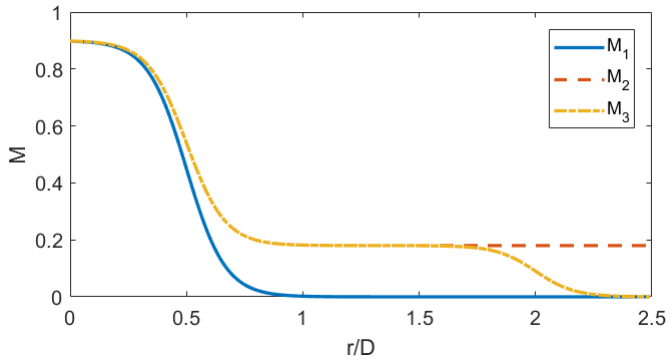

Figure C.1: Analytical flow profiles [27].

Following [27] a ring source directivity factor $D(\mathbf{x}, \mathbf{y}, \omega)$ is computed using the locally parallel jet model in MATLAB:

$$D^2(\mathbf{x}, \mathbf{y}, \omega) = \frac{(4\pi R)^2}{2\pi} \int_{-\pi}^{\pi} |G(\mathbf{x}, \mathbf{y}, \omega)|^2 d\theta. \tag{C.3}$$

Results are shown in fig.C.2 that demonstrates the effect of the mean flow on a stationary ring source as a function of the source location for a fixed distance from the jet to the observer. Here r^s is a span wise radial component of $\mathbf{y}$ (compare with Section 3.2). It can be seen that the obtained solutions are very similar to the reference solutions from [27]).

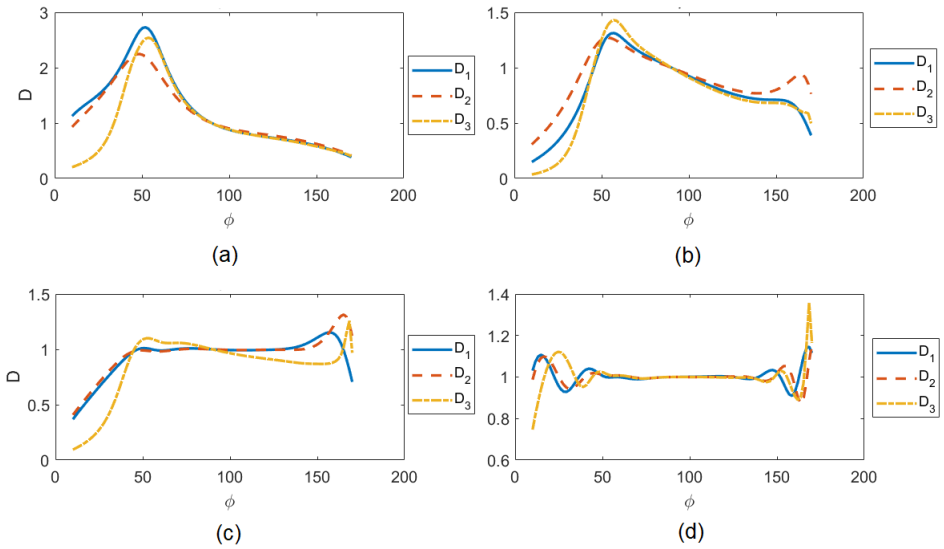

Figure C.2: Effect of the free jet on refraction. Green's function $D(\mathbf{x}, \mathbf{y}, \omega)$ at Strouhal number $St = 0.5$. Constant source intensity along a ring in a span-wise plane. Ring source location are defined at (a) at $r^s/D_j = 0$, (b) at $r^s/D_j = 0.5$, (c) at $r^s/D_j = 1$, (d) at $r^s/D_j = 3$.

Appendix D

Supplementary results for acoustic scale modeling and noise spectra predictions for CoJeN jets

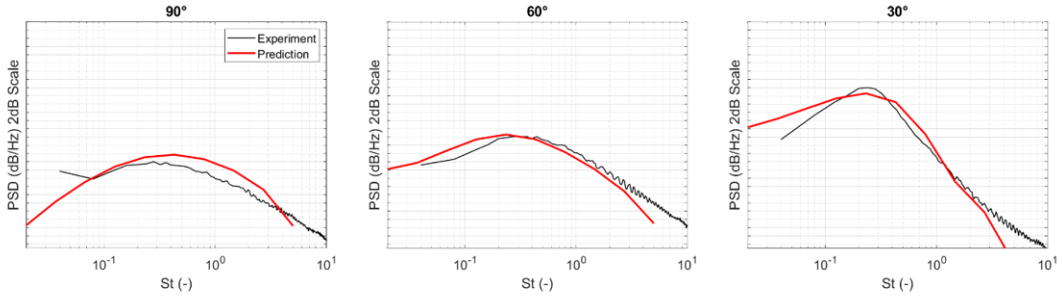

Figure D.1: Comparison of the reduced-order model predictions with the experiment for the CoJeN OP1.1 jet at 90°(a), 60° (b), and 30° (c) polar angles to the jet flow.

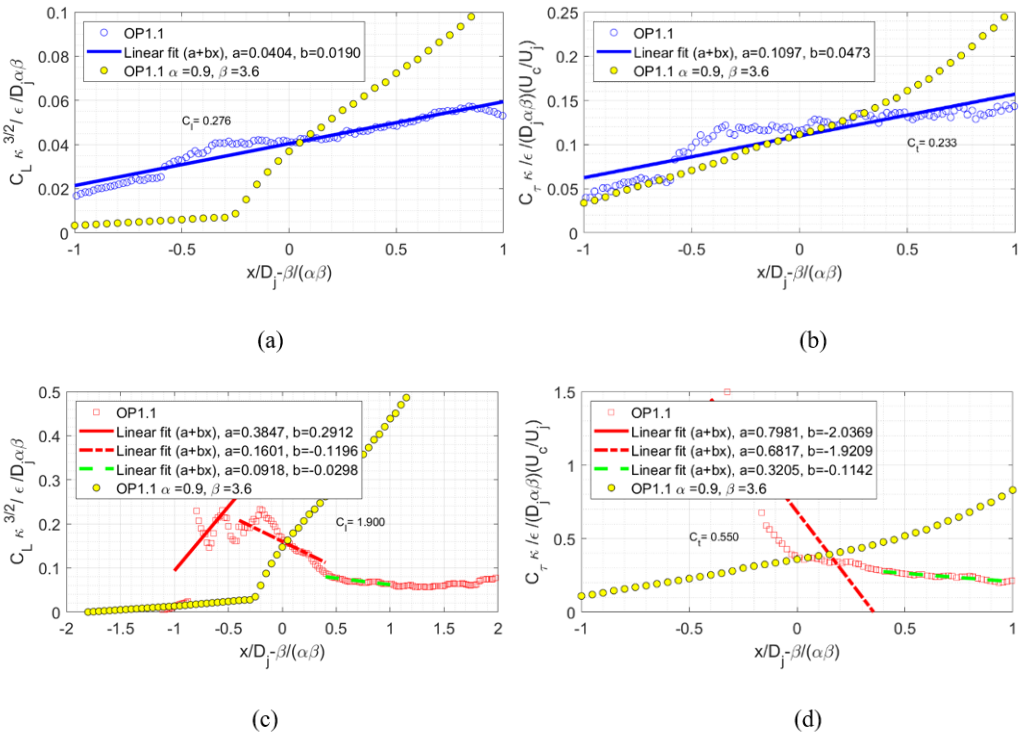

Figure D.2: Evaluation of the dimensionless acoustic correlation scales of the OP1.1 jet in the core/bypass shear layer for space (a) and time (b) lengthscales and in the core/bypass shear layers for space (c) and time (d) scales

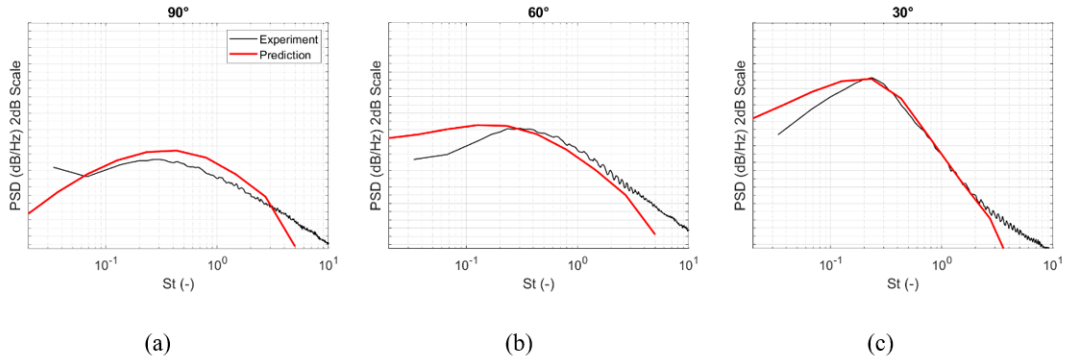

Figure D.3: Comparison of the reduced-order model predictions with the experiment for the CoJeN OP1.2 jet at 90°(a), 60° (b), and 30° (c) polar angles to the jet flow.

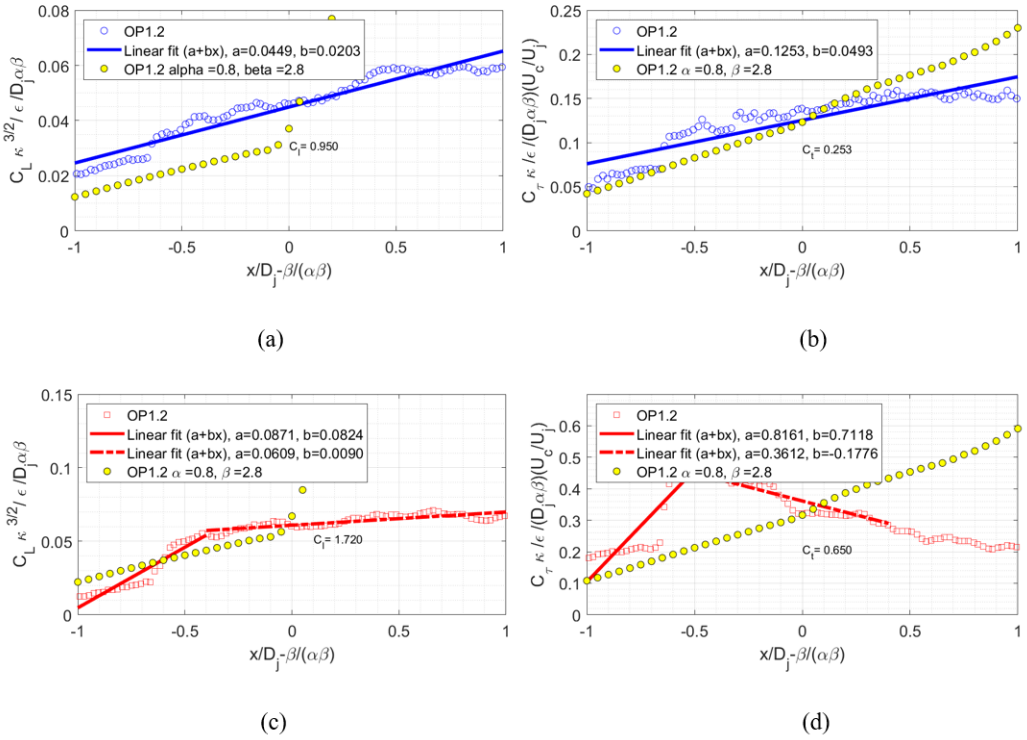

Figure D.4: Evaluation of the dimensionless acoustic correlation scales of the OP1.2 jet in the core/bypass shear layer for space (a) and time (b) lengthscales and in the core/bypass shear layers for space (c) and time (d) scales.

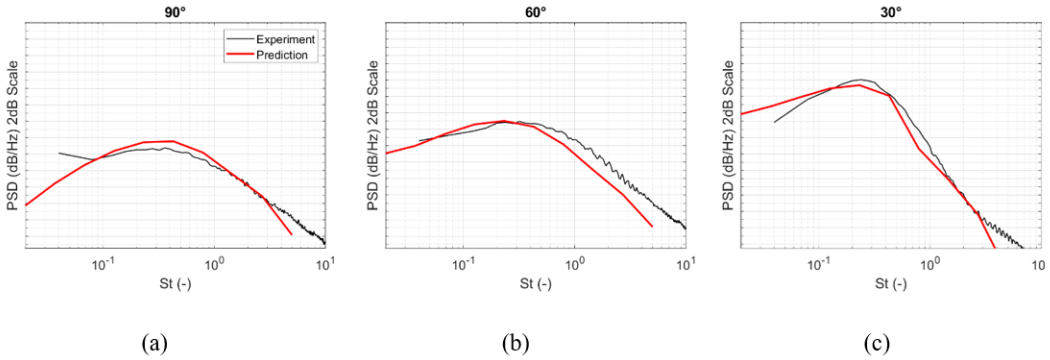

Figure D.5: Comparison of the reduced-order model predictions with the experiment for the CoJeN OP1.4 jet at 90°(a), 60° (b), and 30° (c) polar angles to the jet flow.

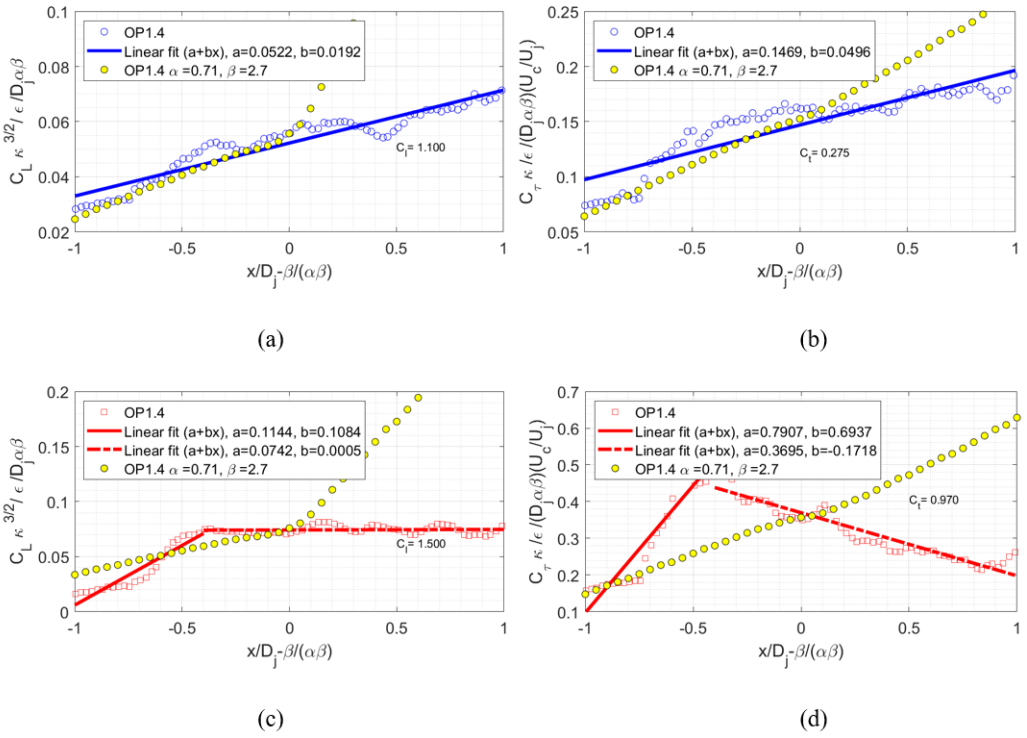

Figure D.6: Evaluation of the dimensionless acoustic correlation scales of the OP1.4 jet in the core/bypass shear layer for space (a) and time (b) lengthscales and in the core/bypass shear layers for space (c) and time (d) scales.

Reference List

[1] D. Bodony, S. Lele, "Jet noise prediction of cold and hot subsonic jets using large-eddy simulation," 10th AIAA/CEAS Aeroacoustics Conference, 3022, 2004.

[2] C. Bailly, , C. Bogey., "Contributions of computational aeroacoustics to jet noise research and prediction," *International Journal of Computational Fluid Dynamics*, 18:481-491, 2004.

[3] A. Uzun, G. A. Blaisdell, A. S. Lyrintzis., "Application of Compact Schemes to Large Eddy Simulation of Turbulent Jets," Journal of Scientific Computing, Volume 21, Issue 3, pp 283-319, 2004.

[4] P.R. Spalart, W-H. Jou, M. Strelets, S.R. Allmaras., "Comments on the Feasibility of LES for Wings, and on a Hybrid RANS/LES Approach," in Advances in DNS/LES: Direct numerical simulation and large eddy simulation, 137-148, 1997. Conference), 1997.

[5] S. Karabasov, M. Afsar, T. Hynes, A. Dowling, W. McMullan, C. Pokora, G. Page, J. McGuirk, "Using large eddy simulation within an acoustic analogy approach for jet noise modelling," 14th AIAA/CEAS Aeroacoustics Conference, 2010.

[6] A.P. Markesteijn, V. Semiletov, S.A. Karabasov, "CABARET GPU Solver for Fast-Turn-Around Flow and Noise Calculations," 21st AIAA/CEAS Aeroacoustics Conference, 2015.

[7] S. Grace, I. Gonzalez-Martino, D. Casalino, "Analysis of LBM/VLES fan-stage gap-flow data to inform simulation of fan broadband noise," Philosophical Transactions of the Royal Society, 2019.

[8] D.Casalino, S.K. Lele, S.K. "Lattice-Boltzmann simulation of coaxial jet noise generation," Center for Turbulence Research, Proceedings of the Summer Program, 2014.

[9] Lighthill, M.J. "On Sound Generated Aerodynamically. I. General Theory," *Proc. R. Soc. A Math. Phys. Eng. Sci.*, vol. 211, no. 1107, pp. 564587, 1952

[10] Lighthill, M.J. "On Sound Generated Aerodynamically. II. Turbulence as a Source of Sound," *Proc. R. Soc. A Math. Phys. Eng. Sci.*, vol. 222, no. 1148, pp. 132, 1954.

[11] G.M. Lilley, "On the noise from jets," Noise Mechanisms, AGARD-CP-131, 13.113.12, 1974.

[12] K. Viswanathan, "Aeroacoustics of hot jets," J. Fluid Mech. 516, pp. 39–82, 2004.

[13] M.J. Fisher, P.A. Lush, M. Harper-Bourne "Jet noise," J Sound Vib.28:563-585, 1973.

[14] B. Tester B, C. Morfey, "Developments in jet noise modelling – theoretical predictions and comparisons with measured data". J Sound Vib 46(1), 1976.

[15] H.S. Ribner, "The generation of sound by turbulent jets," In Advances in Applied Mechanics, vol. 8, pp. 108-182, 1964.

[16] J. E. Ffowcs Williams, D. L. Hawkings, "Sound generation by turbulence and surfaces in arbitrary motion," Philos. Trans. R. Soc., A264, 32142, 1969.

[17] M. E. Goldstein, "A generalized acoustic analogy," J. Fluid Mech., 488, 315-333, 2003.

[18] A. Samanta, J.B. Freund, ,M. Wei, S.K. Lele, "Robustness of acoustic analogies for predicting mixing-layer noise," AIAA J. 44, 2780-2786, 2006.

[19] C. K. W. Tam, K. C. Chen, "A statistical model of turbulence in two-dimensional mixing layers," J. Fluid Mech. 92, 303-326, 1979.

[20] S.C. Crow, and F.H. Champagne, "Orderly Structure in Jet Turbulence," J. Fluid Mech., 48, 547591, 1971.

[21] C. K. W. Tam, L. Auriault, "Jet Mixing Noise from Fine-Scale Turbulence," AIAA Journal, Vol. 37, No. 2, pp.145–153, 1999.

[22] A. Cavalieri, P. Jordan, A. Agarwal and Y. Gervais,"Jittering wavepacket models for subsonic jet noise," J. Sound Vib. 330, 4474-4492, 2011.

[23] T. Colonius, A. Samanta and K. Gudmundsson, "Parabolized stability equation models of large-scale mixing noise," Procedia IUTAM 1 64-73, 2010.

[24] P. Jordan, T. Colonius, "Wave Packets and Turbulent Jet Noise," Ann. Rev.Fluid Mech. 45. 173-195 2013.

[25] R. Reba, S. Narayanan and T. Colonius, "Wave-packet models for large-scale mixing noise," Int. J. Aeroacoustics 9(4& 5) 533-558, 2010.

[26] A. Khavaran, J. Bridges, "Modelling of turbulence generated noise in jets", Technical Report, TM-2004-213105, NASA, 2004.

[27] A. Khavaran, N.J.Georgiadis, J. Bridges, and V.F.Dippold, "Effect of free jet on refraction and noise," AIAA-2005-2941, 2005.

[28] M. E. Goldstein and S. J.Leib, "The Aero-acoustics of slowly diverging supersonic jets," J. Fluid Mech., 600, 291-337, 2008.

[29] A. Khavaran, D.C. Kenzakowski, and A.F. Mielke-Fagan "Hot jets and sources of jet noise," International J. Aeroacoustics, 9, pp. 491–532, 2010.

[30] A. Khavaran, and J. Bridges, "An empirical temperature variance source model in heated jets," Technical Report, TM-2012-217743, NASA, 2012.

[31] J. Bridges, "Simple Scaling Of Multi-Stream Jet Plumes For Aeroacoustic Modeling". AIAA SciTech Conference 4-8, 2016.

[32] M. Abramowitz and I.A. Stegun. "Handbook of Mathematical Functions," National Bureau of Standards Applied Mathematics Series. US Department of Commerce, 1970.

[33] C. K. W.Tam, and L. Auriault, "Mean flow refraction effects on sound from localized sources in a jet," J. Fluid Mech., 370, 149-174, 1998.

[34] SILOET Programme Rolls-Royce private data.

[35] QinetiQ Co-axial Jet Noise (CoJeN) experiment.

[36] D. J. Tan, D. Honnery, A. Kalyan, V. Gryazev, S. A. Karabasov, and D. M. Edgington-Mitchell, "Correlation analysis of high resolution particle image velocimetry data of screeching jets," AIAA J., pp. 163. 2017.

[37] SOLIDWORKS, 2017.

[38] ICEM grid generation ver. 16.5.

[39] Ansys Fluent ver. 16.5.

[40] MATLAB ver. R2019b.

[41] A. Kalyan, V. Gryazev, S.A. Karabasov, D.J. Tan, M. Wong, D. Honnery, D. Edgington-Mitchell, "Improved predictions of broadband shock associated noise in supersonic jet," INTER-NOISE and NOISE-CON Congress and Conference Proceedings 255 (6), 1338-1349, 2017.

[42] D. J. Tan, D. Honnery, D. M. Edgington-Mitchell, A. Kalyan, V. Gryazev, and S. A. Karabasov, "Equivalent broadband shock-associated noise source reconstruction from particle image velocimetry measurements," AIAA J., pp. 137, 2018.

[43] C. K.W. Tam,, and A. Ganesan, "A Modified $k - \varepsilon$ Turbulence Model for Calculating the Mean Flow and Noise of Hot Jets, AIAA Journal, Vol. 42, No. 1, pp. 2634, 2004.

[44] F. R. Menter, "Zonal Two Equation k-omega Turbulence Models for Aerodynamic Flows," AIAA Paper 93-2906, 1993.

[45] F.R. Menter, "Two-equation eddy-viscosity turbulence models for engineering applications," AIAA J. 32: 15981605 1994

[46] A.P. Markesteijn, V.A. Semiletov, S.A. Karabasov, "GPU CABARET solutions for the SILOET jet noise experiment: Flow and noise modelling," AIAA-2016-296, 37, No. 2, pp.145-153, 2016.

[47] A. Skeen, "The development of high-speed PIV techniques and their application to jet noise measurement," PhD thesis, University of Warwick, 2006.

[48] C. E. Tinney, and P. Jordan, "The near pressure field of co-axial subsonic jets," J. Fluid Mech. 611, 175204, 2008.

[49] C.J. Mead,, C. Wrighton, K. Britchford, "An Experimental Study of Co-Axial Jets Using Acoustic", PIV&LDA Methods (CoJen), AIAA 2015-3122.

[50] A.P. Markesteijn, and S.A. Karabasov, "An LES Study of Core Temperature, Velocity, and Mach Number Effect on the Far-Field Noise of Co-Axial Jets," 25th AIAA/CEAS Aeroacoustics Conference (Aeroacoustics 2019), 20 - 23 May 2019, Delft, The Netherlands.

[51] A. P. Markesteijn , V. Gryazev, S. A. Karabasov, R.S. Ayupov, L. A. Benderskiy, D A. Lyubimov, "Flow and Noise Predictions of the CoJeN Jets: Cross-Validation and Investigation of Mach Number and Temperature Effects," 25th AIAA/CEAS Aeroacoustics Conference (Aeroacoustics 2019), 20 - 23 May 2019, Delft, The Netherlands.

[52] C.K.W. Tam, K. Viswanathan, K.K Ahuja, J. Panda, "The sources of jet noise: experimental evidence," J. Fluid Mech. 615, 253-292, 2008.

[53] M. Z. Afsar, M. E.Goldstein, A. M.Fagan "Enthalpy ux/Momentum ux Coupling in the Acoustic Spectrum of Heated Jets," AIAA J., 49, No. 11, pp. 2522–2531, 2011

[54] S.A. Karabasov, C. Bogey, T. Hynes, "An investigation of the mechanisms of sound generation in initially laminar subsonic jets using the Goldstein acoustic analogy," Journal of Fluid Mechanics 714, 24–5, 2013.

[55] S. J.Leib, and M. E. Goldstein, "Hybrid Source Model for Predicting High-Speed Jet," Noise AIAA Journal , 49(7), 1324-1335, 2011.

[56] V.A. Semiletov, S.A. Karabasov, "A volume integral implementation of the Goldstein generalised acoustic analogy for unsteady flow simulations," Journal of Fluid Mechanics 853, 461-487, 2018.

[57] N.K. Depuru Mohan, A.P. Dowling, S.A.Karabasov, H. Xia, O. Graham, T.P.Hynes, P.G.Tucker, "Acoustic sources and far-field noise of chevron and round jets,", AIAA J. 53 (9), 2421-2436, 2015.

[58] B.S. Henderson, and S.J. Leib, "Measurements and Predictions of the Noise from Three-Stream Jets," 21st AIAA/CEAS Aeroacoustics Conference, AIAA AVIATION Forum, (AIAA 2015-3120)

[59] M. E. Goldstein,, Adrian Sescu and M. Z. Afzar, "Effect of non-parallel mean flow on the Greens function for predicting the low-frequency sound from turbulent air jets" J.Fluid Mech., 695, 199234, 2012

[60] V. Gryazev, A.P. Markesteijn, and S.A. Karabasov, "Temperature effect on the apparent position of effective noise sources in a hot jet," AIAA Aeroacoustics Conference, 25-29 June, Atlanta, 2018.

[61] S. A. Karabasov, "Understanding jet noise," Phil. Trans. R. Soc. 368, pp. 3593–3608, 2010.

[62] G. A. Faranosov, V. M. Goloviznin, S. A. Karabasov, V. G. Kondakov,, V. F. Kopiev, M. A. Zaitsev, "CABARET method on unstructured hexahedral grids for jet noise computation," Comp. and Fluids, 88, 165–179, 2013.

[63] A.P. Markesteijn, and S.A.Karabasov, "GPU CABARET Solver Extension to Handle Complex Geometries Utilizing snappyHexMesh with Asynchronous Time Stepping", AIAA 2017–4184.

[64] A.P. Markesteijn, and S.A.Karabasov, "CABARET solutions on Graphics Processing Units for NASA jets: grid sensitivity and unsteady inflow condition effect", CR Mecanique (Proc. French Academy of Sciences), 346 (10), 948–963, 2018.

[65] A.P. Markesteijn, and S.A.Karabasov, "GPU CABARET Solutions for the CoJen Jet Noise Experiment," 2018 AIAA/CEAS Aeroacoustics Conference, AIAA AVIATION Forum, (AIAA 2018–3921).

[66] P.J. Morris and F. Farassat, "Acoustic analogy and alternative theories for jet noise prediction," AIAA Journal, 4, no. 4:671-680, 2002.

[67] V. Gryazev, A.P. Markesteijn, and S.A. Karabasov, "Low-Order Models of Dual-Stream Jet Noise with Temperature Effects Based on the Goldstein Generalised Acoustic Analogy," AIAA Aeroacoustics Conference, 20-23 May, Delft, The Netherlands, 2019.

[68] V.A. Semiletov, S.A. Karabasov,"On the similarity scaling of jet noise sources for low-order jet noise modelling based on the Goldstein generalized acoustic analogy," Int. J. Aeroacoustics, Volume: 16 issue: 6, 476–490, 2017.

[69] J. Bridges, and M.P. Wernet, "The NASA Subsonic Jet Particle Image Velocimetry (PIV) Dataset," NASA/TM-2011-216807, 2011

[70] P. O. Witze, "Centerline velocity decay of compressible free jets". AIAA J., 12(4), 417-418, 1974.

[71] W.D. Bryce, and C.B.Chinoy, "A method for predicting static-to-flight effects on coaxial jet noise," J. Sound Vib. 375 (2016) 132-161, 2016.